Thermoelectric Properties of $Bi_{1-x}Sb_x$ Nanowires and Lead Salt Superlattice Nanowires

by

Yu-Ming Lin

B.S., National Taiwan University (1996)
M.S., Massachusetts Institute of Technology (2000)

Submitted to the Department of Electrical Engineering
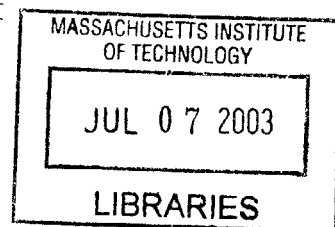and Computer Science
in partial fulfillment of the requirements for the degree of

Doctor of Philosophy

at the

MASSACHUSETTS INSTITUTE OF TECHNOLOGY

June 2003

Author .
Department of Electrical Engineering and Computer Science
May 9, 2003

Certified by......
Mildred S. Dresselhaus
Institute Professor of Electrical Engineering and Physics
Thesis Supervisor

Certified by.......
Jackie Y. Ying
Professor of Chemical Engineering
Thesis Supervisor

Accepted by ......
Arthur C. Smith
Chairman, Departmental Committee on Graduate Students

Thermoelectric Properties of $Bi_{1-x}Sb_x$ Nanowires

and Lead Salt Superlattice Nanowires

by

Yu-Ming Lin

Submitted to the Department of Electrical Engineering and Computer Science
on May 9, 2003, in partial fulfillment of the
requirements for the degree of
Doctor of Philosophy

Abstract

This thesis involves an extensive experimental and theoretical study of the thermo-electric-related transport properties of $Bi_{1-x}Sb_x$ nanowires, and presents a theoretical framework for predicting the electrical properties of superlattice nanowires. A template-assisted fabrication scheme is employed to synthesize Bi-based nanowires by pressure injecting liquid metal alloys into the hexagonally packed cylindrical pores of anodic alumina. These nanowires possess a very high crystalline quality with a diameter-dependent crystallographic orientation along the wire axis. A theoretical model for $Bi_{1-x}Sb_x$ nanowires is developed, taking into consideration the effects of cylindrical wire boundary, multiple and anisotropic carrier pockets, and non-parabolic dispersion relations. A unique semimetal-semiconductor (SM-SC) transition is predicted for these nanowires as the wire diameter decreases or as the Sb concentration increases. Also, an unusual physical phenomenon involving a very high hole density of states due to the coalescence of 10 hole carrier pockets, which is especially advantageous for improving the thermoelectric performance of p-type materials, is uncovered for $Bi_{1-x}Sb_x$ nanowires.

Various transport measurements are reported for Bi-related nanowire arrays as a function of temperature, wire diameter, Sb content, and magnetic field. $R(T)$ measurements show distinct T dependences for semimetallic and semiconducting nanowires, as predicted by the theory, and the condition for the SM-SC transition can be clearly identified. Enhanced thermopower is observed for $Bi_{1-x}Sb_x$ nanowires as the diameter decreases or as the Sb content increases, indicating that both quantum confinement effects and Sb alloying effects are important for improving the thermo-electric performance. The theoretical model is further extended to study transport properties of Te-doped Bi nanowires and Sb nanowires, and good agreement between theoretical predictions and experimental results is obtained.

A model for superlattice nanowires is presented to evaluate their potential for thermoelectric applications. Thermoelectric properties of superlattice nanowires made of various lead salts (PbS, PbSe, and PbTe) are investigated as a function of segment length, wire diameter, crystal orientation along the wire axis, and length ratio of

the constituent nanodots. An interesting inversion of the potential barrier and well induced by quantum confinement is predicted in superlattice nanowires as the wire diameter decreases. ZT values higher than 4 and 6 are predicted for 5 nm-diameter PbSe/PbS and PbTe/PbSe superlattice nanowires, respectively, at 77 K, and these ZT values are significantly larger than those of their corresponding alloy nanowires. For a given superlattice period, the ZT value can be further improved by adopting different segment lengths for the two constituent materials. The model developed here not only can determine the optimal superlattice nanowire parameters (segment length, diameter, materials, and doping level) for thermoelectric applications, but also can be extended to other superlattice systems, such as 3D quantum dot arrays. Furthermore, the theoretical foundation given here provides a general framework to study properties of interest to other applications of superlattice nanowires.

Thesis Supervisor: Mildred S. Dresselhaus
Title: Institute Professor of Electrical Engineering and Physics

Thesis Supervisor: Jackie Y. Ying
Title: Professor of Chemical Engineering

Acknowledgments

To Prof. Mildred Dresselhaus and Prof. Jackie Ying I owe my sincere gratitude, without them this thesis would not be possible. From Prof. Dresselhaus I received not only the research training, but also her diligent attitude towards life. Her devotion to the pursuit of science have been a constant inspiration to me. I am especially amazed by her energetic and vigorous character that draws people like a magnet. I would like to thank Prof. Jackie Ying for offering me the opportunity to work in her laboratory and for her strong support, insightful advice, and continued encouragement.

I wish to express my gratefulness to my thesis committee members, Prof. Gang Chen and Prof. Qing Hu, for their precious time and constructive comments.

I am much indebted to Dr. Zhibo Zhang for his mentorship in my first year. He has patiently and systematically trained me in the fabrication techniques for nanowires. I am greatly influenced by his meticulousness in research and have acquired useful experimental skills from him. Dr. Xiangzhong Sun has played a vital role in developing the theoretical part of the thesis. Dr. Sun and Mr. Wolfgang Rupprecht have offered great assistance with the system administration of the group computers. Discussions with Dr. Joseph Heremans have been very fruitful and my research has benefited significantly from his broad knowledge on Bi systems. I am also grateful to Yinlin Xie for her assistance in the preparation of various Bi alloys, Dr. Fang-Cheng Chou for his expertise with the SQUID equipment, and Mr. Michael Frongillo for the assistance with electron microscopy.

The most valuable assets in the Dresselhaus research group are the pleasant environment and the friendly group members. Dr. Takaaki Koga was my office-mate for the first three years, and we had a lot of interesting conversations on topics that range from science to politics. His creativity and mathematical insight always impressed me. The laughter of Dr. Sandra Brown from three offices away was always helpful for stress relief. Dr. Stephen Cronin has offered countless assistance in solving experimental obstacles. The occasional crackers and desserts from Dr. Adelina Pinheiro Santos and Grace Chou were always helpful in maintaining my vitality in the late

afternoon. The TA experience with Marcie Black in 6.732 and 6.734 was a joyful one, and her devotion to the solar cell technology was admirable. I enjoyed the salads and crêpes made by Oded Rabin, who also provided me many great suggestions for my research. I would like to thank the following people for making MGM such an interesting and memorable place: Dr. Hao Xin, Dr. Ado Jorio, Georgii Samsonidze, Dr. Antonio Souza Filho, Prof. Riichiro Saito, and Ming Tang. The experience at MIT would not be half as fun without Dr. Gene Dresselhaus, and I enjoyed tackling his many 10-minute challenges in computer problems. I am also obliged to Ms. Laura Doughty, whose beautiful singing voice is often heard in the hallway, for her professional administrative support.

Thanks to Prof. Jackie Ying, I have the chance to know another group of interesting people at the Nanostructured Materials Research Laboratory. There is always laughter with Dr. Justin McCue, who happened to have the same birthday as me, and who helped me a lot in improving the anodic alumina film synthesis. I am indebted to Dr. Mark Fokema, Dr. Martin Panchula, Dr. Neeraj Sangar, and Dr. Andrey Zarur for their help with the equipment set-up and for their useful advice in experiments. I am also grateful to Dr. Chen-Chi Wang, Duane Myers, Dr. Edward Ahn, Dr. John Lettow, Dr. Jason Sweeney, Yee Su, Steven Weiss, Suniti Moudgil, Thomas Lancaster, Todd Zion, Tseh-Hwan Yong, Jianyi Cui, and Dr. Jinsuo Xu. Their friendship makes my time at MIT a joyful experience.

This thesis is dedicated to my family, especially to my parents, Lloyd Lin and Spring Ho, who have constantly given me their unreserved love and support throughout my life.

Contents

List of Figures

9

12

14

List of Tables

18

Chapter 1

Introduction

1.1 Background

Nanostructured materials have received significant attention in recent years because of their fundamental importance and potential applications in areas ranging from chemistry, physics, electronics, optics, materials science to biology. In the field of electronics and optics, the drive to miniaturize devices and increase storage density has fueled research in nanotechnology. The recent advances in material science and microfabrication techniques, such as the epitaxial growth, electron beam lithography, chemical vapor deposition, vapor-liquid-solid growth [1] and self-assembly approaches [2,3], have made it possible to process various interesting nanostructures and to examine many non-classical phenomena that are absent in bulk materials. Nanostructures represent a new class of materials with properties different from bulk solid-state structures, and their unusual properties arise from the size-dependent quantum effects and the enhancement of surface states.

A promising application of nanostructured systems involves advanced thermoelectric materials. The search for good thermoelectric materials used to be an active field during the 1957 1965 period, after Ioffe's suggestion of using thermoelectrics as solid-state refrigerators [4]. However, the best thermoelectric material found in that period had only moderate performance efficiency, and there has been little progress in this field since then. Recently, Hicks and Dresselhaus predicted a dramatic enhancement

in thermoelectric performance with low-dimensional systems [5, 6]. The proposed improvement in the thermoelectric efficiency is associated with the enhanced density of states at the band edge in low-dimensional systems, the possibility to manipulate multiple anisotropic carrier pockets to optimize their thermoelectric performance, and the opportunities to increase phonon scattering at the quantum-confined interfaces. This promising prediction, along with the increasing demand for CFC-free, efficient and small power generators or refrigerators, has rendered the study of low-dimensional thermoelectric materials a rapidly growing field over the past few years.

1.2 Low-Dimensional Thermoelectricity

Evaluation of new materials for thermoelectric applications is usually made in terms of the dimensionless thermoelectric figure of merit ZT where T is the temperature (in Kelvin) and Z is given by

$$Z = \frac{S^2 \sigma}{\lambda}, \tag{1.1}$$

where S is the thermoelectric power or Seebeck coefficient, σ is the electrical conductivity and

$$\lambda = \lambda_e + \lambda_{ph}, \tag{1.2}$$

is the thermal conductivity, which includes contributions from carriers (λ_e) and the lattice (λ_{ph}). Large values of ZT require high S, high σ, and low λ. Since an increase in S normally implies a decrease in σ because of carrier density considerations, and since an increase in σ implies an increase in the electronic contribution to λ as given by the Wiedemann-Franz law, it is very difficult to increase Z in typical thermoelectric materials. The best commercial bulk thermoelectric material is $Bi_{0.5}Sb_{1.5}Te_3$ with a room temperature $ZT \sim 1$. It is believed that if materials with $ZT \sim 3$ could be developed, many more practical applications for thermoelectric devices would be realized. It should be noted that for a thermoelectric device to operate, both p-type and n-type elements are required to complete an electrical circuit. Simple thermo-
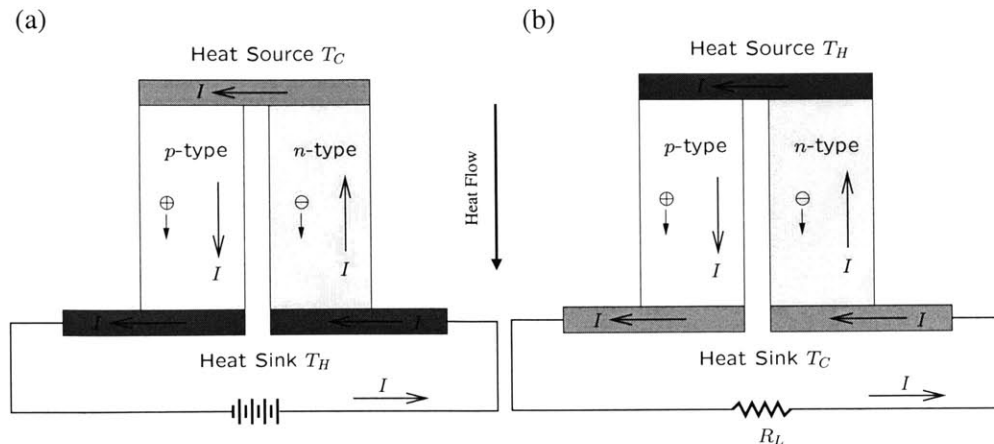
Figure 1-1: Schematic diagrams for simple (a) cooling and (b) energy conversion devices using thermoelectric materials.

electric cooling and energy conversion devices constructed with p-type and n-type components are schematically illustrated in Figs. 1-1(a) and (b), respectively.

Recently, research in thermoelectricity has entered into a new era with inspiration from band structure engineering and phonon engineering of low-dimensional structures [6, 7]. In these new materials, the dimension of the systems is comparable to or even smaller than the de Broglie wavelength of electrons, causing the emergence of quantized energy subbands that dramatically alter the electronic band structures and various properties. In addition, with the restricted dimensions shorter than the phonon mean free paths, the thermal conductivity contribution from the lattice is effectively reduced. Through carefully designed structures and optimal doping concentrations, it is possible to maintain the desirable thermoelectric properties of the bulk material, while significantly improving the thermoelectric efficiency for the low-dimensional systems.

The proof-of-principle demonstration of enhanced ZT in low-dimensional thermo-electrics has been carried out for 2D quantum well systems using $PbTe$-$Pb_{1-x}Eu_xTe$ superlattice [9] and strain-relaxed Si-$Si_{0.7}Ge_{0.3}$ superlattice [8, 10]. Figure 1-2 shows the experimental data of S^2n as a function of well thickness in the Si-$Si_{0.7}Ge_{0.3}$ superlattice system, compared to theoretical predictions. The agreement between the experimental results and theoretical prediction validates the theoretical transport

21
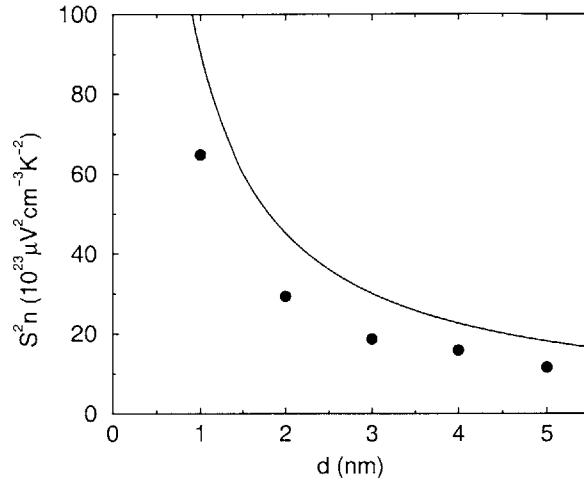
Figure 1-2: Comparison between experimental data (•) and theoretical prediction ( ) for $S^2 n$ vs. quantum well width d at the optimal doping level for a strain-relaxed $Si/Si_{0.7}Ge_{0.3}$ quantum well superlattice at room temperature [8].

model for these low-dimensional systems; the trend also gives convincing evidence for the enhanced thermoelectric performance in 2D systems. An extension of the previous results indicates that even higher ZT may be achieved in 1D and/or 0D systems. Figure 1-3 shows the calculated ZT for 1D Bi nanowires compared with 2D Bi thin films as a function of wire diameter and film thickness [8], respectively. This theoretical model predicts that 1D systems may possess ZT values of practical interest for thermoelectric devices.

In this thesis, we present a comprehensive theoretical and experimental study of the thermoelectric properties of 1D Bi and $Bi_{1-x}Sb_x$ nanowires. Bi and its alloy are chosen for this research because of their very small electron effective masses ($\sim$ 0.001 m_0, where m_0 is the free electron mass), long carrier mean free path ($\sim$ mm at 4 K), and large carrier anisotropy, which allow for the observation of quantum effects at a relatively large wire diameter ($\sim$ 50 nm) and provide for the possibility of carrier pocket engineering to optimize the thermoelectric performance of nanowires.

It is possible that additional ZT enhancement may occur in 0D systems, e.g. quantum dot systems. Recently, an unusually large Seebeck coefficient was measured in a $PbSe_x Te_{1-x}/PbSe$ quantum-dot superlattice at 300 K ($ZT \sim 2$) [11]. This experimental observation pointed out a potential way to utilize quantum dot systems for
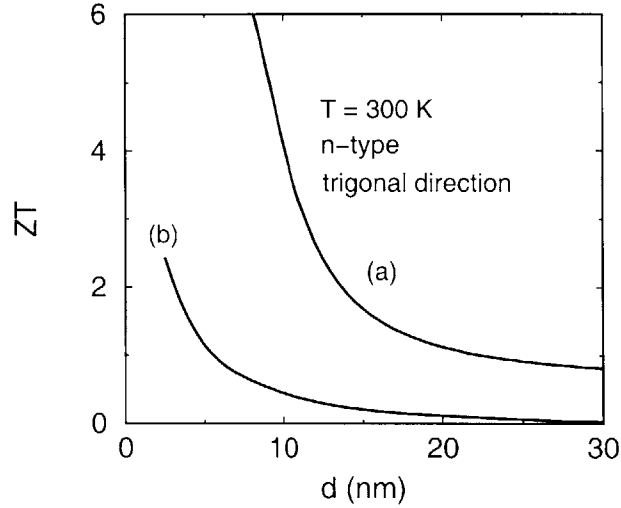
Figure 1-3: Calculated ZT for (a) Bi nanowires and (b) Bi thin films as a function of wire diameter and film thickness, respectively [8].

thermoelectric applications. We propose in this thesis a novel structure that arranges quantum dots in a systematic way in the form of a superlattice nanowire. A theoretical framework for the transport behavior will be developed for superlattice wires consisting of quantum dots, and the thermoelectric properties will be predicted.

1.3 Thesis Outline

The first part (Chapters 2–4) of the thesis is focused on the studies of Bi and $Bi_{1-x}Sb_x$ nanowires, and the second part (Chapter 5) is devoted to the theoretical investigation of superlattice nanowires.

Chapter 2 describes the fabrication process of Bi-related nanowire arrays. Characterization of the nanowires using various techniques, including scanning electron microscopy (SEM), transmission electron microscopy (TEM), X-ray diffraction (XRD), and energy dispersive X-ray (EDX) spectroscopy, will be discussed.

Chapter 3 presents a general theoretical framework to model the electronic band structure and transport properties of nanowires, taking into consideration the quantum

confinement effects due to cylindrical wire boundary and the effect of anisotropic carriers. The theoretical model is then applied to $Bi_{1-x}Sb_x$ nanowires to investigate their unique semimetal-semiconductor transition and the potential for thermoelectric applications.

Chapter 4 is devoted to the experimental study of transport properties of $Bi_{1-x}Sb_x$ nanowires as a function of temperature, wire diameter, Sb content, and magnetic field. The transport measurements not only provide valuable information to validate theoretical assumptions and model calculations, but also demonstrate the enhanced thermoelectric performance of $Bi_{1-x}Sb_x$ nanowires. The theoretical model is then extended to other nanowires, such as Te-doped Bi nanowires and Sb nanowires, in order to examine their transport behavior and interpret the experimental findings.

Chapter 5 presents a general theoretical model for the electronic structure and transport properties of superlattice nanowires made of interlaced quantum dots. It explicitly takes into account the cylindrical wire boundary conditions, the diameter-dependent band offsets for the periodic potential along the wire axis, and the multiple types of anisotropic carriers. The established transport model is utilized to study the thermoelectric properties of superlattice nanowires of various lead salts (PbS, PbSe, and PbSe) to elucidate their performance dependence on the segment length, wire diameter, crystal orientation along the wire axis, and the length ratio of the constituent nanodots.

Lastly, conclusions of this thesis are presented along with suggestions for future research in Chapter 6.

Chapter 2

Fabrication and Characterization of Bi-related Nanowires

2.1 Introduction

Recently, nanowires have received growing attention because of their importance as low-dimensional systems and their potential in nanotechnology applications. Nanowires are quantum-confined in two dimensions, while the electrical conduction is allowed along the wire axis. Because of their unique density of electronic states, nanowires are expected to exhibit significantly different optical [12–15], electrical and magnetic [16, 17] properties from their bulk 3D crystalline counterparts. The increased surface-to-volume ratio, the very high density of electronic states near the energies of their van Hove singularities, the diameter-dependent band structures, and the increased surface scattering for electrons and phonons are some of the unique properties exhibited by nanowires that may be beneficial for certain applications. Nanowires have also been shown to provide a promising framework for applying the "bottom-up" approach [18] in the design of complicated nanostructures.

The preparation of 1D quantum systems represents one of greatest challenges in materials fabrication. The synthesis of highly crystalline and continuous nanowires is essential for studying the interesting quantum phenomenon in these low-dimensional systems. Over the last decade, significant progress has been made in deriving

nanowires via techniques such as high-pressure injection [2, 19–21], vapor deposition [22, 23], electrochemical deposition [16, 24–38], laser ablation [39 43], thermal evaporation [44, 45], molecular beam epitaxy [46, 47], and electron beam lithography [48]. These different methods led to the generation of a broad range of 1D nanostructured materials. Although some approaches are more suitable than others for specific applications, each approach may present certain limitations in fabrication with regard to nanowire diameter, crystallinity, fabrication costs and scalability. A comprehensive discussion on nanowire synthesis techniques is given by Refs. [49] and [50].

Since the present project is in part motivated by thermoelectric applications of low-dimensional systems, several factors are further considered. First, in order to carry a high electrical current density, it would be favorable to have a large number of parallel nanowires connected. Secondly, in thermoelectric applications, it is desirable to minimize the thermal conductivity and maximize the electrical conductivity. Therefore, the thermal conductivity of the host material should be small, and a high crystallinity in the nanowires is desired to achieve a high electrical conductivity.

The template-assisted synthesis of nanowires is a conceptually elegant way of fabricating nanostructures with the above characteristics in a self-organized assembly [19, 35, 51–54]. The template is typically a nonconducting host matrix with nanometer-sized elongated pores or voids, which can be filled by the material of choice. Templates that have been used for nanowire synthesis include anodic alumina (Al_2O_3), nano-channel glass [53], ion track-etched polymers and mica films [55]. Recently, diblock copolymers [56] that consist of two different polymer chains with dissimilar properties have also been utilized as templates for nanowire growth. During the segregation of the two phases, spheres, cylinders and lamellae are formed, depending on the volume ratio of the two polymer chains. By applying an electric field while the copolymer is heated above the glass transition temperature, the self-assembled cylinders could be aligned with their main axis perpendicular to the film.

In this study, Bi and $Bi_{1-x}Sb_x$ alloy nanowires were synthesized within the nano-channels of anodic alumina templates, which possess excellent chemical and

mechanical stability, controlled pore structures, and low thermal conductivity, which is favorable for thermoelectric applications. The wide bandgap of anodic alumina ($\sim$ 3.2 eV) also makes it an excellent host material for quantum wires.

Several techniques have been developed for filling the voids of porous templates with the desired materials, including vacuum melting and pressure injection [2, 19, 21], vapor deposition [22] and electrochemical deposition [34, 38]. For Bi-related alloys, the pressure injection technique is found to produce nanowires with consistently high crystalline quality down to a wire diameter of 13 nm. Due to the high thermal stability of the alumina template (up to 800 °C), this high-pressure injection approach can be readily extended to the nanowire fabrication of other materials with a low melting point. While it is possible to fabricate nanowires with smaller diameters by electrochemical deposition [57] or vapor-phase deposition [58] in nanochannel templates, these filling techniques produce polycrystalline nanowires with small grains, and post-annealing treatments are usually required to improve their crystallinity.

In this study, we use vacuum melting and high-pressure injection to fabricate Bi-based nanowire arrays in anodic alumina templates. In the following sections, the fabrication process of anodic alumina templates and Bi-based nanowires is presented, and the characterization results of these Bi-based nanowires are discussed.

2.2 Synthesis of Porous Anodic Alumina Templates

In this section, we briefly present the procedures and conditions used to fabricate porous anodic alumina templates. Readers are referred to Refs. [2] and [49] for a more detailed description.

In the processing of anodic alumina films, a thin aluminum sheet is first mechanically and electrochemically polished to produce a smooth surface. It is then anodized in an acidic electrolyte solution [59–61] at a constant voltage and temperature. The experimental set-up for the anodization process is shown in Fig. 2-1. An ice bath is used since the temperature for the anodization process is usually kept low. Under
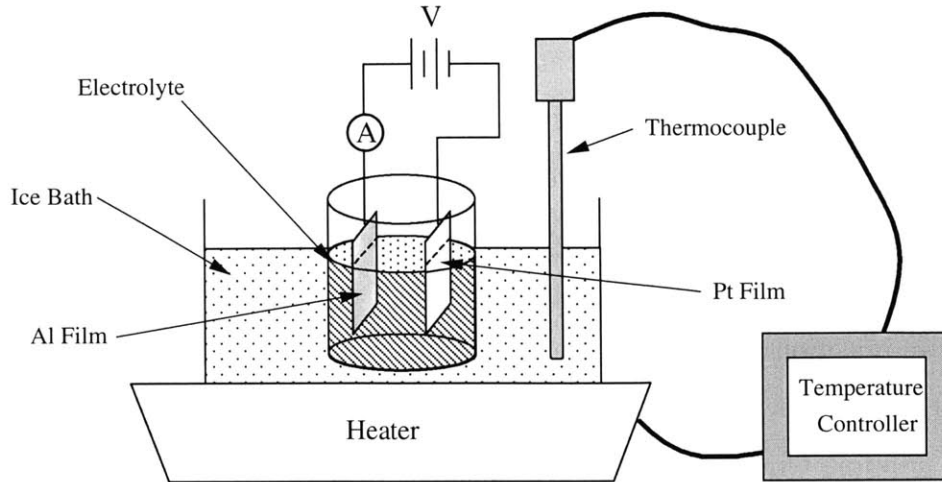
Figure 2-1: Schematic of the experimental set-up for anodization of aluminum.

carefully chosen anodization conditions, oxide films possessing a regular hexagonal array of parallel and nearly cylindrical channels are obtained (see Fig. 2-2(a)). The anodization voltage V determines the interpore distance D by an empirical relation: $D(\text{nm})= -1.7+2.81 \times V(\text{volts})$ [61]. Different electrolytes are usually used for different anodization voltage ranges: $20\,\text{wt}\%$ sulfuric acid (H_2SO_4) for $\leq 20\,\text{V}$, $4\,\text{wt}\%$ oxalic acid ($H_2C_2O_4$) for 30–$65\,\text{V}$, and $3.5\,\text{wt}\%$ phosphoric acid (H_3PO_4) for $\geq 70\,\text{V}$. The as-prepared anodic alumina film has open pores on the top surface of the substrate and is capped by a barrier layer on the other side (see Fig. 2-2(a)).

The self-organization of the pore structure in an anodic alumina template involves two coupled processes: pore formation with uniform diameters and pore ordering. The pores are formed with a uniform diameter because of a delicate balance between the electric-field-enhanced diffusion that determines the growth rate of alumina, and the dissolution of alumina into the acidic electrolyte [60]. The pores are believed to self-order because of mechanical stress at the aluminum-alumina interface due to expansion during anodization. This stress produces a repulsive force between the pores, causing them to arrange in a hexagonal lattice [62]. Depending on the an-odization conditions, the pore diameter can be systematically varied from $< 10\,\text{nm}$ to $200\,\text{nm}$ with a pore density of 10^9–10^{11} pores/cm^2 [19, 59, 60, 63]. With recent im-
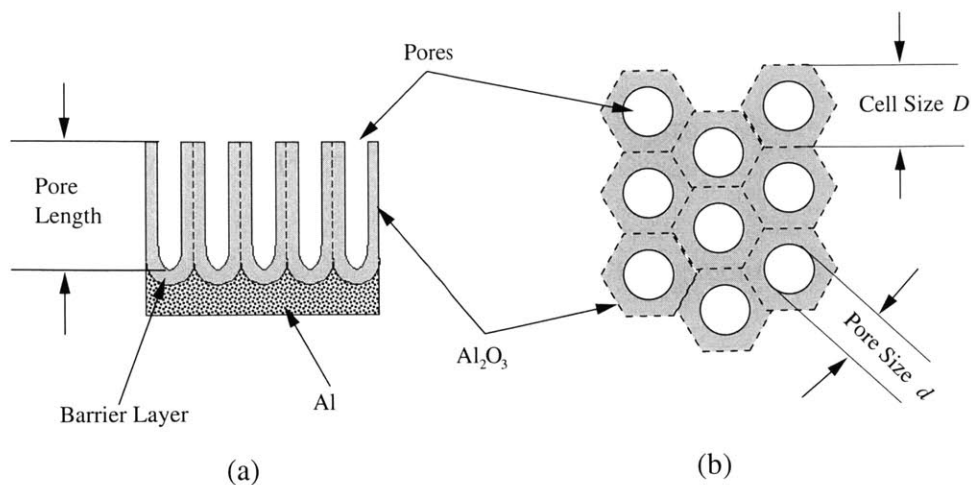
Figure 2-2: Schematic diagrams illustrating the structure of an anodic alumina template: (a) side view and (b) cross-sectional view.

provements on the degree of pore ordering, anodic alumina templates have stimulated much interest in device applications [64–69] because they provide a highly ordered 2D nanopattern readily and inexpensively on a larger scale than conventional lithographic approaches.

The pore size distribution and pore ordering of anodic alumina templates can be significantly improved by a two-step anodization technique [70, 71], whereby the alumina layer is dissolved after the first anodization in an acidic solution, followed by a second anodization under the same conditions (see Fig. 2-3). Figures 2-4(a) and (b) show scanning electron microscopy (SEM) images of the surfaces of porous alumina templates anodized in 4 wt% oxalic acid and 20 wt% sulfuric acid, respectively. The ordering and uniformity of the pores shown in Fig. 2-4 have been optimized by the two-step anodization technique [70, 71]. The processing conditions for the second anodization process for templates (a) and (b) shown in Fig. 2-4 are listed in Table 2.1.
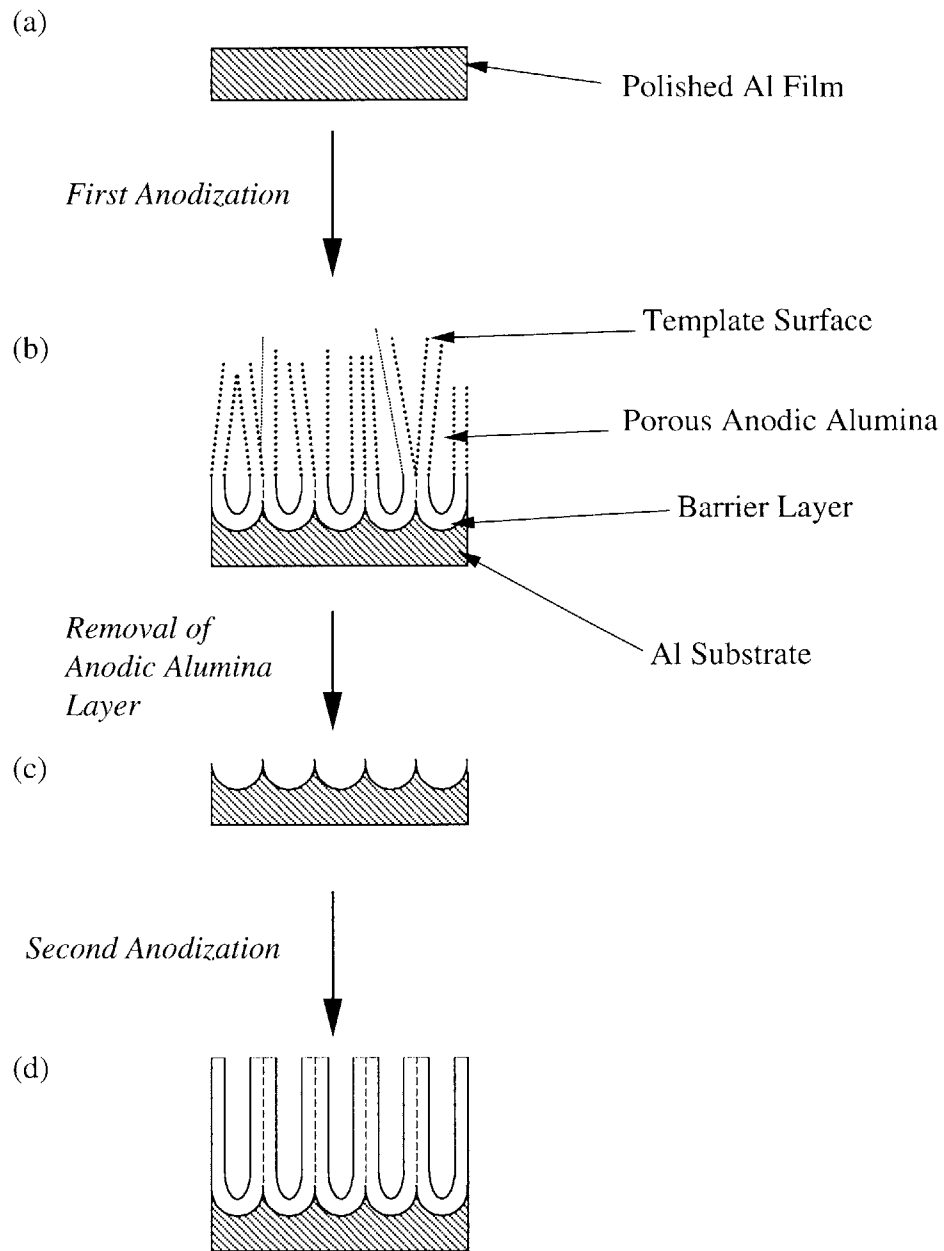
Figure 2-3: Schematic of the two-step anodization process: (a) a mechanically and electrochemically polished Al substrate at the start of the anodization, (b) porous anodic alumina layer produced in the first anodization, (c) textured Al substrate surface after removal of the anodic alumina layer in (b), and (d) porous anodic alumina template produced in the second anodization.
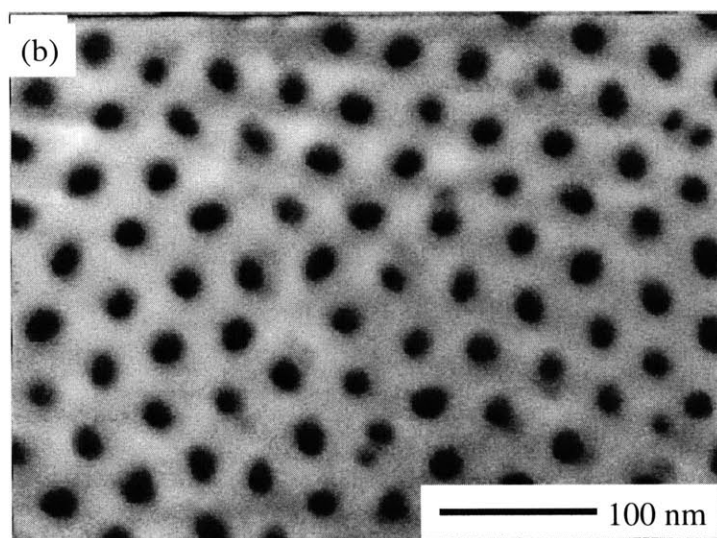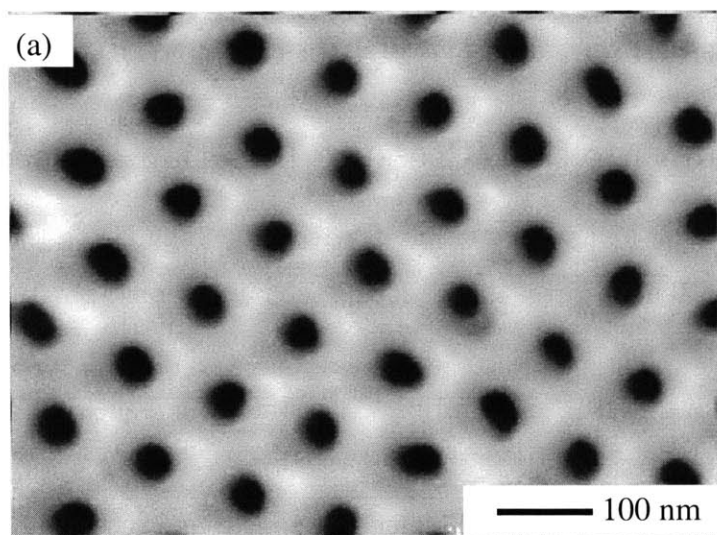
Figure 2-4: SEM images of the top surfaces of porous anodic alumina templates after the second anodization in (a) 4 wt% $H_2C_2O_4$ and (b) 20 wt% H_2SO_4. The average pore diameters in (a) and (b) are 44 nm and 18 nm, respectively.

Table 2.1: The second anodization conditions for anodic alumina templates shown in Fig. 2-4. The sample shown in Fig. 2-4(b) was also immersed in 20 wt% H_2SO_4 for 20 minutes for pore enlargement following the second anodization.

Sample	Electrolyte	Volt. (V)	Temp. (°C)	Current (mA/cm²)	Duration (min)
Fig. 2-4(a)	4 wt% $H_2C_2O_4$	45.0	19	11	250
Fig. 2-4(b)	20 wt% H_2SO_4	20.0	0–13	22–32	120

2.3 Preparation of Bi-related Nanowires

2.3.1 Vacuum Melting/Pressure Injection Process

To produce $Bi_{1-x}Sb_x$ nanowires, we used a technique similar to that developed for synthesizing pure Bi nanowires [19], replacing the pure Bi metal by the $Bi_{1-x}Sb_x$ alloy in the pressure injection process.

The metal alloys used in pressure injection were prepared by mixing high-purity Bi (99.9999%, Alfa Aesar) and Sb (99.9999%, Alfa Aesar) in a quartz tube, which was then evacuated and sealed. The sealed tube was then heated to 650°C for 8 hours with constant agitation to facilitate homogenization of the melt. The melt was then quenched in cold water to prevent possible segregation. This vacuum sealing-melting-quenching technique was found to be effective in producing an oxygen-free $Bi_{1-x}Sb_x$ alloy.

For the pore-filling processes, the anodic alumina template was placed in a glass beaker and fixed to the bottom of the container by pure Al (99.999%, Alfa Aesar) and Cu (99.999%, Alfa Aesar) wires. The Al wires have essentially zero solubility in liquid Bi at the temperatures used in the pressure injection process ($T \leq 325°C$), while Cu has a small solubility ($\sim 0.2\,at\%$) in liquid Bi at 325°C. The latter was introduced to reduce the surface tension of Bi, thus facilitating Bi injection into the nanochannels of the anodic alumina template [19, 72].

Figure 2-5 shows a schematic of the experimental set-up for pressure injection. The chamber employed was a Parr high-pressure reactor that could sustain a pressure of up to $\sim 5500\,psi$. It was attached to a vacuum pump that could achieve $10^{-2}\,mbar$, and was heated to 240°C for 8–10 hours to evacuate the channels of the alumina template. After degassing, the temperature was slowly ramped up (by $\sim 1°C/min$) to 325°C to melt the $Bi_{1-x}Sb_x$ alloy, which has a melting point of $\sim 271°C$. The reactor was maintained at this temperature for two hours for the system to reach equilibrium. Before pressure injection, the vacuum pump was removed from the chamber, and a high-pressure Ar gas cylinder (6000 psi, BOC Gases) was connected to the inlet valve of the chamber instead. Ar gas was then introduced into the chamber to increase the
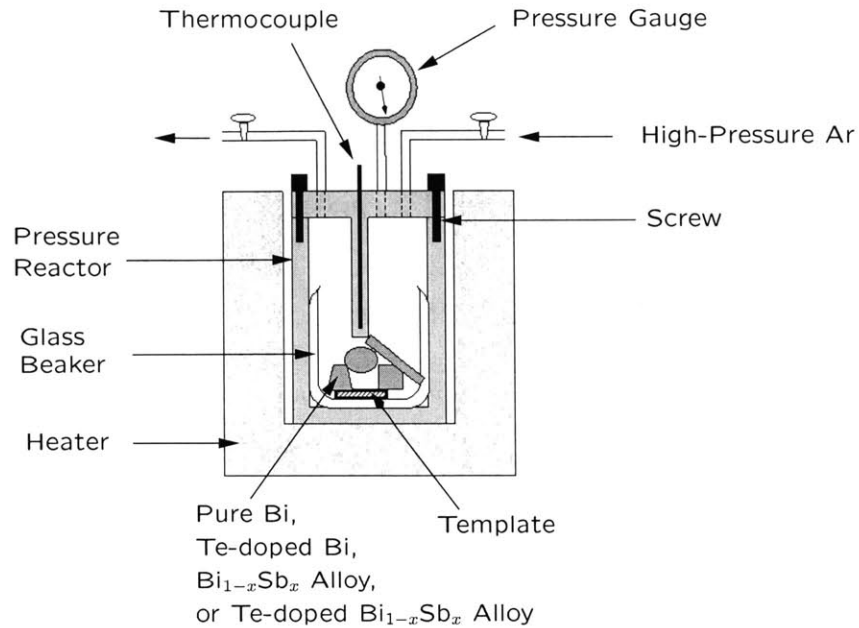
Figure 2-5: Schematic of the experimental set-up for the pressure injection of Bi-related alloy into the pores of an anodic alumina template [19]. The metal charge could be pure bismuth, Te-doped Bi, $Bi_{1-x}Sb_x$ alloy or Te-doped $Bi_{1-x}Sb_x$ alloy.

pressure to 4500 psi for the pressure injection of liquid alloy into the nanochannels of the anodic alumina template. After 5 hours, the chamber was slowly cooled down to room temperature over a 12-hour period, and the $Bi_{1-x}Sb_x$ alloy was allowed to crystallize within the nanochannels. The slow cooling process was found to be critical towards producing single-crystal nanowires. Although a small amount of Cu was introduced into liquid Bi to enhance the filling of nanochannels, the Cu atoms should be segregated from Bi upon solidification, since Cu has zero solubility in solid Bi. The Cu flakes rose to the top surface of Bi after solidification due to their lower density, leaving pure Bi nanowires within the nanochannels. As will be shown in Chapter 4, Bi nanowires fabricated by the vapor deposition and the pressure injection techniques possess similar transport properties, indicating that the introduction of Cu impurities during the liquid injecting process does not affect the transport properties of the Bi-related nanowires. The absence of Cu impurities in these Bi-related nanowires was further confirmed by the energy dispersive X-ray (EDX) spectroscopy analysis of

33

nanowire arrays under the SEM environment, which showed no Cu signals within the detection limit.

2.4 Characterization of Bi-related Nanowires

2.4.1 SEM and TEM Characterization

To ensure that the $Bi_{1-x}Sb_x$ alloy was injected as nanowires from the top surface all the way to the bottom side of the anodic alumina template, the bottom surface of the Bi/Al_2O_3 nanocomposite was examined by a scanning electron microscope (SEM) after removal of the barrier layer and the underlying Al substrate. Figure 2-6 presents the SEM image of a nanowire array with an average wire diameter of 45 nm, showing that more than 80% of the pores were filled. For templates with pore diameters smaller than 40 nm, however, the filling factor declines rapidly with decreasing wire diameter d_w because the pressure required to fill the pores varies as $1/d_w$. It is found that for a template with a pore diameter of less than 10 nm, the filling factor becomes lower than 10%, rendering other filling processes more attractive for this pore diameter range.

The crystal quality and structural characteristics of these $Bi_{1-x}Sb_x$ nanowires were studied by high-resolution transmission electron microscopy (HRTEM) using a JEOL 2010 high-resolution TEM operated at 200 kV. Figure 2-7 shows a HRTEM image of a free-standing $Bi_{1-x}Sb_x$ nanowire that was removed from the alumina template. Free-standing nanowires were derived by dissolving the alumina template at 20°C in an acid solution of 3.5 vol% H_3PO_4 plus 45 g/l CrO_3, which does not attack the $Bi_{1-x}Sb_x$ nanowires. In Fig. 2-7, the lattice fringes of a typical nanowire can be seen, clearly indicating its high crystallinity. HRTEM studies show that most of the $Bi_{1-x}Sb_x$ nanowires are single crystals, and no grain boundaries are observed. The single crystallinity is further supported by selected-area electron diffraction (SAED) experiments. Fig. 2-8 shows a SAED pattern taken from the same nanowire. The
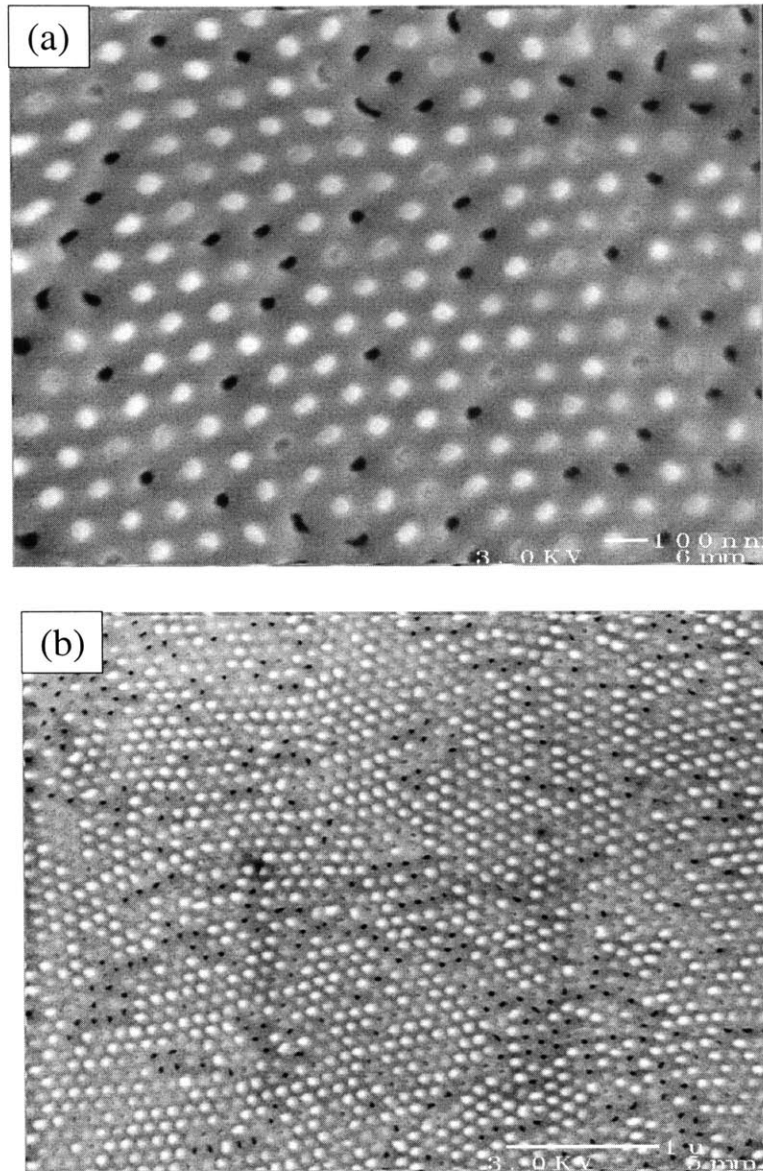
Figure 2-6: Two SEM micrographs of (a) high and (b) low magnifications of the bottom surface of a nanowire array after the barrier layer was removed. The alumina template was prepared in $4\,\mathrm{wt\%}$ $H_2C_2O_4$ and has an average pore diameter of $\sim 45\,\mathrm{nm}$. Most of the pores have been thoroughly filled with $Bi_{1-x}Sb_x$ alloy (shown as bright spots).
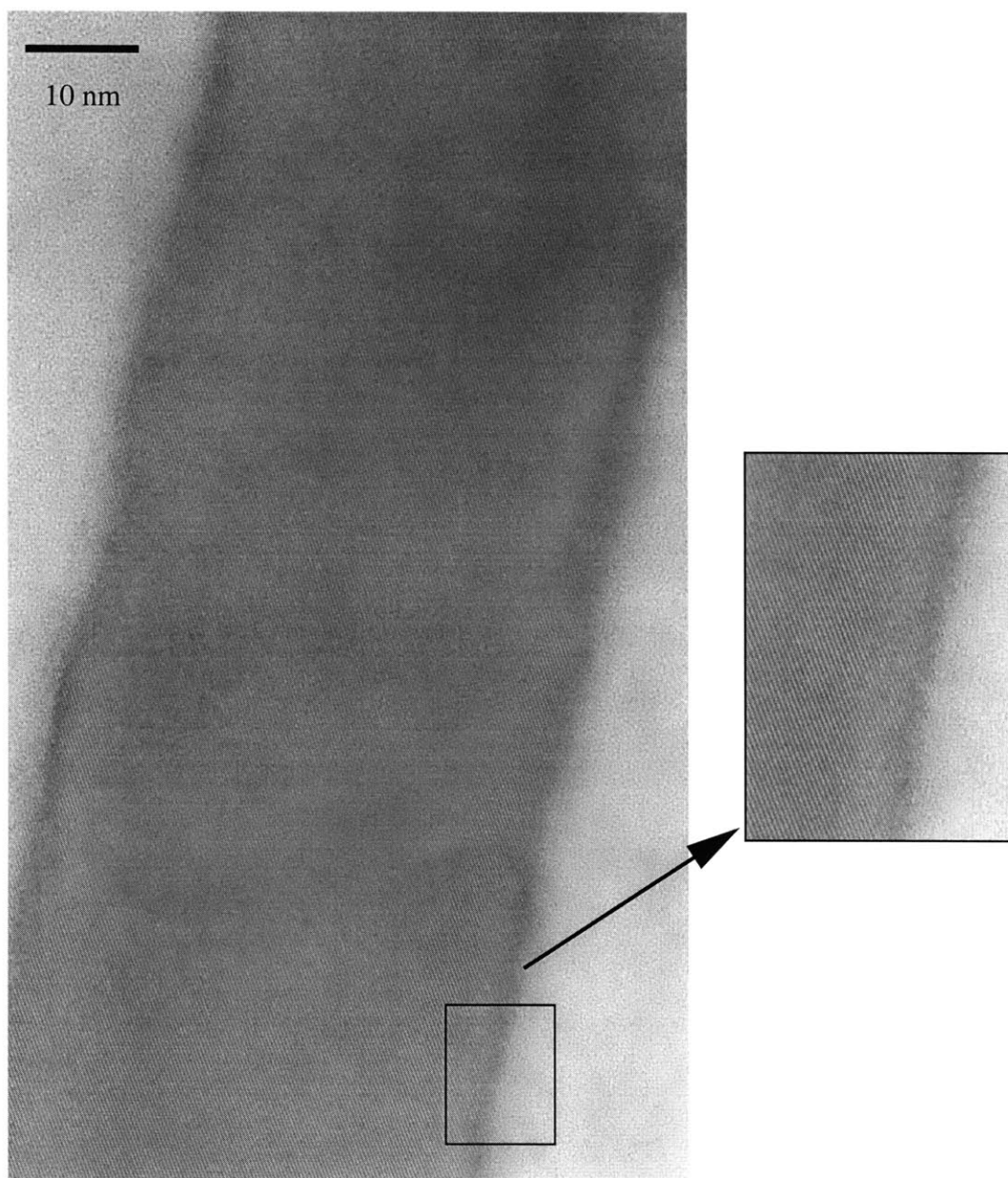
Figure 2-7: HRTEM image of a free-standing $Bi_{1-x}Sb_x$ nanowire with a diameter of ~ 45 nm and a nominal Sb content of 15 at%. The inset highlights the lattice fringes of the nanowire, indicating high crystallinity. The amorphous layer on the nanowire surface is the oxide of $Bi_{1-x}Sb_x$ alloy.

Figure 2-8: Selected-area electron diffraction pattern of the nanowire shown in Fig. 2-7.

discrete diffraction spots in the SAED pattern result from a single crystalline grain, indicating the high crystallinity of the nanowire.

In Fig. 2-7, a thin amorphous coating was noted on the $Bi_{1-x}Sb_x$ nanowire. This was found to be the oxide of $Bi_{1-x}Sb_x$ alloy, which might have resulted from the oxidation of $Bi_{1-x}Sb_x$ nanowire upon removal of the alumina template and/or exposure to air, and the thickness of this oxide layer was found to be independent of the Sb content. Although this oxide coating may protect the crystalline core of the nanowire from further oxidation, it presents a substantial challenge in the electrical measurements of free-standing nanowires [73].

2.4.2 Compositional Analysis by EDX

For $Bi_{1-x}Sb_x$ alloy nanowires synthesized by pressure injecting liquid alloys into a porous template, it is important to determine the actually Sb content in the nanowires. The Sb content and distribution within the nanowire are critical factors that influence various transport properties of $Bi_{1-x}Sb_x$ alloy nanowires.

The EDX capability of a TEM instrument provides a valuable and non-destructive tool for elemental analysis of a single nanowire. By striking the specimen with high-energy electron beams, a X-ray spectrum consisting of the characteristic peaks of
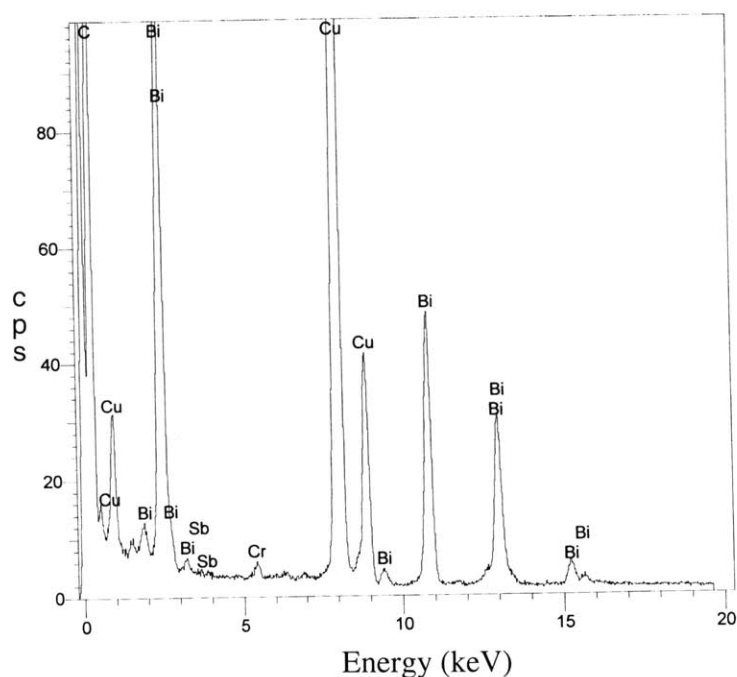
Figure 2-9: EDX spectrum of a free-standing $Bi_{1-x}Sb_x$ nanowire with a diameter of 45 nm and a nominal Sb content of 15 at%.

constituent elements can be obtained, and the peak intensity can be quantified to determine the concentration ratio of different chemical elements by comparison to a standard. Since the electron beam used in the TEM has a diameter as small as several nm, this technique can be employed to investigate the compositional distribution along the wire axis, which is usually on the order of tens of microns for our $Bi_{1-x}Sb_x$ nanowires.

Figure 2-9 shows the EDX spectrum of a free-standing 45-nm $Bi_{1-x}Sb_x$ nanowire using an electron beam diameter of 25 nm. Besides the characteristic peaks of Bi and Sb, Cu signals were detected from the TEM grid used for holding the nanowire sample. The Cr peaks were due to residues of the acid solution (Cr_2O_3 + H_3PO_4) used for dissolving the alumina template. By quantifying the peak intensities of Bi and Sb in Fig. 2-9, the Bi and Sb contents in the nanowire were calculated to be 84.5 at% and 15.5 at%, respectively, which are in good agreement with that of the bulk alloy used for the pressure injection of nanowires (85.0 at% and 15.0 at%, respectively). To examine the homogeneity of the nanowires, the EDX analysis was performed at various spots along the nanowire. As indicated in Fig. 2-10, we found

38

16.6 at% Sb
83.4 at% Bi

16.5 at% Sb
83.5 at% Bi

15.0 at% Sb
85.0 at% Bi

15.5 at% Sb
84.5 at% Bi
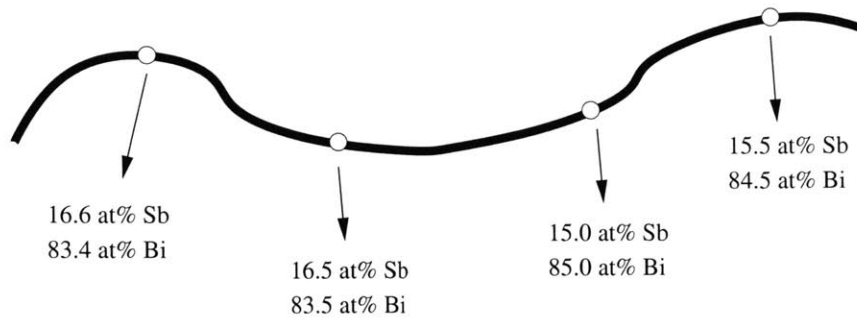
Figure 2-10: EDX analysis at four different spots along the wire axis of a free-standing $Bi_{1-x}Sb_x$ nanowire with a nominal Sb content of 15 at%. The wire diameter was $\sim 45\,nm$ and the electron beam diameter is $25\,nm$. The results showed that the actual Sb content in the nanowire was $15.8\,at\% \pm 0.8\,at\%$.

that the Sb content was fairly constant along the wire length with values within 2% of the nominal Sb content of the bulk alloy.

The results from the EDX studies of $Bi_{1-x}Sb_x$ nanowires are of great significance because they confirm that these nanowires not only have a similar composition to the alloy pieces used for the pressure injection, but also possess a uniform compositional distribution throughout the entire wire. Since the electronic and transport properties of these $Bi_{1-x}Sb_x$ nanowires are expected to be highly dependent on the Sb content (see Chapter 3), the information on the nanowire composition forms the basis of the fundamental assumptions for the theoretical models developed on these nanowires.

The determination of the Te dopant concentration in Te-doped $Bi_{1-x}Sb_x$ nanowires using the EDX analysis was, however, not feasible. The Te dopant concentration in these nanowires was typically on the order of $0.1\,at\%$ for samples of interest for thermoelectric applications. This concentration was below the detection limit ($\sim 1\,at\%$) of the EDX instrument. Therefore, other techniques that are more sensitive to the Te dopants, e.g., the electrical transport or optical measurements, should be employed to determine the Te dopant content in doped $Bi_{1-x}Sb_x$ nanowires.
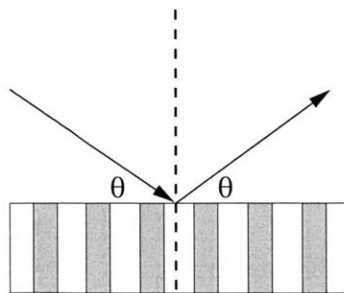
Figure 2-11: Schematic of the set-up for XRD experiments, illustrating the orientation of the nanowire array relative to the X-ray beam.

2.4.3 XRD Study of Bi-related Nanowire Arrays

The crystal structure of the $Bi_{1-x}Sb_x$ nanowires was investigated by X-ray diffraction (XRD) with the reflection plane perpendicular to the wire axis. The XRD studies were performed on a θ-θ diffractometer (Siemens D5000, 45 kV, 40 mA, Cu-Kα) using an experimental set-up depicted in Fig. 2-11.

Figure 2-12 shows the XRD patterns of pure Bi nanowire arrays of three different wire diameters. It illustrates that the crystal structure of these nanowires is the same as that of bulk Bi, and no separate Cu phase is present. We note that since Cu has zero solubility in solid Bi, it is expected that Cu atoms would segregate to the nanowire surface and/or form nanocrystals that may be detected by the XRD experiments if present, rather than producing point defects in the nanowires. Figure 2-12 also indicates that the nanowire arrays possess a preferred wire orientation that is dependent on their wire diameters. The major orientations of the 95-nm and 40-nm Bi nanowire arrays are normal to the (202) and (012) lattice planes, respectively, which are denoted as $[10\bar{1}1]$ and $[01\bar{1}2]$ using the hexagonal lattice structure notation. These results suggest that the majority ($> 80\%$) of the Bi nanowires are oriented along the $[10\bar{1}1]$ and $[01\bar{1}2]$ directions for $d_w \geq 60$ nm and $d_w \leq 50$ nm, respectively. The existence of more than one dominant orientation in the 52-nm Bi nanowires (Fig. 2-12(b)) is attributed to the transitional behavior of nanowires with *intermediate* diameters as the preferential growth orientation is shifted from $[10\bar{1}1]$ to $[01\bar{1}2]$ with decreasing d_w. On the other hand, Huber *et al.* have synthesized 30-nm Bi nanowires using a much higher pressure of $> 20,000$ psi, and their nanowires show a different
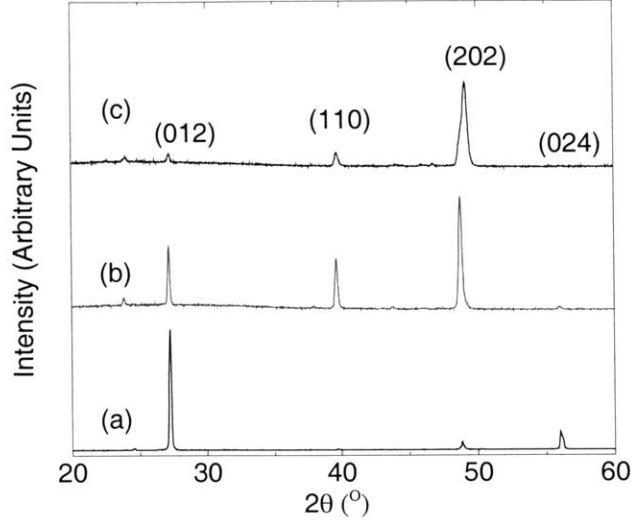
Figure 2-12: XRD patterns of Bi/anodic alumina nanocomposites with average Bi wire diameters of (a) 40 nm, (b) 52 nm and (c) 95 nm. The XRD peaks of all three samples appeared at the same positions as those of the polycrystalline Bi standard, and the resulting lattice constants were equal to those of bulk Bi within 0.3 %. The Miller indices corresponding to the lattice planes of bulk Bi are indicated above the individual peaks.

crystal orientation of (001) along the wire axis [74], indicating that the preferred crystal orientation may also depend on the pressure applied. From XRD studies, Zhang $et\ al.$ also found that there is a metastable high-stress phase in the as-prepared nanowires [19], which can be transformed into the normal Bi phase by a thermal annealing treatment.

Figure 2-13 shows the XRD patterns of $Bi_{1-x}Sb_x$ nanowire arrays with different Sb contents. The wire diameters of the three samples in Fig. 2-13 were all about 40 nm. We note that the XRD peak positions as well as the relative peak intensities of the $Bi_{1-x}Sb_x$ nanowire arrays were similar to those of the pure Bi nanowire array, indicating that alloying Bi with $\leq$ 15 at% Sb did not affect the crystal structure of Bi, and the dominant crystal orientation along the wire axes was perpendicular to the (012) lattice plane for these 40-nm nanowire arrays, although the transition diameter for the preferred growth orientation may change in the $Bi_{1-x}Sb_x$ nanowires.

XRD studies of the Bi-related nanowires indicated that the rhombohedral crystal structure of bulk Bi was preserved in the nanowires. This result has important im-

41
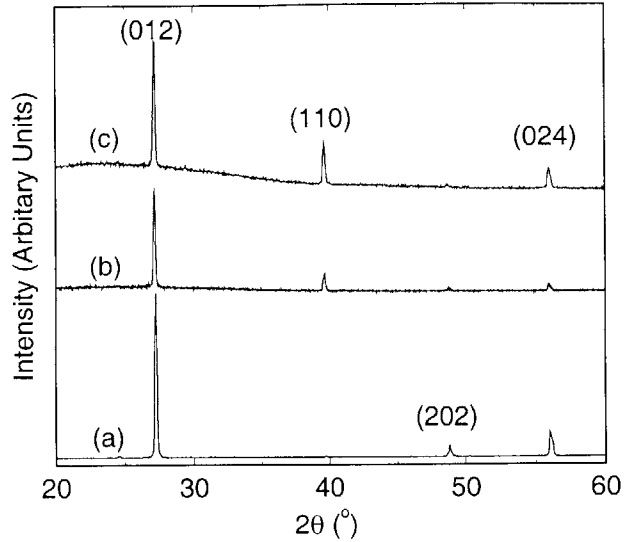
Figure 2-13: XRD patterns of 40-nm $Bi_{1-x}Sb_x$ nanowire arrays with $x =$ (a) 0.0, (b) 0.10 and (c) 0.15. The Miller indices corresponding to the lattice phases of bulk Bi are indicated above the individual peaks.

plications for transport-related experiments, since it suggests that the unique band structure and electronic properties of bulk Bi are retained in these nanowires. As the carrier pockets of Bi are highly anisotropic, the preferred crystal orientation provides valuable information on the electronic states of Bi-related nanowire systems. The crystal structure of Bi is characterized by three orthogonal principal axes, the binary, bisectrix and trigonal axes. The two preferred directions for Bi nanowires of different wire diameters both lie in the trigonal-bisectrix plane, with the $[10\bar{1}1]$ and $[01\bar{1}2]$ directions making $71.87°$ and $56.5°$ angles to the trigonal axis, respectively. We note that since these preferred crystallographic orientations obtained in our nanowires are not along the highest symmetry direction, the degeneracy of various materials properties in bulk $Bi_{1-x}Sb_x$ alloy is lifted in the nanowires, which can be utilized to provide valuable information on the anisotropy of important attributes.

Chapter 3

Theoretical Model for Bi and Bi$_{1-x}$Sb$_x$ Nanowires

3.1 Introduction

Nanostructured materials have received a great deal of research interest because they are expected to exhibit very different properties from their bulk counterparts due to quantum confinement effects. The ability to tailor materials properties by exploiting quantum confinement effects [6] not only provides a promising approach for novel device fabrication, but also creates possibilities for fundamental studies on nanotechnology [35].

Bi is attractive for transport studies as low-dimensional systems for the following reasons. The electrons in Bi are distributed in three highly anisotropic carrier pockets at the L points of the Brillouin zone, and the holes are contained in one pocket at the T point [75, 76]. Quantum confinement effects can be readily observed in Bi at a larger length scale ($\sim 50\,\mathrm{nm}$) [22] than most metals and semiconductors. Bi$_{1-x}$Sb$_x$ alloys form substitutional solid solutions, and the band structure of these alloys changes gradually from that of Bi to that of Sb as x increases [77, 78]. Thus, Bi$_{1-x}$Sb$_x$ nanowires constitute a unique 1D system in which the band structure and other related properties can be tailored by combining the quantum confinement effects with the Sb alloying effects.

In this chapter, a general theoretical framework is developed to derive the electronic band structure of nanowires and their transport properties, taking into consideration the quantum confinement effects due to the cylindrical wire boundary and the effect of anisotropic carriers. The theoretical model is then applied to $Bi_{1-x}Sb_x$ nanowires to investigate their semimetal-semiconductor transition and their potential for thermoelectric applications.

3.2   Theoretical Formalism

1D quantum wires are different from bulk materials in that the carriers (i.e. electrons or holes) are confined in two directions and constrained to only move along the wire axis. This confinement causes the allowed in-plane carrier energies to be quantized, which alters their properties dramatically. Thus, it is important to understand how the quantum confinement effects modify the band structure when a bulk material is shaped into a nanowire, and the information is essential for predicting various properties of the nanowires and in designing optimal thermoelectric devices.

A general theoretical framework and numerical solutions for the energy spectrum of anisotropic carriers in cylindrical nanowires have been previously developed in Ref. [79]. In this section, we summarize the important findings in Ref. [79], and consider the effect of magnetic field on the energy levels in a nanowire system.

3.2.1   Band Structure of a Homogeneous Nanowire in the Absence of Magnetic Fields [79]

A bulk material is considered where the majority carriers are electrons with an effective mass $\mathbf{m_e}$. In general, the electron masses are anisotropic, and the effective mass is expressed as a symmetric second-rank tensor $\mathbf{m_e}$. The dispersion relation of the electrons is written as

$$E(\mathbf{k}) = \frac{\hbar^2}{2}\mathbf{k} \cdot \boldsymbol{\alpha} \cdot \mathbf{k}, \qquad (3.1)$$

where $\mathbf{k}$ is the wavevector and $\boldsymbol{\alpha}$ is the inverse tensor of $\mathbf{m_e}$. From the effective mass theorem, the envelope wavefunction of electrons, $\psi(\mathbf{r})$, is described by the Schrödinger equation,

$$-\frac{\hbar^2}{2}\boldsymbol{\nabla}\cdot\boldsymbol{\alpha}\cdot\boldsymbol{\nabla}\psi(\mathbf{r}) = E\psi(\mathbf{r}). \qquad (3.2)$$

For nanowires embedded in an insulating matrix with a large band gap (e.g., alumina or mica), electrons are well-confined within the wires. Thus, to a good approximation, the electron wavefunction can be assumed to vanish at the wire boundary.

For an infinitely long wire with a circular cross-section of diameter d_w, we take the z axis to be parallel to the wire axis, with the x and y axes lying on the cross-sectional plane. The cylindrical symmetry properties of the wire are then used to simplify Eq. (3.2) by making $\alpha_{xy} = \alpha_{yx} = 0$, which can be achieved by a proper rotation about the z axis. The wavefunction then has the form:

$$\psi(\mathbf{r}) = u(x, y)\exp(i\xi x)\exp(i\eta y)\cdot\exp(ik_z z), \qquad (3.3)$$

where ξ and η are constants to be determined, and k_z is the wavenumber of the traveling wave in the z direction. By letting $\xi = -(\alpha_{xz}/\alpha_{xx})k_z$ and $\eta = -(\alpha_{yz}/\alpha_{yy})k_z$, Eq. (3.2) is reduced to a concise second-order differential equation in x and y only:

$$-\frac{\hbar^2}{2}\left(\alpha_{xx}\frac{\partial^2}{\partial x^2} + \alpha_{yy}\frac{\partial^2}{\partial y^2}\right)u = \left(E - \frac{\hbar^2 k_z^2}{2m_{zz}}\right)u, \qquad (3.4)$$

where

$$m_{zz} = \hat{z}\cdot\mathbf{m_e}\cdot\hat{z} \qquad (3.5)$$

is the transport effective mass along the wire axis. Equation (3.4) is reminiscent of a 2D Schrödinger equation with in-plane effective mass components

$$\begin{aligned} m_x &\equiv \alpha_{xx}^{-1} \\ m_y &\equiv \alpha_{yy}^{-1} \end{aligned} \qquad (3.6)$$

in the x and y directions, respectively. Since $u(x, y)$ must satisfy the boundary

condition: $u(x, y) = 0$ when $x^2 + y^2 = (d_w/2)^2$, the eigenvalues of $u(x, y)$ in Eq. (3.4) are quantized, and the energy of the electrons is written as

$$E_{nm}(k_z) = \varepsilon_{nm} + \frac{\hbar^2 k_z^2}{2m_{zz}}, \tag{3.7}$$

where ε_{nm} is the eigenvalue of Eq. (3.4) corresponding to the subband edge eigenstate at $k_z = 0$ labeled by the quantum numbers (n, m).

In the nanowire system, the quantized subband energy ε_{nm} and the transport effective mass m_{zz} along the wire axis are the two most fundamental parameters that determine essentially every electronic property of this 1D system. For a simple case where $\alpha_{xx} = \alpha_{yy}$, the wavefunction of Eq. (3.4) has the analytical solution,

$$u_{nm}(r) \sim J_n(\chi_{nm} r) e^{im\theta}, \tag{3.8}$$

where J_n is the nth Bessel function, and χ_{nm} is determined by the mth root of $J_n(x d_w/2) = 0$. The subband energy ε_{nm} corresponding to the wavefunction $u_{nm}(r)$ is given by

$$\varepsilon_{nm} = \frac{\hbar^2}{2} \alpha_{xx} \chi_{nm}^2. \tag{3.9}$$

For the general case where $\alpha_{xx} \neq \alpha_{yy}$, there are no analytical solutions and the only possible approach to determine the quantized subband energy ε_{nm} from Eq. (3.4) is through numerical methods, as described in Ref. [79].

The density of states (DOS) of electrons in nanowires is derived from Eq. (3.7) as

$$g(E) = \frac{\sqrt{2m_{zz}}}{\pi \hbar} \sum_{n,m} (E - \varepsilon_{nm})^{-1/2}, \tag{3.10}$$

which has a very different form from that of bulk materials. Figure 3-1 shows the calculated DOS for electrons in a 40-nm Bi nanowire compared to that of bulk Bi, in which the non-parabolic character of the electron pockets is also taken into account. The DOS in nanowires is a superposition of 1D transport channels, each located at a quantized subband edge ε_{nm}. We note that the DOS of nanowires has sharp peaks

46
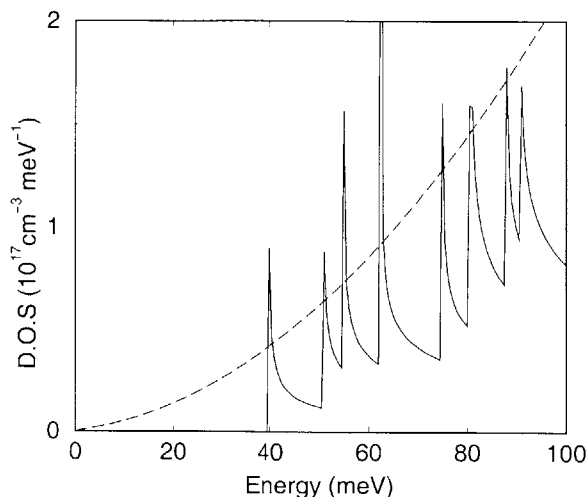
Figure 3-1: Calculated effective densities of states for 40-nm bismuth nanowires (—) and bulk bismuth (- - -). The zero energy refers to the band edge of bulk bismuth.

at the subband edges, whereas the DOS in a bulk material is a smooth monotonic function of energy. The enhanced density of states at the subband edges has important implications for many applications, such as in optics [14, 80] and thermoelectrics [6].

3.2.2   Band Structure of Nanowires in Magnetic Fields

With the application of a magnetic field, the trajectory of carriers is deflected due to the Lorentz force. In addition, in crystalline materials with high mobility carriers, the magnetic field yields discrete Landau levels and alters the electronic properties of the systems. Both effects will change the transport properties of the material. In this section, we will devote our attention to the effect of magnetic field on the energy spectrum of nanowire systems.

In a bulk material with isotropic carriers, magnetic field causes the energy levels associated with motion in the plane perpendicular to the magnetic field to collapse

into equally spaced Landau levels, which can be written as:

$$E_l = \hbar\omega_c(l + \frac{1}{2}),$$

(3.11)

where $\omega_c = eB/m$ is the cyclotron frequency, and l is a non-negative integer. The degeneracy factor of each Landau level is proportional to the magnetic field strength, and is given by eB/h. The total energy for a free electron in a magnetic field is then

$$E_l = \hbar\omega_c(l + \frac{1}{2}) + \frac{\hbar^2 k_z^2}{2m}.$$

(3.12)

However, in a nanowire, these Landau levels are no longer well-defined due to the competing interaction of quantum confinement, which also tends to form quantized levels. Therefore, the energy levels of nanowires in a magnetic field will depend on the wire diameter and the magnetic field, as well as the field direction relative to the wire axis. In addition, for materials with anisotropic carriers, such as Bi, the energy levels will also be affected significantly depending on the direction of the magnetic field relative to the major crystallographic axes. Since the transport properties of nanowires are closely related to these subband levels, it is necessary to obtain the shifts in energy levels in the presence of a magnetic field. A theoretical formulation is presented in this section for nanowires with anisotropic carriers in a magnetic field parallel to the wire axis.

Assuming that the nanowire axis and the magnetic field are both in the z direction, the Schrödinger equation for an anisotropic carrier in the magnetic field is:

$$\frac{1}{2}(\mathbf{P} - e\mathbf{A})\cdot\boldsymbol{\alpha}\cdot(\mathbf{P} - e\mathbf{A})\Psi(\mathbf{r}) = E\Psi(\mathbf{r}),$$

(3.13)

where $\mathbf{P} = -i\hbar\boldsymbol{\nabla}$ is the momentum operator, $\boldsymbol{\alpha}$ is a symmetric second-rank tensor denoting the inverse effective mass tensor, and $\mathbf{A}$ is the vector potential. The vector potential satisfies $\nabla \times \mathbf{A} = \mathbf{B}$ where $\mathbf{B}$ is the magnetic field. For a magnetic field

48

along the z axis, we choose the symmetric gauge for $\mathbf{A}$:

$$\mathbf{A} = \frac{B}{2}(x, -y, 0). \tag{3.14}$$

As shown earlier, in a wire with cylindrical symmetry, the inverse effective mass tensor $\boldsymbol{\alpha}$ can be written, without loss of generality, as

$$\boldsymbol{\alpha} \equiv \mathbf{M}^{-1} = \begin{pmatrix} \alpha_{11} & 0 & \alpha_{13} \\ 0 & \alpha_{22} & \alpha_{23} \\ \alpha_{31} & \alpha_{32} & \alpha_{33} \end{pmatrix} \tag{3.15}$$

where $\alpha_{ij} = \alpha_{ji}$. Assuming that the solution of $\Psi(\mathbf{r})$ in Eq. (3.13) has the same form as Eq. (3.3) and substituting the assumed wavefunction into Eq. (3.13), it is surprising that the resulting equation can also be significantly reduced into a manageable form by letting $\xi = -\alpha_{13}/\alpha_{11}k_z$ and $\eta = -\alpha_{23}/\alpha_{11}k_z$, as we did in the previous section. The resulting wave equation then becomes:

$$-\frac{\hbar^2}{2}\left(\alpha_{11}\frac{\partial^2}{\partial x^2} + \alpha_{22}\frac{\partial^2}{\partial y^2}\right)u \;+\; i\hbar^2(\frac{eB}{2})\left(\alpha_{11}y\frac{\partial}{\partial x} - \alpha_{22}x\frac{\partial}{\partial y}\right)u \tag{3.16}$$

$$+\; \frac{\hbar^2}{2}(\frac{eB}{2})^2(\alpha_{11}y^2 + \alpha_{22}x^2)u = \left(E - \frac{\hbar^2 k_z^2}{2m_{33}}\right)u$$

where $m_{33} = \hat{z} \cdot \mathbf{M} \cdot \hat{z}$ is the transport effective mass along the wire axis. The eigenvalues of Eq. (3.16) can then be derived through numerical solutions with proper boundary conditions. We note that due to the finite cross-sectional area, the well-defined degenerate Landau levels are lifted into discrete subbands. Also, the transport effective mass m_{33} is unchanged in the presence of longitudinal magnetic field, and the result given in Eq. (3.5) still applies, indicating that the motion along the wire axis is not affected by the longitudinal magnetic field. Eq. (3.16) can be written in a more concise form as:

$$\frac{1}{2}(\mathbf{P}_{2D} - e\mathbf{A}_{2D}) \cdot \boldsymbol{\alpha}_{2D} \cdot (\mathbf{P}_{2D} - e\mathbf{A}_{2D})u(x,y) = \left(E - \frac{\hbar^2 k_z^2}{2m_{33}}\right)u(x,y) \tag{3.17}$$

49

where $\mathbf{P}_{2D}$ and $\mathbf{A}_{2D}$ are the projection of the momentum operator $\mathbf{P}$ and the vector potential $\mathbf{A}$ on the x-y plane, respectively, and $\boldsymbol{\alpha}$ is the 2D projection of the inverse effective mass tensor given by:

$$\boldsymbol{\alpha}_{2D} = \begin{pmatrix} \alpha_{11} & 0 \\ 0 & \alpha_{22} \end{pmatrix}. \tag{3.18}$$

It is interesting to note the resemblance between Eq. (3.13) and Eq. (3.17), which holds even for anisotropic carrier pockets. The importance of Eq. (3.17) cannot be over-emphasized since it provides the insight into the electronic structure of a nanowire in a magnetic field. It should also be noted that the validity of Eq. (3.17) is not self-evident for an anisotropic carrier pocket, since special conditions for ξ and η have to be met with respect to the original wavefunction $\Psi(\mathbf{r})$ (see Eq. (3.3)).

3.2.3 Transport Equations

The transport properties of nanowire systems have been studied by extending the semi-classical Boltzmann transport model to 1D systems. For a one-band system in a 1D quantum wire, important thermoelectric-related transport coefficients such as the electrical conductivity σ, the Seebeck coefficient S, and the thermal conductivity λ_e are derived as [81, 82]:

$$\sigma = \mathcal{L}^{(0)} \tag{3.19}$$

$$S = -\frac{1}{eT}\frac{\mathcal{L}^{(1)}}{\mathcal{L}^{(0)}} \tag{3.20}$$

$$\lambda_e = \frac{1}{e^2 T}(\mathcal{L}^{(2)} - \frac{(\mathcal{L}^{(1)})^2}{\mathcal{L}^{(0)}}), \tag{3.21}$$

where T is the temperature and

$$\mathcal{L}^{(\alpha)} = e^2 \int \frac{4dk}{\pi^2 d^2} \left(-\frac{df}{dE}\right) \tau(k)v(k)v(k)(E(k) - E_F)^\alpha, \tag{3.22}$$

in which $\alpha = 0, 1$ or 2, $E(k)$ is the carrier dispersion relation, $\tau(k)$ is the relaxation time, E_F is the Fermi energy, and $f(E)$ is the Fermi-Dirac distribution function. For a one-band system with a parabolic dispersion relation, the transport elements $\mathcal{L}^{(\alpha)}$ in Eqs. (3.19)–(3.21) are derived as

$$\mathcal{L}^{(0)} = D \left[\frac{1}{2} F_{-\frac{1}{2}} \right] \tag{3.23}$$

$$\mathcal{L}^{(1)} = \begin{cases} (k_B T) D \left[\frac{3}{2} F_{\frac{1}{2}} - \frac{1}{2} \zeta^* F_{-\frac{1}{2}} \right] & \text{(for electrons)} \\ -(k_B T) D \left[\frac{3}{2} F_{\frac{1}{2}} - \frac{1}{2} \zeta^* F_{-\frac{1}{2}} \right] & \text{(for holes)} \end{cases} \tag{3.24}$$

$$\mathcal{L}^{(2)} = (k_B T)^2 D \left[\frac{5}{2} F_{\frac{3}{2}} - 3 \zeta^* F_{\frac{1}{2}} + \frac{1}{2} \zeta^{*2} F_{-\frac{1}{2}} \right] \tag{3.25}$$

where D is given by

$$D = \frac{8e}{\pi^2 d_w^2} \left(\frac{2m^* k_B T}{\hbar^2} \right)^{\frac{1}{2}} \mu, \tag{3.26}$$

in which μ is the carrier mobility along the nanowire and

$$F_j = \int_0^\infty \frac{x^j dx}{e^{(x - \zeta^*)} + 1} \tag{3.27}$$

denotes the Fermi-Dirac related functions, with fractional indices $j = -\frac{1}{2}, \frac{1}{2}, \frac{3}{2}, \ldots$. The reduced chemical potential ζ^* is defined as

$$\zeta^* = \begin{cases} (E_F - \varepsilon_e^{(0)})/k_B T & \text{(for electrons)} \\ (\varepsilon_h^{(0)} - E_F)/k_B T & \text{(for holes)} \end{cases}, \tag{3.28}$$

where $\varepsilon_e^{(0)}$ and $\varepsilon_h^{(0)}$ denote the 1D subband edges for electrons and holes, respectively.

For the Bi and $\mathrm{Bi}_{1-x}\mathrm{Sb}_x$ quantum wire systems, there are many 1D subbands due to the multiple carrier pockets, and the quantum confinement-induced band splitting also forms a set of 1D subbands from each single band in the bulk material. Therefore, when considering the transport properties of real 1D nanowire systems, contributions from all of the subbands near the Fermi energy should be included, and the $\mathcal{L}^{(\alpha)}$'s in Eqs. (3.19)–(3.21) should be replaced by the sum $(\mathcal{L}_{total}^{(\alpha)} = \sum_i \mathcal{L}_i^{(\alpha)})$ of contributions from each subband i to obtain the various transport coefficients.

Another physical quantity of interest in the thermoelectric application of quantum wire systems is the lattice thermal conductivity λ_L which, together with the electronic thermal conductivity λ_e, determines the total thermal conductivity of the system. The lattice thermal conductivity in 1D systems has been studied by using the Boltzmann equation for phonons and considering the diffusive and specular phonon scattering at the wire boundary [83,84]. The calculated results showed that λ_L decreases significantly below the bulk value for small wire diameters. In this study, we use a simpler approach to estimate λ_L for nanowire systems as follows. From the kinetic theory, the thermal conductivity of phonons is given by [85]

$$\lambda_L = \frac{1}{3} C_v v \Lambda, \tag{3.29}$$

where C_v is the heat capacity per unit volume, v is the sound velocity, and Λ is the mean free path for phonons. We note that the wide bandgap host material which confines electrons cannot confine the phonon paths, and thus, because of acoustic mismatch, phonons will be scattered when they move across the wire boundary. Therefore, if the phonon mean free path Λ_B in the bulk material is larger than the wire diameter d_w, then Λ and λ_L are mainly limited by the predominant phonon scattering at the wire boundary, and the lattice thermal conductivity of the quantum wire system is obtained approximately [5,6] by setting $\Lambda = d_w$ and using Eq. (3.29). On the other hand, the bulk value of λ_L is used for a conservative estimation of the thermal conductivity of nanowire systems if d_w is larger than Λ_B.

3.3 Electronic Properties of Bulk Bi and $\mathrm{Bi}_{1-x}\mathrm{Sb}_x$ Alloys

Bi is a group V semimetal, in which the electrons are distributed in three highly anisotropic ellipsoidal carrier pockets at the L points of the Brillouin zone, and an equal number of holes are contained in one pocket at the T point (see Fig. 3-2).
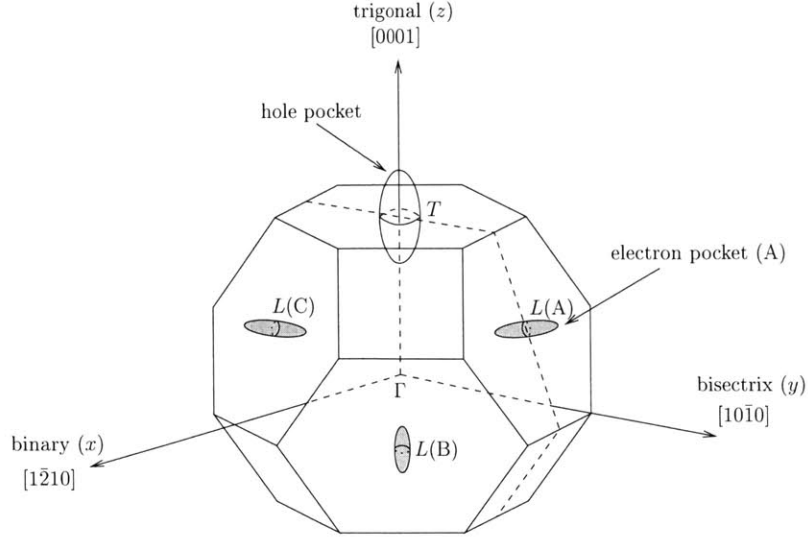
Figure 3-2: The Brillouin zone of Bi, showing the Fermi surfaces of the T-point hole pocket and the three L-point electron pockets.

The effective mass of the T-point holes is heavier than the L-point carriers, and the dispersion relation at the T point can be approximated by a parabola. The L-point carriers, however, are highly non-parabolic due to the strong coupling between the L-point valence and conduction bands, which gives rise to the very small effective mass components for L-point carriers along certain crystallographic directions. The valence band and the conduction band at the L points are symmetric, and their dispersion relations are described by

$$E_L(\mathbf{k}) = -\frac{E_{gL}}{2}\left(1 \pm \sqrt{1 + \frac{2\hbar^2}{E_{gL}}\mathbf{k}\cdot\boldsymbol{\alpha_e}\cdot\mathbf{k}}\right) \qquad (3.30)$$

for the L-point electrons ($-$ sign) and holes ($+$ sign), where E_{gL} (38 meV at 77 K) is the direct L-point band gap, and $\boldsymbol{\alpha_e}$ is the inverse mass tensor at the conduction (or valence) band extremum. Although either the L-point electrons or the T-point holes alone would make large Seebeck coefficient contributions, pure bulk Bi has a small Seebeck coefficient because the contributions from electrons and holes nearly cancel each other. Thus, bulk Bi has been traditionally considered a poor thermoelectric material. However, it has also been suggested that if the overlap between the T-point valence band and the L-point conduction band can be reduced, it may be possible to

Table 3.1: The band structure parameters of bulk Bi at $T \leq 77\,\mathrm{K}$ [86].

Parameters	Notation	Value	Reference
Band overlap[a]	Δ_0	$-38\,\mathrm{meV}$	[76]
Band gap at the L point	E_{gL}	$13.8\,\mathrm{meV}$	[87]
Electron effective mass tensor elements at the band edge for the $L(A)$ pocket[b]	m_{e1}	$0.00119\,m_0$	[75]
	m_{e2}	$0.263\,m_0$	
	m_{e3}	$0.00516\,m_0$	
	m_{e4}	$0.0274\,m_0$	
T-point hole effective mass tensor elements at the band edge	m_{h1}	$0.059\,m_0$	[76]
	m_{h2}	$0.059\,m_0$	
	m_{h3}	$0.634\,m_0$	
Electron mobility[c] at $77\,\mathrm{K}$ $(10^4\,\mathrm{cm}^2/\mathrm{Vs})$	μ_1	68.0	[88]
	μ_2	1.6	
	μ_3	38.0	
	μ_4	-4.3	
Hole mobility[c] at $77\,\mathrm{K}$ $(10^4\,\mathrm{cm}^2/\mathrm{Vs})$	$\mu_{h1} = \mu_{h2}$	12.0	[88]
	μ_{h3}	2.1	

[a]The band overlap for Sb and As is 177.5 meV and 356 meV, respectively.
[b]The tilt angle of the L-point electron ellipsoids are $6.0°$, $-4°$, and $-4°$ for Bi, Sb, and As, respectively. The tilt angle of the H-point hole "ellipsoids" are $53°$ for Sb and $37.5°$ for the major As hole ellipsoid.
[c]The forms of the effective mass tensor and the mobility tensor are assumed to be the same for a given carrier pocket for Bi. Since the Fermi surfaces of the carrier pockets for Sb and As are much larger than for Bi, the ellipsoidal approximation is not valid and more accurate models are necessary to obtain quantitative results.

develop a good thermoelectric material based on Bi. Values for the band parameters of bulk Bi are given in Table 3.1. Since these band parameters are highly sensitive to temperature, their temperature dependences are listed in Table 3.2.

Bismuth can be alloyed isoelectronically with antimony (Sb) to yield a high mobility material with desirable thermoelectric properties. Bi and Sb both crystallize in the same A_7 structure with space group $R\bar{3}m$ [92], and $\mathrm{Bi}_{1-x}\mathrm{Sb}_x$ alloys form a solid solution over the entire compositional range x. The lattice constants and structural parameters obey Vegard's law for $x \leq 0.3$ [93], which is the range of interest for low-dimensional thermoelectricity. In antimony, the electron pockets are at the L points of the Brillouin zone, while holes are at the H points (see Fig. 3-3). The substitution

Table 3.2: Temperature dependence of selected bulk Bi band structure parameters.

Parameters	Temperature Dependence	
Band overlap (meV) [89]	$\Delta_0 = \begin{cases} -38 \ (\text{meV}) & (T < 80\text{K}) \\ \\ -38 - 0.044(T-80) \\ +4.58 \times 10^{-4}(T-80)^2 & (T > 80\text{K}) \\ -7.39 \times 10^{-6}(T-80)^3 \end{cases}$	(3.31)
Direct band gap (meV) [90]	$E_{gL} = 13.6 + 2.1 \times 10^{-3}T + 2.5 \times 10^{-4}T^2$	(3.32)
L-point electron effective mass components [75, 90]	$[\mathbf{m}_e(T)]_{ij} = \dfrac{[\mathbf{m}_e(0)]_{ij}}{1 - 2.94 \times 10^{-3}T + 5.56 \times 10^{-7}T^2}$	(3.33)
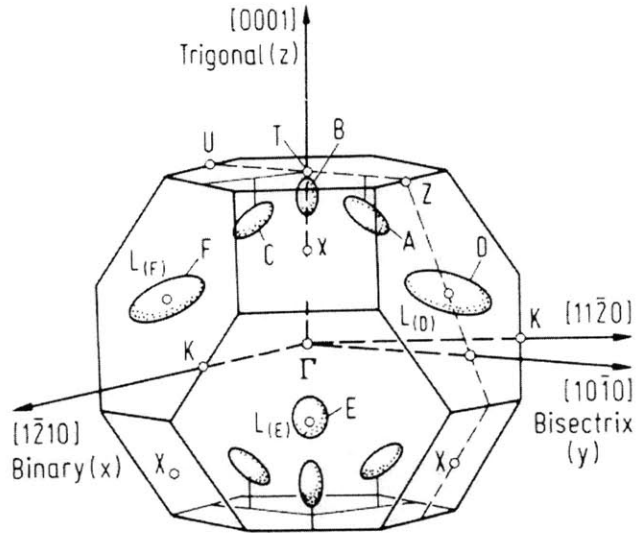
Figure 3-3: The three L-point electron carrier pockets and the six H-point hole carrier pockets of Sb in the rhombohedral Brillouin zone [91]. As a first approximation, ellipsoidal carrier pockets are assumed.
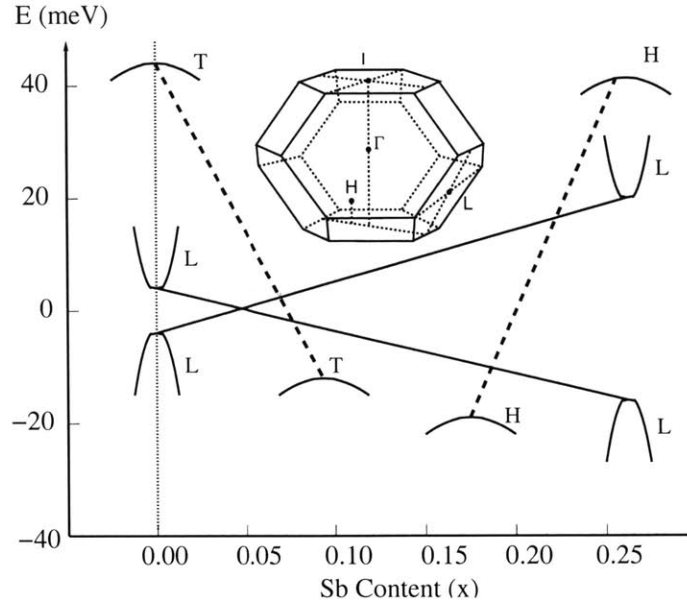
Figure 3-4: Schematic diagram for the energy bands near the Fermi level for 3D $Bi_{1-x}Sb_x$ alloys as a function of x at low T ($\leq 77\,K$) [77].

of Sb atoms in the Bi lattice has a major effect on the electronic band structure of Bi (see Fig. 3-4). Three features of particular interest include: (1) the crossing of the L_S and L_A energy bands at $x \sim 0.05$; (2) the semiconducting range ($0.07 < x < 0.22$) delineated by the crossing of the L-point conduction band with the T-point hole band at $x = 0.07$ and with the H-point hole band at $x = 0.22$; and (3) the range of $0.09 < x < 0.16$ where the highest lying valence band is at the L point, giving rise to the possibility of p-type carriers (which are mirror images of the L-point electron carriers) with excellent thermoelectric properties.

56

(a) Semimetal   (b) Transition   (c) Semiconductor

Conduction Band

Valence Band

Decreasing Wire Diameter
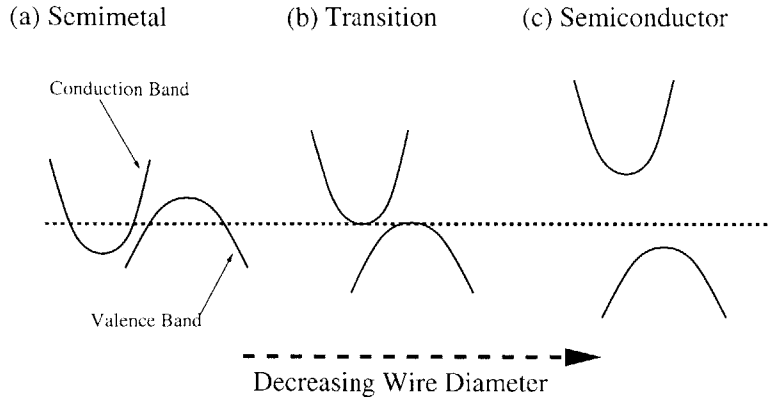
Figure 3-5: Schematic illustrating the semimetal-semiconductor transition in nanowires made of semimetals: (a) bulk semimetals with a band overlap between the electrons and holes, (b) nanowires with a critical wire diameter d_c undergoing the semimetal-semiconductor transition, and (c) nanowires with diameters smaller than d_c, exhibiting a bandgap between the conduction and valence bands.

3.4 Predictions for $Bi_{1-x}Sb_x$ Nanowires

3.4.1 Band Structure Engineering and Semimetal-Semiconductor Transition

For semimetals, such as Bi, the conduction band overlaps with the valence band, and the electronic properties are governed by both electrons and holes. Quantum confinement effects in nanowires cause the band edge of the electrons to move up in energy, while decreasing the energy of the valence band edge. The band edge energies of electrons and holes shift in opposite directions in Bi, decreasing the energy overlap between the conduction and valence bands, as illustrated in Fig. 3-5. As the wire diameter decreases further, the energy overlap vanishes eventually (Fig. 3-5(b)), and a band gap is formed between the lowest conduction subband and the highest valence subband, causing a semimetal-to-semiconductor transition. The critical wire diameter d_c corresponding to this transition depends on the band overlap energy, electron and hole effective masses, and the crystal orientation along the wire axis. For Bi nanowires, d_c is is predicted to be $\sim 50\,\mathrm{nm}$ at $77\,\mathrm{K}$ [79]. Owing to the large carrier anisotropy
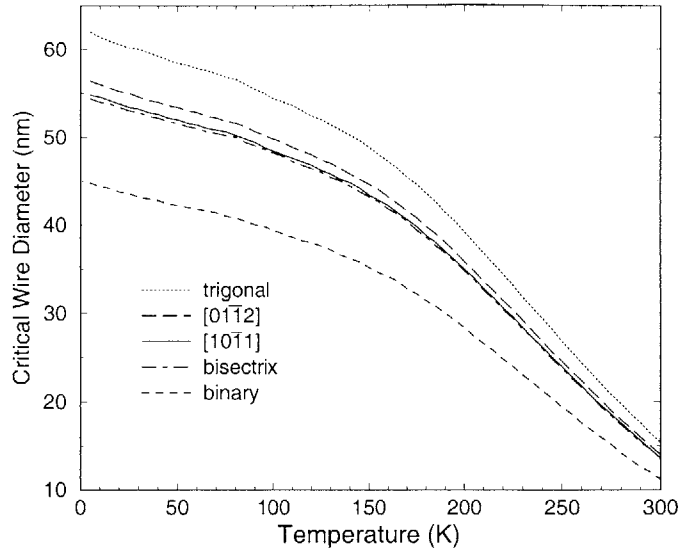
Figure 3-6: Calculated critical wire diameter d_c for the semimetal-semiconductor transition as a function of temperature for Bi nanowires oriented in different directions [79].

Table 3.3: Calculated critical wire diameter d_c for the semimetal-semiconductor transition of Bi nanowires of various crystallographic orientations at 77 K and 300 K [79].

Temperature	Trigonal	Binary	Bisectrix	[01$\bar{1}$2]	[10$\bar{1}$1]
77 K	55.1 nm	39.8 nm	48.5 nm	49.0 nm	48.7 nm
300 K	15.4 nm	11.2 nm	13.6 nm	14.0 nm	13.6 nm

and highly temperature-dependent band structure parameters of Bi, this critical wire diameter is a function of wire orientation and temperature, as shown in Fig. 3-6 and Table 3.3 [79]. The quantum confinement-induced semimetal-semiconductor transition dramatically alters the electronic properties of the nanowires, and could be used to design a system of desired band structure.

In addition to quantum confinement effects, the electronic properties of Bi nanowires can be further engineered by Sb alloying. Figure 3-7 illustrates the electronic phase diagram of $Bi_{1-x}Sb_x$ nanowires as a function of wire diameter and Sb content x [94]. The semimetal and indirect semiconductor states at $x \lesssim 0.13$ have the highest valence band extremum at the T-point, while those states at $x \gtrsim 0.13$ have
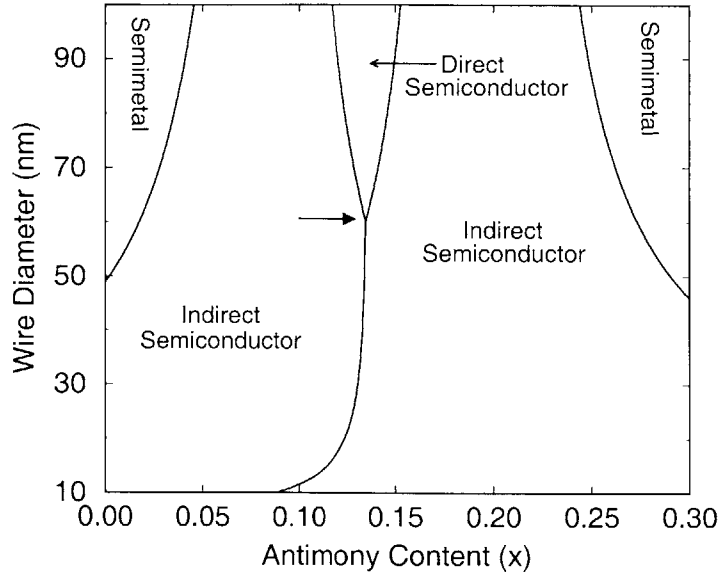
Figure 3-7: The electronic phase diagram of $Bi_{1-x}Sb_x$ nanowires as a function of wire diameter and antimony content x at 77 K [94].

their H-point hole pockets at the highest energy. Along the solid lines in this "phase diagram", the extrema of the first subband of carrier pockets coalesce in energy at two different points in the Brillouin zone. This diagram predicts a shift in d_c to higher values as Sb is added to pure Bi. In Fig. 3-7, another semimetal-semiconductor transition involving the band overlap between the H-point holes and the L-point electrons is also noticed for $Bi_{1-x}Sb_x$ nanowires at $x \geq 0.24$, where d_c shifts to lower values as the Sb content increases. The bold arrow in the center of the diagram points to the particularly interesting situation where the extrema of all 10 hole pockets coalesce in energy ($d_w = 60$ nm, $x = 0.13$), resulting in a high density of states that may be beneficial towards increasing the thermopower.

3.4.2   Thermoelectric Properties

The efficiency of a thermoelectric material is measured by the figure of merit,

$$Z = \frac{S^2 \sigma}{\lambda},$$ (3.34)
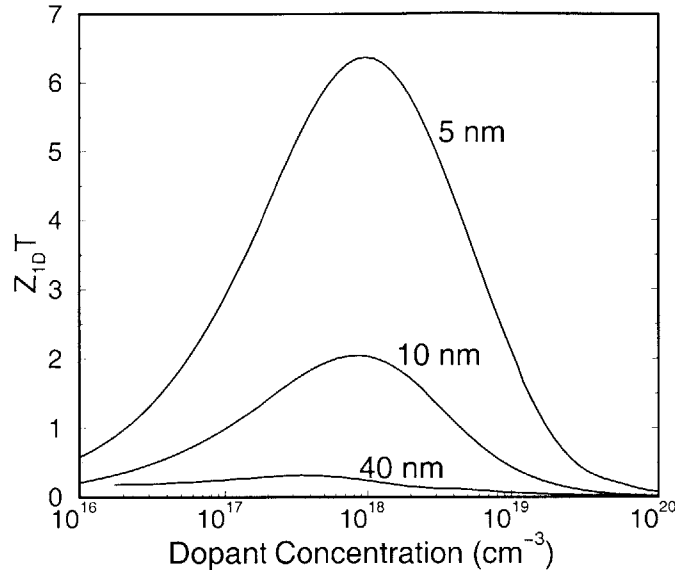
Figure 3-8: Calculated $Z_{1D}T$ at 77 K as a function of carrier concentration for n-type Bi nanowires of different diameters oriented along the trigonal axis [79].

where S is the Seebeck coefficient, σ is the electrical conductivity, and λ is the thermal conductivity. The thermal conductivity consists of two components: lattice thermal conductivity λ_L and electronic thermal conductivity λ_e, and $\lambda = \lambda_L + \lambda_e$.

The thermoelectric figure of merit $Z_{1D}T$ of $Bi_{1-x}Sb_x$ nanowires is calculated based on the theoretical model developed in previous sections and in Ref. [79], taking into consideration the multiple carrier pockets and the non-parabolic behavior of L-point carriers. Figure 3-8 shows the calculated $Z_{1D}T$ for n-type Bi nanowires oriented along the trigonal axis at 77 K as a function of dopant concentration for three different wire diameters [79]. We note that the value of $Z_{1D}T$ for a given donor concentration increases dramatically with decreasing wire diameter d_w. For 5-nm Bi nanowires oriented along the trigonal axis, the maximum $Z_{1D}T$ at 77 K is $\sim$ 6.4, with an optimized electron concentration $N_{d(opt)} \simeq 10^{18}\,\mathrm{cm}^{-3}$. The value of $Z_{1D}T$ also strongly depends on the wire orientation due to the anisotropic nature of the Bi band structure and thermal properties. Figure 3-9 shows the calculated figure of merit $Z_{1D}T$ at 77 K as a function of donor concentration N_d for 10-nm Bi nanowires oriented in different directions. The trigonal nanowires have the highest optimal $Z_{1D}T$ ($\sim$ 2.1), while
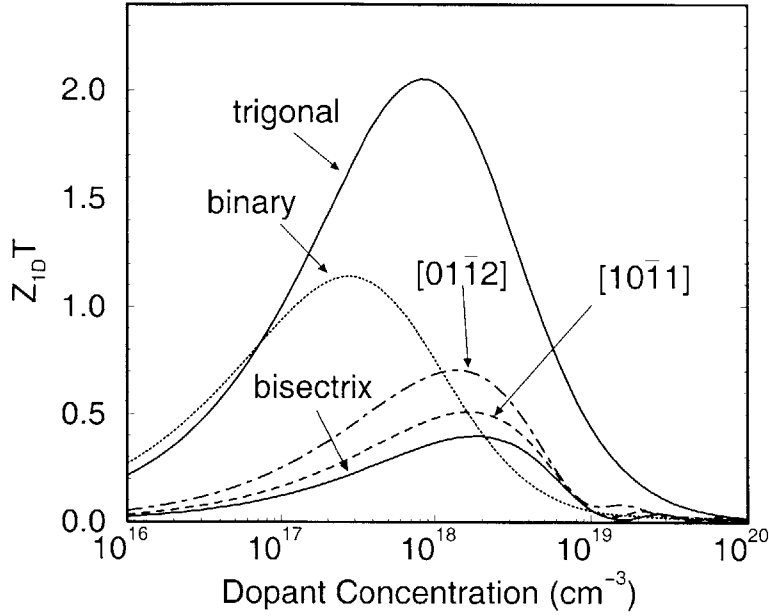
Figure 3-9: Calculated $Z_{1D}T$ at 77 K as a function of carrier concentration N_d for 10-nm n-type Bi nanowires oriented along trigonal, binary, bisectrix, [10$\bar{1}$1] and [01$\bar{1}$2] directions [79].

the bisectrix wires have the lowest optimal $Z_{1D}T$ of ~ 0.4. A detailed discussion on the optimal $Z_{1D}T$ of Bi nanowires with different diameters and crystal orientations has been presented in Ref. [79]. The optimum carrier concentrations $N_{d(opt)}$ and the corresponding $Z_{1D}T$ of nanowires at 77 K are summarized in Table 3.4.

Figures 3-10(a) and (b) depict the contour plots of the optimal $Z_{1D}T$ for n- and p-type Bi$_{1-x}$Sb$_x$ nanowires at 77 K [94], respectively, showing improved thermoelectric efficiency compared to pure Bi nanowire systems. For n-type Bi$_{1-x}$Sb$_x$ nanowires, $Z_{1D}T$ increases as the wire diameter decreases at all x values. For p-type Bi$_{1-x}$Sb$_x$ nanowires, however, the contour plot of $Z_{1D}T$ (see Fig. 3-10(b)) is very different from that of the n-type counterparts, with a local maximum $Z_{1D}T$ of ≥ 1.2 observed at $0.13 \leq x \leq 0.14$ and 35 nm $\leq d_w \leq$ 43 nm at 77 K. This unusual enhancement in $Z_{1D}T$ for p-type Bi$_{1-x}$Sb$_x$ nanowires, which is absent in n-type nanowires, is due to the merging of 10 valence subbands to a common degeneracy point noted in Fig. 3-7. It is this degeneracy that leads to an increased density of states near the Fermi energy for valence band carriers in p-type Bi$_{1-x}$Sb$_x$ nanowires, which is in turn manifested in the high $Z_{1D}T$ values calculated. Since there is no corresponding degeneracy for

Table 3.4: The optimum dopant concentrations $N_{d(\text{opt})}$ (in $10^{18}\,\text{cm}^{-3}$) and the corresponding $Z_{1D}T$ for n-type and p-type Bi nanowires of various diameters and orientations at 77 K [79].

Wire Orientation		5 nm		10 nm		40 nm	
		$N_{d(\text{opt})}$	$Z_{1D}T$	$N_{d(\text{opt})}$	$Z_{1D}T$	$N_{d(\text{opt})}$	$Z_{1D}T$
Trigonal	n-type	0.96	6.36	0.81	2.0	0.38	0.31
	p-type	0.96	6.36	12.9	0.72	6.2	0.17
Binary	n-type	0.35	3.68	0.28	1.14	0.56	0.13
	p-type	0.79	1.78	10.3	0.16	7.9	0.05
Bisectrix	n-type	4.1	2.21	1.78	0.40	4.97	0.03
	p-type	0.74	0.32	0.19	0.40	0.50	0.07
[10$\bar{1}$1]	n-type	3.21	2.69	1.57	0.51	2.57	0.04
	p-type	1.04	1.16	0.43	0.19	0.63	0.05
[01$\bar{1}$2]	n-type	2.07	3.41	1.33	0.70	2.73	0.06
	p-type	2.59	2.46	0.58	0.18	0.75	0.03
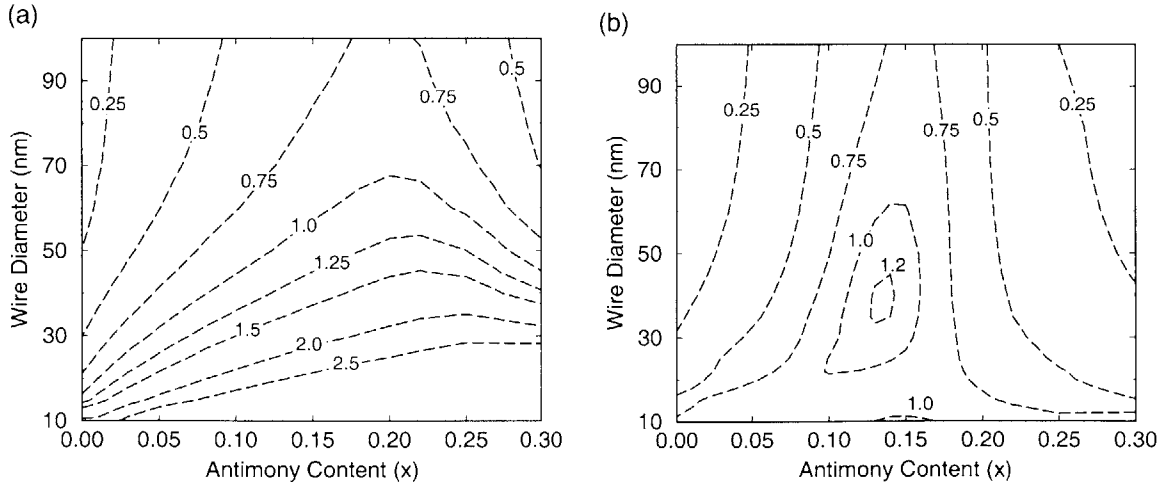
Figure 3-10: Contour plots of optimal ZT values for (a) n-type and (b) p-type $Bi_{1-x}Sb_x$ nanowires of different wire diameters and antimony contents at 77 K [94].

the conduction bands, the thermoelectric performance for n-type nanowires exhibits a monotonic variation as a function of wire diameter. Fig. 3-10 indicates that with the addition of Sb in accordance with the band structure engineering concept [79, 94, 95], $Z_{1D}T > 1$ can be achieved at 77 K for Bi-based nanowires with a diameter as large as 40 nm, which can be achieved readily with existing fabrication techniques.

Chapter 4

Transport Properties of Bi$_{1-x}$Sb$_x$ Nanowires

4.1 Introduction

Factors that determine the transport properties of nanowires include wire diameter (which is important for both classical and quantum size effects), material composition, surface chemistry, and crystallinity. Also, crystallographic orientation along the wire axis is critical for materials with anisotropic electronic parameters, such as effective mass tensor, Fermi surface, and carrier mobility.

The electronic transport behavior of nanowires may be categorized based on the relative magnitude of three important length scales: carrier mean free path ℓ_W, the de Broglie wavelength of electrons λ_E, and wire diameter d_w. For wire diameters much larger than the carrier mean free path ($d_w \gg \ell_W$), the wires exhibit diameter-independent transport properties similar to bulk materials, since the scattering due to wire boundary is negligible compared to other scattering mechanisms. For wire diameters comparable to or smaller than the carrier mean free path ($d_w \lesssim \ell_W$), but much larger than the de Broglie wavelength of electrons ($d_w \gg \lambda_E$), the transport in nanowires is in the classical finite size regime, where the band structure of the nanowires is still similar to that of bulk materials, while their transport properties may become diameter-dependent because of the scattering events at the wire boundary.

For wire diameters comparable to the electronic wavelength $(d_w \sim \lambda_F)$, quantum subbands are formed due to quantum confinement at the wire boundary, and the electronic density of states is altered dramatically. In this regime, the transport properties are further influenced by the change in the band structure. We note that transport properties for nanowires in the classical finite size and quantum size regimes are expected to be highly diameter-dependent.

Bi and $Bi_{1-x}Sb_x$ alloys are promising candidates for studying the quantum size effects in the transport properties of nanowires because of their very small electron effective mass components and the long carrier mean free paths. Quantum size effects are expected to become significant in bismuth nanowires with diameters smaller than 50 nm [79], and the fabrication of crystalline nanowires of this diameter range has been demonstrated and discussed in Chapter 2.

In this chapter, we present transport measurements of $Bi_{1-x}Sb_x$ nanowires as a function of temperature, wire diameter, Sb content, and magnetic field. The experimental results are compared with theoretical predictions based on the model developed in Chapter 3. These transport measurements not only provide valuable information to validate theoretical assumptions and model calculations, but also demonstrate the enhanced thermoelectric performance of $Bi_{1-x}Sb_x$ nanowires. The theoretical model was further extended to other nanowires, such as Te-doped Bi nanowires and Sb nanowires, so as to study their transport behavior and to interpret the experimental results.

4.2 Temperature-Dependent Resistance Measurements

Measurements of the temperature-dependent resistance $R(T)$ of Bi-related nanowire arrays have been carried out on samples prepared by pressure injection [2] and vapor-phase deposition [96], yielding results that are consistent. Due to geometric
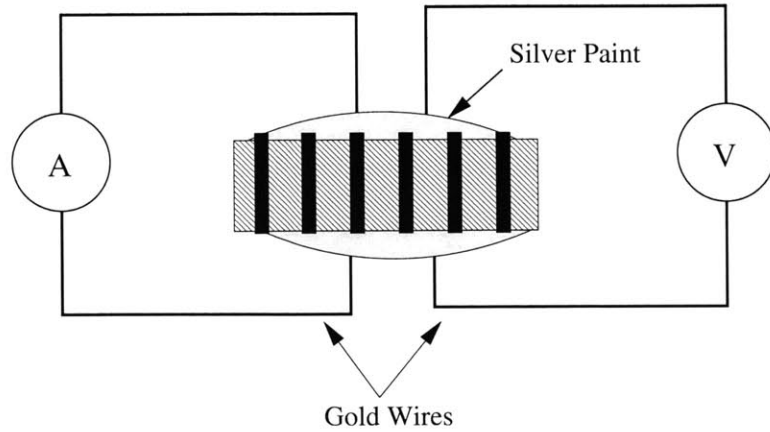
Figure 4-1: Schematic of the experimental set-up for two-probe measurements. Silver paint (Ladd Research Industries) is applied onto both sides of the template to make ohmic contacts, to which two gold wires are attached on each side. One pair of gold wires is connected to a current source, and the voltage drop is measured across the other pair of gold wires. The current is applied both forward and backward to eliminate any thermoelectric effects.

limitations, the first attempt to study the temperature-dependent properties of nanowires was made with a two-probe measurement (see Fig. 4-1). Recently, a number of high-resolution lithographic techniques have been developed for patterning nano-contacts to enable four-probe measurements on a single nanowire [97]. However, surface oxidation of the free-standing Bi-related nanowires upon their removal from the alumina matrix was found to prevent the fabrication of low-resistance ohmic contacts, rendering the temperature-dependent measurement a difficult task as these contacts become unstable at temperatures below 200 K [97]. On the other hand, the anodic alumina template protects the Bi-related nanowires against oxidation, and offers a convenient system for handling the nanowires. Hence, we adopt the two-probe method illustrated in Fig. 4-1 to study the temperature-dependent transport properties of nanowires arrays. Although an absolute value of the resistivity cannot be obtained by the two-probe method, the temperature dependence can be examined by normalizing the resistance $R(T)$ to the resistance at a common temperature, e.g. $R(300\,\text{K})$. In addition, since the nanowires formed in the anodic alumina template possess a very narrow diameter distribution ($\leq 10\%$ variation), the two-probe measurement on nanowire arrays may be utilized to reveal the size dependence

66

of their transport properties.

4.2.1 T-Dependent Resistance of Bi Nanowires

Figure 4-2 shows the temperature dependence of the resistivity $R(T)/R(300\,\text{K})$ of Bi nanowire arrays synthesized by vapor deposition [22]. As shown in Fig. 4-2, $R(T)$ of Bi nanowires is very different from that of bulk Bi, and is highly sensitive to the wire diameter. Interestingly, the $R(T)$ curves in Fig. 4-2 show a non-monotonic trend for nanowires of larger diameters (70 nm and 200 nm), whereas $R(T)$ curves decrease monotonically with T for nanowires with diameters of $\leq$ 48 nm. This dramatic change in $R(T)$ behavior as a function of d_w is attributed to the unique semimetal-semiconductor transition in Bi [98], induced by quantum size effects. The critical Bi wire diameter for the semimetal-semiconductor transition is predicted to be $\sim 50\,\text{nm}$ below 100 K, as discussed in Section 3.4.1. For $T > 70\,\text{K}$, the resistance of all nanowire arrays shown in Fig. 4-2 decreases with increasing T. For $T < 70\,\text{K}$, the resistance of the smaller Bi nanowires (7–48 nm) in the semiconducting regime increases with decreasing T, while the resistance decreases with decreasing T for the nanowires of larger diameters (70 and 200 nm) in the semimetallic regime. It is also noted that the temperature dependence of the resistance of semiconducting nanowires weakens as the wire diameter d_w decreases, as explained in the next section. The resistance of Bi nanowires is determined by two competing factors: the carrier density that increases with T, and the carrier mobility that decreases with T. Qualitatively, the non-monotonic $R(T)$ for Bi nanowires of larger diameters is due to a smaller carrier concentration variation in semimetals at low temperatures ($\leq$ 100 K), so that the electrical resistance is dominated by the carrier mobility in this temperature range.

Based on the band structure model and transport equations established for nanowires, the normalized temperature-dependent resistance $R(T)/R(270\,\text{K})$ for 70-nm and 36-nm Bi nanowires has been calculated [99], and the results are shown by the solid curves in Fig. 4-3, which exhibit trends consistent with the experimental results in Fig. 4-2. Calculations for nanowires of 70 nm and 36 nm diameters are particu-
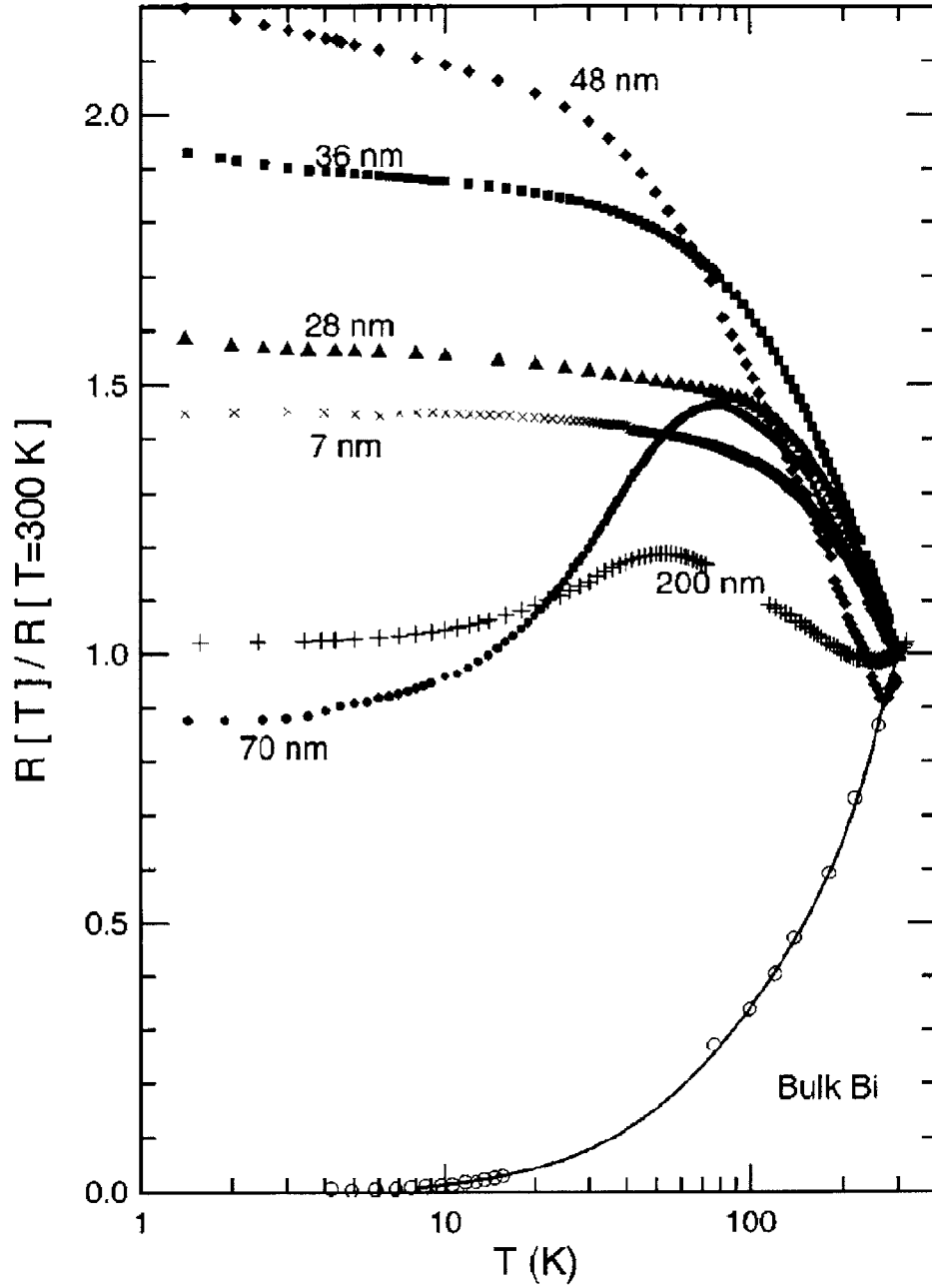
Figure 4-2: Temperature dependence of the normalized resistance $R(T)/R(300\,\mathrm{K})$ for Bi nanowire arrays of various wire diameters prepared by the vapor deposition method [22], in comparison with the corresponding data for bulk Bi.
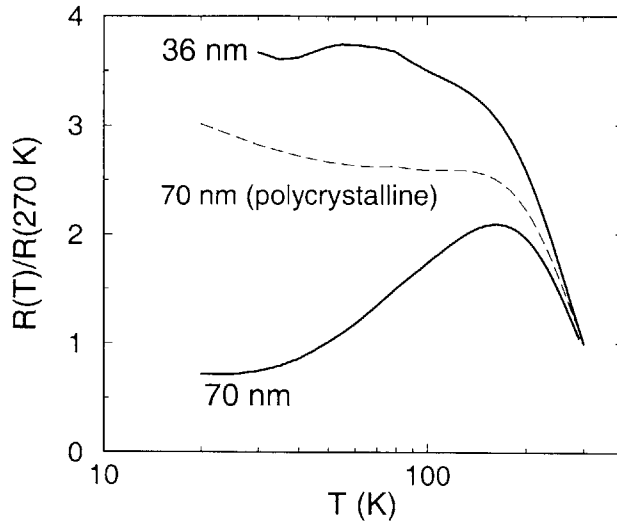
Figure 4-3: Calculated temperature dependence of $R(T)/R(270\,\mathrm{K})$ for Bi nanowires of 36 nm and 70 nm, using a semiclassical transport model [99].

larly interesting because they are semimetallic and semiconducting, respectively. In this model, additional scattering processes are considered for realistic Bi nanowires, including wire boundary and grain boundary scattering, and ionized impurity scattering that reflects the presence of uncontrolled charged impurities. The total mobility μ_{tot} by various scattering processes is taken into account by Matthiessen's rule [100]:

$$\frac{1}{\mu_{\mathrm{tot}}(T)} = \frac{1}{\mu_{\mathrm{bulk}}(T)} + \frac{1}{\mu_{\mathrm{bound}}} + \frac{1}{\mu_{\mathrm{imp}}(T)}, \tag{4.1}$$

where μ_{bulk} is the carrier mobility in bulk crystalline bismuth, and $\mu_{\mathrm{bound}}^{-1}$ and μ_{imp}^{-1} account for boundary scattering and charged impurity scattering, respectively. The T dependence of $\mu_{\mathrm{bulk}}(T)$ is mainly due to electron-phonon scattering [90], while μ_{bound} is assumed to be T-independent. For most bulk materials, impurity scattering contributes to a temperature-dependent mobility $\mu_{\mathrm{imp}} \sim T^{3/2}$, and the same temperature dependence is assumed for nanowires. The curve for the 36-nm Bi nanowires in Fig. 4-3 is fitted by $\mu_{\mathrm{bound}} = 33\,\mathrm{m^2V^{-1}s^{-1}}$ and $\mu_{\mathrm{imp}} = 0.2 \times T^{3/2}\,\mathrm{m^2V^{-1}s^{-1}}$, and the uncontrolled impurity contribution is fitted to $N_{\mathrm{imp}} \simeq 5 \times 10^{16}\,\mathrm{cm^{-3}}$. The data (solid curve) for the 70-nm Bi nanowires are fitted by $\mu_{\mathrm{bound}} \simeq 50\,\mathrm{m^2V^{-1}s^{-1}}$ and $\mu_{\mathrm{imp}} \simeq 1.0 \times T^{3/2}\,\mathrm{m^2V^{-1}s^{-1}}$. Since the 70-nm Bi nanowires are semimetallic, the

carrier density contribution due to N_{imp} can be neglected. The smaller value of μ_{bound}^{-1} for the 70-nm wires relative to that for the 36-nm wires is attributed to a smaller fraction of atoms on the 70-nm nanowire surface. The T dependence of $R(T)$ of Bi nanowires, which is found to be strongly affected by the crystal quality, can be accounted for in this transport model by the value of μ_{bound}. Instead of a non-monotonic behavior for semimetallic Bi nanowires as shown in Fig. 4-3, $R(T)$ is predicted to have a monotonic T dependence at a higher defect level. The dashed curve in Fig. 4-3 shows the calculated $R(T)/R(270\,\text{K})$ for 70-nm wires with increased boundary scattering ($\mu_{\text{bound}} \simeq 6\,\text{m}^2\text{V}^{-1}\text{s}^{-1}$), exhibiting a monotonic T dependence similar to that of Bi nanowires synthesized by electrochemical deposition [101].

4.2.2 Significance of the Semimetal-Semiconductor Transition to the T-Dependent Resistance

In order to investigate the influence of the semimetal-semiconductor transition in Bi-related nanowires on their transport properties, we have fabricated 65-nm $\text{Bi}_{1-x}\text{Sb}_x$ nanowires with different Sb concentrations and performed the temperature-dependent resistance (see Fig. 4-4). According to the phase diagram of $\text{Bi}_{1-x}\text{Sb}_x$ nanowires in Section 3.4.1 (Fig. 3-7), 65-nm $\text{Bi}_{1-x}\text{Sb}_x$ nanowires are expected to undergo a semimetal-semiconductor transition at $x \sim 0.03$ as x increases. In Fig. 4-4, the measured resistivity of pure Bi nanowires exhibits a non-monotonic T dependence with a maximum at $\sim 70\,\text{K}$, while the resistivities of the two alloy nanowire samples (with 5 at% and 10 at% Sb) decrease monotonically with increasing T. In addition, the resistance of the $\text{Bi}_{0.95}\text{Sb}_{0.05}$ nanowires displays a stronger T dependence than that of the $\text{Bi}_{0.90}\text{Sb}_{0.10}$ nanowires. We note that this non-monotonic shift in $R(T)/R(270\,\text{K})$ of $\text{Bi}_{1-x}\text{Sb}_x$ nanowires as a function of Sb content is strikingly similar to the non-monotonic shift in $R(T)/R(300\,\text{K})$ of pure Bi nanowires as a function of wire diameter (see Fig. 4-2). The resemblance in the two sets of experimental findings suggests that in Bi nanowires, the alloying with Sb and the reduction of wire diameter may have
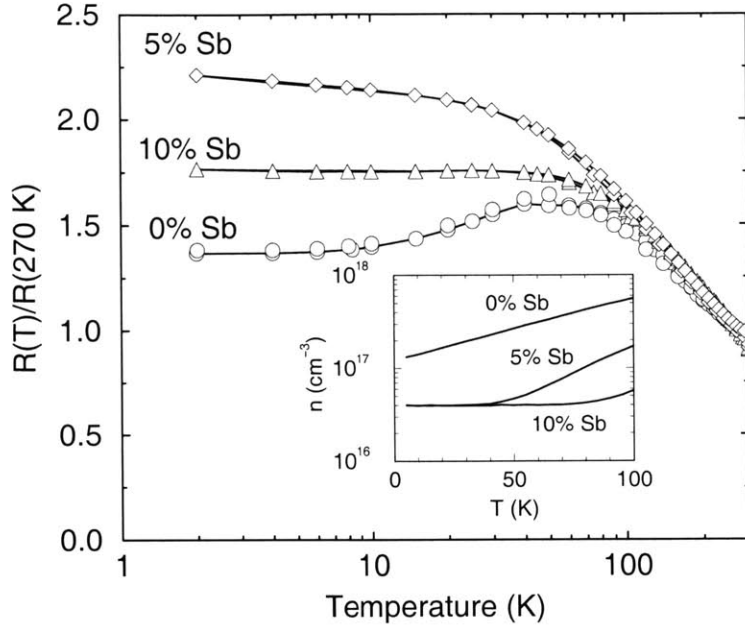
Figure 4-4: Temperature dependence of $R(T)/R(270\,\mathrm{K})$ for 65-nm $\mathrm{Bi}_{1-x}\mathrm{Sb}_x$ nanowires with different Sb contents. The inset shows the calculated carrier density as a function of temperature for these 65-nm $\mathrm{Bi}_{1-x}\mathrm{Sb}_x$ nanowires, assuming an impurity carrier concentration of 4×10^{16} cm^{-3}.

common effects on the band structure and transport properties, i.e. the semimetal-semiconductor transition [79]. Therefore, both Figs. 4-4 and 4-2 indicate that in Bi-related nanowire systems, semiconducting wires possess a monotonically decreasing $R(T)$ with increasing T, whereas semimetallic nanowires exhibit a maximum resistivity below 100 K. The agreement between these two sets of experiments not only provides strong evidence for the semimetal-semiconductor transition in Bi-related nanowire systems, but also validates the phase diagram predicted for $\mathrm{Bi}_{1-x}\mathrm{Sb}_x$ nanowires.

The reason for a weakened temperature dependence for semiconducting wires with increasing band gap is due to carriers contributed by uncontrolled impurities. We note that in Fig. 4-4, the resistivity of semiconducting wires (with 5 at% and 10 at% Sb) saturates at low temperatures instead of exhibiting a T dependence of $\exp(E_g/2kT)$ characteristic of semiconductors with a band gap E_g. This resistivity saturation behavior was also observed for semiconducting Bi nanowires in Fig. 4-2, and it was attributed to uncontrolled impurities introduced during the nanowire

71
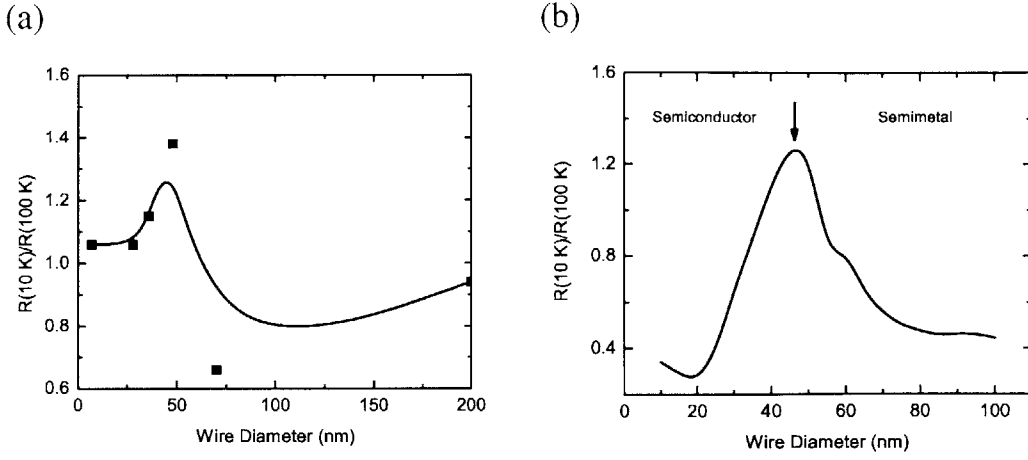
Figure 4-5: (a) Measured and (b) calculated $R(10\,\mathrm{K})/R(100\,\mathrm{K})$ as a function of Bi nanowire diameter [102].

synthesis process. The uncontrolled impurity density, which was estimated to be on the order of $10^{16}\,\mathrm{cm}^{-3}$ (see Sec. 4.2.1), has little effect on the total carrier concentration for semimetallic wires that usually have an intrinsic carrier density higher than $10^{17}\,\mathrm{cm}^{-3}$. However, the presence of extrinsic carriers is important to the transport behavior of semiconducting wires, especially at low temperatures. For semiconducting wires with a larger band gap, the extrinsic carriers that have a T-independent carrier concentration will dominate over thermally excited carriers over a broader temperature range as T increases (see the inset of Fig. 4-4), resulting in a weaker T dependence of the resistance, as observed experimentally.

Fig. 4-5(a) shows the measured $R(10\,\mathrm{K})/R(100\,\mathrm{K})$ of Bi nanowires as a function of wire diameter [102]. The solid line in Fig. 4-5(a) is a guide to the eye. The resistance ratio is chosen between 10 K and 100 K because (1) the resistance becomes relatively constant below 10 K, and (2) the band structure parameters of Bi and $\mathrm{Bi}_{1-x}\mathrm{Sb}_x$ are highly T-dependent above 100 K, and these parameters are relatively T-independent and reliably known below 100 K. Therefore, it is sensible to compare theoretical calculations with experimental results in the temperature range of 10 K to 100 K. In Fig. 4-5(a), a maximum in $R(10\,\mathrm{K})/R(100\,\mathrm{K})$ is clearly observed at $d_w \sim 50\,\mathrm{nm}$, which is very close to the predicted critical wire diameter for the semimetal-semiconductor transition of Bi nanowires. To interpret this peak in $R(10\,\mathrm{K})/R(100\,\mathrm{K})$, we show

72

in Fig. 4-5(b) the calculated resistance ratio of Bi nanowires as a function of wire diameter [102]. In deriving the curve in Fig. 4-5(b), we considered both the carrier concentration contributed by uncontrolled doping impurities and additional scattering mechanisms introduced by charged impurities and by the wire boundary. These parameters were previously determined in Section 4-2, yielding an impurity carrier concentration of $\sim 5 \times 10^{16}\,\mathrm{cm}^{-3}$, and a mobility related to the charged impurities $\mu_{imp} = 1.0 \times T^{3/2}\,\mathrm{m}^2\mathrm{V}^{-1}\mathrm{S}^{-1}$. The mobility related to the wire boundary scattering μ_{bound} is dependent on the wire diameter d_w, and the following relation, obtained by curve fitting in accordance with Matthiessen's rule, is assumed: $\mu_{bound}^{-1} = 0.001 + 0.741 d_w^{-1}\,(\mathrm{m}^2\mathrm{V}^{-1}\mathrm{S}^{-1})$, where d_w is in units of nm. The calculated $R(10\,\mathrm{K})/R(100\,\mathrm{K})$ in Fig. 4-5(b) shows a maximum around the critical wire diameter for the phase transition (indicated by the arrow), and the calculated trend with wire diameter agrees surprisingly well with the experimental results in Fig. 4-5(a). For smaller diameter nanowires, the calculated $R(10\,\mathrm{K})/R(100\,\mathrm{K})$ is lower than the experimental values, possibly due to an overestimation of carrier mobility for these finer nanowires, since the crystalline grain size may be smaller in them. Nevertheless, the good agreement between Figs. 4-5(a) and (b) not only validates the theoretical model developed for Bi nanowires, but illustrates that the semimetal-semiconductor transition in Bi nanowires can be established from the plot of $R(10\,\mathrm{K})/R(100\,\mathrm{K})$ vs. wire diameter. As the wire diameter decreases, $R(10\,\mathrm{K})/R(100\,\mathrm{K})$ of semimetallic wires increases due to the decreased band overlap between the conduction and the valence bands, whereas $R(10\,\mathrm{K})/R(100\,\mathrm{K})$ decreases for semiconducting wires due to the increasing dominance of extrinsic carriers.

A maximum in $R(10\,\mathrm{K})/R(100\,\mathrm{K})$ vs. x that is related to the semimetal-semiconductor transition is also observed for 65-nm $\mathrm{Bi}_{1-x}\mathrm{Sb}_x$ nanowires. Assuming an extrinsic impurity carrier concentration of $4 \times 10^{16}\,\mathrm{cm}^{-3}$, we calculated the total carrier concentration for the 65-nm $\mathrm{Bi}_{1-x}\mathrm{Sb}_x$ nanowires below 100 K (see Fig. 4-4). The ratios of the total carrier concentration $n(100\,\mathrm{K})/n(10\,\mathrm{K})$ are calculated as 4.2, 4.3 and 1.4 for $\mathrm{Bi}_{1-x}\mathrm{Sb}_x$ nanowires with 0, 5, and 10 at% Sb, respectively. Based on the calculated carrier concentration and the measured resistance, the average

73
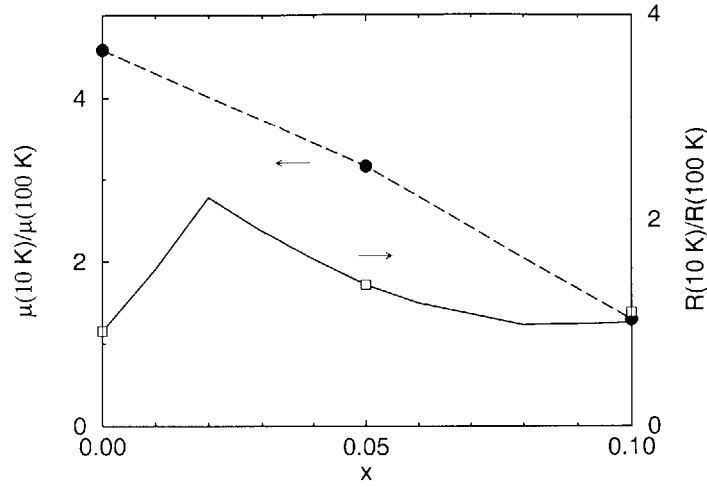
Figure 4-6: $\mu(10\,\text{K})/\mu(100\,\text{K})$ ($\bullet$) and the predicted $R(10\,\text{K})/R(100\,\text{K})$ ($\square$) for 65-nm $\text{Bi}_{1-x}\text{Sb}_x$ nanowires as a function of x.

mobility ratio $\mu(10\,\text{K})/\mu(100\,\text{K})$ is obtained for the three samples, as shown by the dashed curve in Fig. 4-6. We note that although the measured resistance ratio $R(10\,\text{K})/R(100\,\text{K})$ shows complex variations as a function of Sb content x (see Fig. 4-6), the mobility ratio of 65-nm nanowires simply decreases monotonically with x. The results indicate that the carrier mobility becomes less T dependent as x increases due to increased neutral impurity scattering. Assuming a linear dependence to interpolate the mobility ratio for $0.00 \leq x \leq 0.10$, the resistance ratio $R(10\,\text{K})/R(100\,\text{K})$ for 65-nm $\text{Bi}_{1-x}\text{Sb}_x$ nanowires is calculated as a function of x, as shown by the solid curve in Fig. 4-6. The maximum in the resistance ratio $R(10\,\text{K})/R(100\,\text{K})$ at $x \sim 0.02$ corresponds to the Sb content for the predicted semimetal-semiconductor transition. Thus, the transport model we have developed not only is able to explain the complex behavior of the $R(T)$ results, but also suggests an approach to experimentally determine the actual condition for the semimetal-semiconductor transition.

4.2.3 T-Dependent Resistance of 40-nm $\text{Bi}_{1-x}\text{Sb}_x$ Nanowires

As discussed in the previous section, the transport phenomena of pure Bi or 65-nm $\text{Bi}_{1-x}\text{Sb}_x$ nanowires are dominated by the semimetal-semiconductor transition as the wire diameter or the Sb concentration varies. However, it is also informative to study
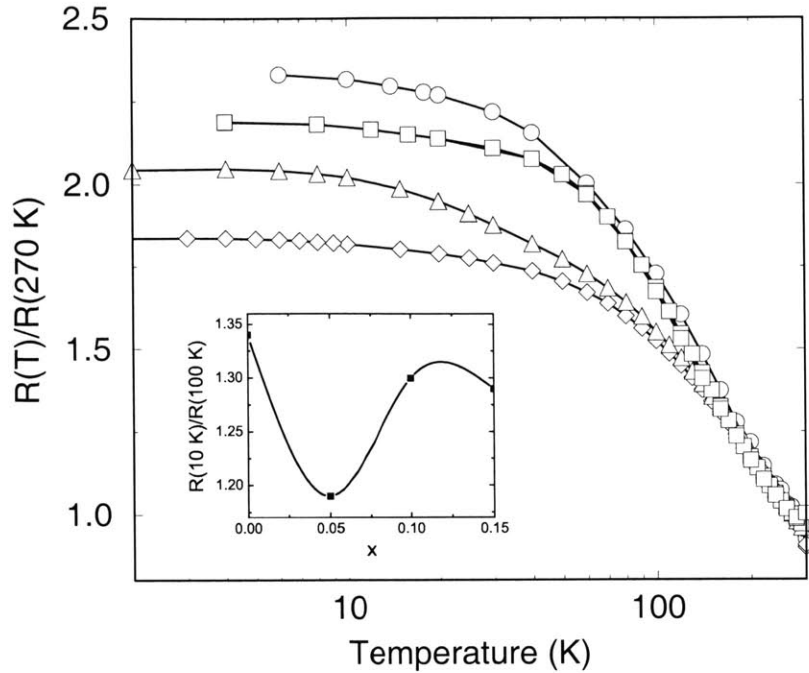
Figure 4-7: Measured $R(T)/R(270\,\mathrm{K})$ for 40-nm $\mathrm{Bi_{1-x}Sb_x}$ nanowires of $x = (\circ)$ 0.00, $(\diamond)$ 0.05, $(\triangle)$ 0.10, and $(\square)$ 0.15 [103]. The inset shows the measured $R(10\,\mathrm{K})/R(100\,\mathrm{K})$ as a function of Sb content x.

the transport properties of semiconducting nanowires with diameters below 50 nm, where the presence of multiple carrier pockets becomes important.

Figure 4-7 shows the measured $R(T)/R(270\,\mathrm{K})$ of 40-nm $\mathrm{Bi_{1-x}Sb_x}$ nanowires with various Sb concentrations for $2\,\mathrm{K} \leq T \leq 300\,\mathrm{K}$ [103]. According to the phase diagram of $\mathrm{Bi_{1-x}Sb_x}$ nanowires (see Fig. 3-7), these 40-nm nanowires are all semiconductors below 100 K. As shown in Fig. 4-7, the semiconducting nanowires exhibit a qualitatively similar monotonic T-dependent resistance. $R(10\,\mathrm{K})/R(100\,\mathrm{K})$ shows a *non-monotonic* behavior as x increases (see the inset of Fig. 4-7), which is due to competing interactions resulting from variation in the band structure and change in carrier mobilities induced by Sb atoms. For the same reasons for a highly T-dependent band structure above 100 K stated in the previous section, we can compare the experimental results with theoretical calculations for $T \leq 100\,\mathrm{K}$. The electrical conductivity of

a system with multiple carriers can be expressed as:

$$\sigma = \sum_i e n_i \mu_i = e n \sum_i \gamma_i \mu_i, \tag{4.2}$$

where n_i and μ_i are the carrier density and the mobility for each type of carrier pocket. $n = \sum_i n_i$ is the total carrier concentration, and $\gamma_i \equiv n_i/n$ is the relative population for each type of carrier. In $Bi_{1-x}Sb_x$ nanowires, carriers of various pockets possess very different mobilities, so σ is sensitive to the relative population γ_i in each carrier pocket.

Fig. 4-7 shows that the resistance ratios $R(10\,K)/R(100\,K)$ of $Bi_{1-x}Sb_x$ nanowire arrays are 1.34, 1.19, 1.30 and 1.29 for $x = 0$, 0.05, 0.10, and 0.15, respectively. To understand the transport behavior of $Bi_{1-x}Sb_x$ nanowires as a function of x, we examine both the change in n and the shift in carrier population among the different carrier pockets between $10\,K$ and $100\,K$. Assuming a modest n-type impurity concentration of 10^{16} cm^{-3}, the total carrier concentration ratio $n(100\,K)/n(10\,K)$ of 40-nm $Bi_{1-x}Sb_x$ nanowires is calculated as a function of x, as shown in Fig. 4-8(a). We note that $n(100\,K)/n(10\,K)$ decreases rapidly as x increases from 0.00 to 0.10, and becomes relatively flat for $x \geq 0.10$. Figure 4-8(b) shows the difference in the relative population $\Delta\gamma_i = \gamma_i(10\,K) - \gamma_i(100\,K)$ calculated for 40-nm $Bi_{1-x}Sb_x$ nanowires for the L-, T- and H-point carriers. γ_L includes contributions from both the light-mass L-point electrons and holes. Since the L-point carriers have a much higher mobility than the T- and H-point holes, the average mobility μ_{avg} is usually dominated by the relative population γ_L of the L-point carriers. Qualitatively, a larger value of $\Delta\gamma_L$ implies a larger increase in μ_{avg} as the temperature decreases, which tends to lower the value of $R(10\ K)/R(100\,K)$. The measured $R(10\,K)/R(100\,K)$ of 40-nm $Bi_{1-x}Sb_x$ nanowires can be understood based on the calculations shown in Figs. 4-8(a) and (b). For $x \leq 0.05$, since $\Delta\gamma_L$ is almost constant, $R(10\,K)/R(100\,K)$ is mainly determined by $n(100\,K)/n(10\,K)$, both of which decrease as x increases. For $x \geq 0.5$, $n(100\,K)/n(10\,K)$ is less sensitive to x, and the variation in $\Delta\gamma_L$ becomes the dominant factor. The decrease in $\Delta\gamma_L$ from 0.43 to ~ 0.20 is mainly responsible
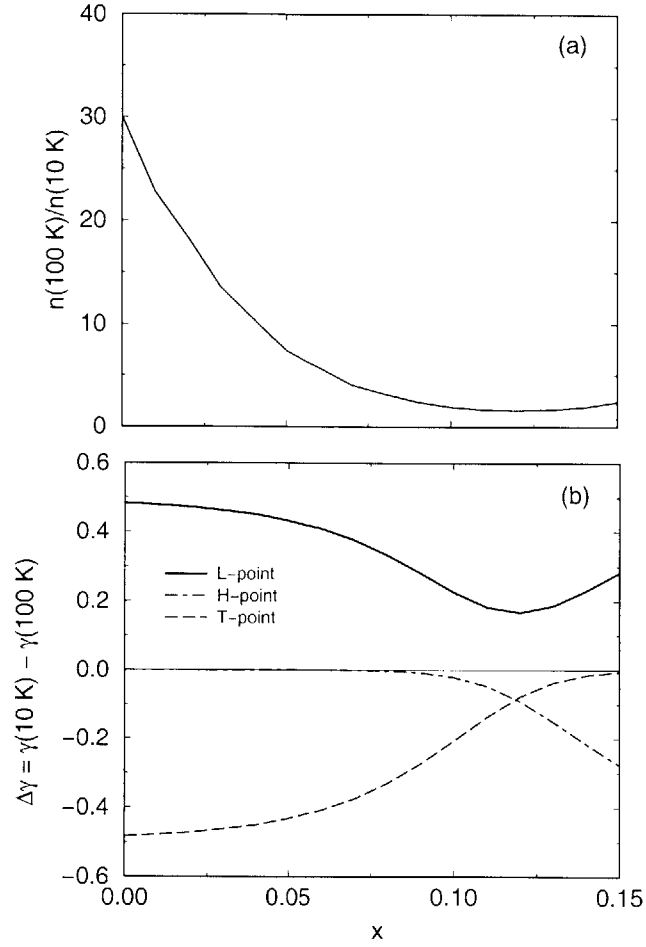
Figure 4-8: (a) Calculated ratios of the total carrier concentration $n(100\,\mathrm{K})/n(10\,\mathrm{K})$ for 40-nm $Bi_{1-x}Sb_x$ nanowires as a function of Sb content x. (b) Calculated difference of the relative populations $\Delta\gamma_i = \gamma_i(10\,\mathrm{K}) - \gamma_i(100\,\mathrm{K})$ for L-, T- and H-point carriers in 40-nm $Bi_{1-x}Sb_x$ nanowires [103].

for the increase in $R(10\,\mathrm{K})/R(100\,\mathrm{K})$ as x increases from 0.05 to 0.10. Finally, since the values of $n(100\,\mathrm{K})/n(10\,\mathrm{K})$ are similar for $x = 0.10$ and 0.15 while $\Delta\gamma_L$ is slightly higher for $x = 0.15$, we expect a lower $R(10\,\mathrm{K})/R(100\,\mathrm{K})$ value for $x = 0.15$ than for $x = 0.10$, which is consistent with the experimental results.

4.2.4 Te-doped Bi Nanowires and Sb Nanowires

In this section, the transport model developed for nanowires is extended to investigate the transport properties of Te-doped Bi nanowires and Sb nanowires.

Te is a group VI element and an electron donor in Bi. Figure 4-9(a) shows the measured $R(T)/R(270\,\mathrm{K})$ of 40-nm Bi nanowires with various nominal Te contents [99]. The actual Te content in the Bi nanowires is smaller than the nominal Te content due to the likely segregation of Te atoms to the wire boundary during alloy solidification [104]. For the following discussions, we assume that $\delta_e = 10\%$ of the Te dopants in the alloy melt are present in the final nanowires produced. A justification of the assumed δ_e values will be given in Section 4.4. With this assumption, 0.025 at%, 0.075 at%, and 0.15 at% Te-doped Bi alloys give rise to donor concentrations N_d of 6.67×10^{17}, 2.0×10^{18}, and $4.0 \times 10^{18}\,\mathrm{cm}^{-3}$ in the respective resulting nanowires. Based on the measured $R(T)$ in Fig. 4-9(a) and the calculated T-dependent carrier density, the T dependence of the average mobility μ_{avg} of these Te-doped Bi nanowires is obtained, shown as $\mu_{\mathrm{avg}}^{-1}(T)/\mu_{\mathrm{avg}}^{-1}(270\,\mathrm{K})$ in Fig. 4-9(b) [99]. μ_{avg}^{-1} of Te-doped Bi nanowires can be related to the various scattering processes by $\mu_{\mathrm{doped}}^{-1}(T) = \mu_{\mathrm{undoped}}^{-1}(T) + \mu_{\mathrm{imp}}^{-1}(T) + \mu_{\mathrm{defect}}^{-1}$, where μ_{undoped} is the average mobility of the undoped Bi nanowires of the same diameter, and μ_{imp}^{-1} and $\mu_{\mathrm{defect}}^{-1}$ are associated with the increased ionized impurity scattering and the expected higher defect level in Te-doped Bi nanowires, respectively. At high T ($> 200\,\mathrm{K}$), the three Te-doped samples in Fig. 4-9(b) exhibit a similar T dependence to that of the undoped sample, indicating that $\mu_{\mathrm{undoped}}^{-1}$ is the major contributor to $\mu_{\mathrm{doped}}^{-1}$. The average mobility of undoped Bi nanowires can be well fitted by a $\mu_{\mathrm{undoped}} \sim T^{-2.9}$ dependence for $T > 100\,\mathrm{K}$, as shown by the dashed line in Fig. 4-9(b), consistent with the predomi-

78
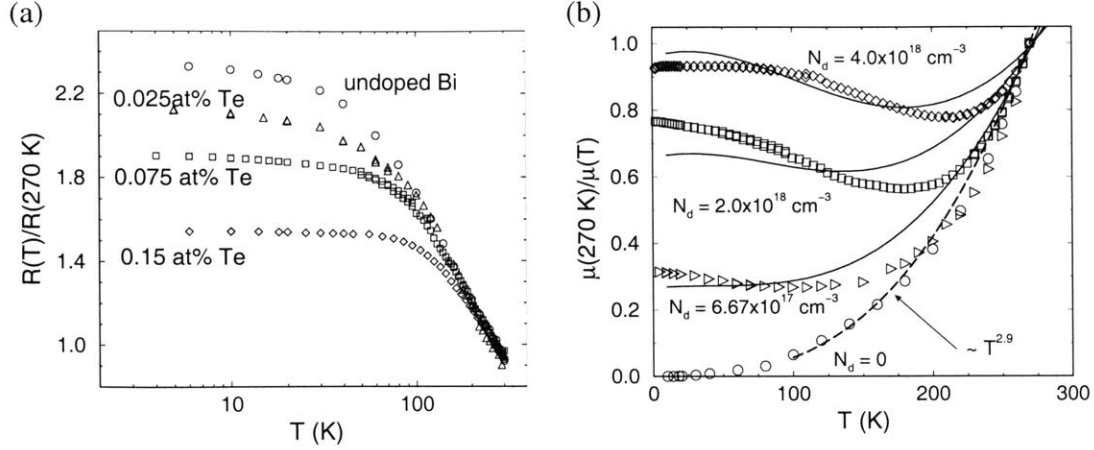
Figure 4-9: (a) Measured $R(T)/R(270\,\mathrm{K})$ for 40-nm undoped and Te-doped Bi nanowires. (b) Calculated T dependence of μ_{avg}^{-1} for 40-nm undoped and Te-doped Bi nanowires. The dashed and solid curves are fitting curves corresponding to undoped and Te-doped Bi nanowires, respectively [99].

nant electron-phonon scattering at high T. For most materials, electron-phonon scattering yields a T-dependent mobility [105] $\mu_{\mathrm{phonon}} \propto m^{*-5/2}T^{-3/2} \propto T^{-1.5}$. However, μ_{phonon} of Bi has a stronger T dependence than $T^{-1.5}$ because the effective mass m^* of Bi increases with T [90]. The term $\mu_{\mathrm{defect}}^{-1}$ that includes neutral impurity scattering is essentially T independent, while μ_{imp}^{-1} generally increases with decreasing T. Since $\mu_{\mathrm{undoped}}^{-1}$ and $\mu_{\mathrm{imp}}^{-1} + \mu_{\mathrm{defect}}^{-1}$ are dominant contributors at high and low T, respectively, a minimum in $\mu_{\mathrm{doped}}^{-1}$ is observed for Te-doped Bi nanowire arrays.

However, the $T^{-3/2}$ dependence generally expected for μ_{imp}^{-1} [105] cannot account for the much weaker T dependence observed in Te-doped Bi nanowires in Fig. 4-9(b) at low T. For ionized impurity scattering, $\tau_{\mathrm{imp}} \propto m^{*2}v^3$, where τ_{imp} is the scattering time and v is the carrier group velocity [105]. Since the L-point electrons have a non-parabolic dispersion relation, μ_{imp} for Bi nanowires has a different T dependence from that of ordinary materials with parabolic dispersion relations. The group velocity along the wire axis (z direction) for electrons in one of the subbands is calculated as

$$v_{nm}(k) = \frac{\partial E_{nm}}{\hbar \partial k} = \sqrt{\frac{2E_{gL}}{\tilde{m}_z}} \left(1 + \frac{\gamma_{nm}^2 \tilde{m}_z E_{gL}}{2\hbar^2 k^2}\right)^{-1/2}, \tag{4.3}$$

79

where $E_{nm}(k)$ is the dispersion relation of the (n, m) subband, E_{gL} is the L-point bandgap of bulk Bi, and $\tilde{m}_z = (\hat{z} \cdot \mathbf{m} \cdot \hat{z})$ is the transport effective mass along the wire. Here $\mathbf{m}$ is the electron band-edge effective mass tensor and $\gamma_{nm} = \sqrt{1 + 4\tilde{\varepsilon}_{nm}/E_{gL}}$, whereby $\tilde{\varepsilon}_{nm}$ is the subband edge energy obtained by ignoring the non-parabolic effects [79]. In Bi nanowires, the Te dopants raise E_F into the conduction band, and the group velocity of electrons responsible for the transport properties is approximately independent of energy, since $v \simeq \sqrt{2E_{gL}/\tilde{m}_z}$. Because of the T dependence of E_{gL} and $\tilde{m}_z$ [90], μ_{imp} is essentially T-independent below $80\,\text{K}$, but increases approximately linearly with increasing T above $80\,\text{K}$. Therefore, we have an expression for μ_{doped}^{-1} as

$$\mu_{\text{doped}}^{-1} \simeq aT^{2.9} + b\eta(T), \qquad (4.4)$$

where

$$\eta(T) \simeq m^*(T)^{1/2} E_{gL}(T)^{-2/3} \qquad (4.5)$$

is an approximate T dependence of $\mu_{\text{imp}}^{-1} + \mu_{\text{defect}}^{-1}$. The ratio β is defined as

$$\beta \equiv b/a, \qquad (4.6)$$

and it expresses the importance of ionized impurity scattering relative to electron-phonon scattering. The data points in Fig. 4-9(b) are fitted by the solid curves, and a β ratio of $1.0 : 3.3 : 6.5$ is found for Bi nanowires with $N_d = 6.67 \times 10^{17}$, 2.0×10^{18}, and $4.0 \times 10^{18}\,\text{cm}^{-3}$, respectively, indicating that μ_{imp}^{-1} is approximately proportional to N_d. In addition, the dependence $\beta \propto N_d$ is essentially independent of δ_e for small variation of δ_e.

Like Bi, Sb is a semimetal in the bulk form. The band overlap between electrons and holes in Sb is about $180\,\text{meV}$ at $4\,\text{K}$, which is about five times larger than that in Bi ($\sim 38\,\text{meV}$). Therefore, the semimetal-semiconductor transition would occur at a smaller wire diameter ($\sim 10\,\text{nm}$) in Sb nanowires compared to Bi nanowires ($\sim 50\,\text{nm}$). Figure 4-10(a) shows the temperature dependence of the resistance for Sb nanowires prepared by vapor deposition [106]. One of the 10-nm nanowire arrays
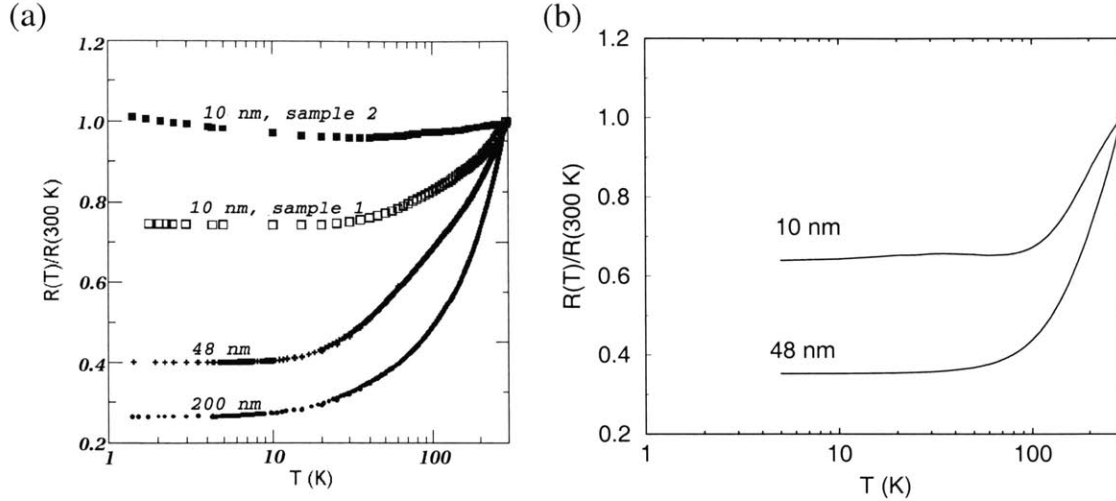
Figure 4-10: (a) Measured $R(T)/R(300\,\mathrm{K})$ of various Sb nanowires [106]. (b) Calculated $R(T)/R(300\,\mathrm{K})$ for 10-nm and 40-nm Sb nanowires [106].

has less temperature variation than the other, probably due to differences in impurity content or wire diameter distribution within the anodic alumina templates. Fig. 4-10(b) illustrates the modeled normalized resistance $R(T)/R(300\,\mathrm{K})$ curves for 10-nm and 48-nm Sb nanowire arrays [106], which display trends that are qualitatively consistent with the experimental results shown in Fig. 4-10(a).

The fact that the measured $R(T)$ of Sb and Te-doped Bi nanowires can be explained by the same transport model not only corroborates our theoretical calculations and predictions made for the general nanowire systems, but also suggests that the different T dependences of the resistance between nanowires and bulk materials arise from both quantum finite-size effects and classical finite-size effects. The classical finite-size effect decreases the carrier mobility by limiting the carrier mean free path, whereas the quantum confinement effect alters the band structure (especially for semimetals) and significantly changes the carrier density and mobility. These two factors determine the temperature-dependent transport properties in the nanowire systems.
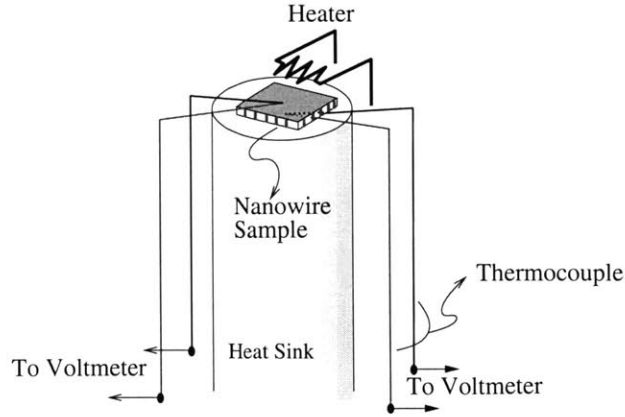
Figure 4-11: Experimental set-up for Seebeck measurements of nanowire arrays.

4.3 Seebeck Coefficient Measurements

The Seebeck coefficient measurements are essential for evaluating the performance of thermoelectric materials. However, due to the difficulties associated with the thinness of nanowire arrays, there has been limited progress in the S measurements of nanowire arrays until recently [107].

The experimental set-up for the Seebeck coefficient measurement is shown in Fig. 4-11. Two E-type thermocouple junctions (OMEGA Engineering, Inc.) are placed on both sides of the nanowire arrays. The thermocouple used here is only $25\,\mu$m in diameter; it is the smallest thermocouple commercially available. Small thermocouples are critical in Seebeck coefficient measurements in order to reduce the heat capacity of the probe and to minimize the heat transfer through the thermocouple. The thermocouples and the nanowire arrays are attached to a heat sink, and a resistor ($\sim 100\,\Omega$) is placed on top of the nanowire array as a heater. In this set-up, the connection points of the thermocouple with voltmeters should be kept at a distance from the heater to avoid errors due to temperature fluctuations.

Figure 4-12 shows the measured Seebeck coefficient as a function of temperature for nanowire arrays with different diameters and Sb contents [98]. The Seebeck coefficient for bulk Bi (taken from excess Bi pieces after the pressure injection and annealing processes) was also measured using a similar experimental setup, and the results are shown as the solid curve in Fig. 4-12 for comparison. The measured Seebeck coeffi-
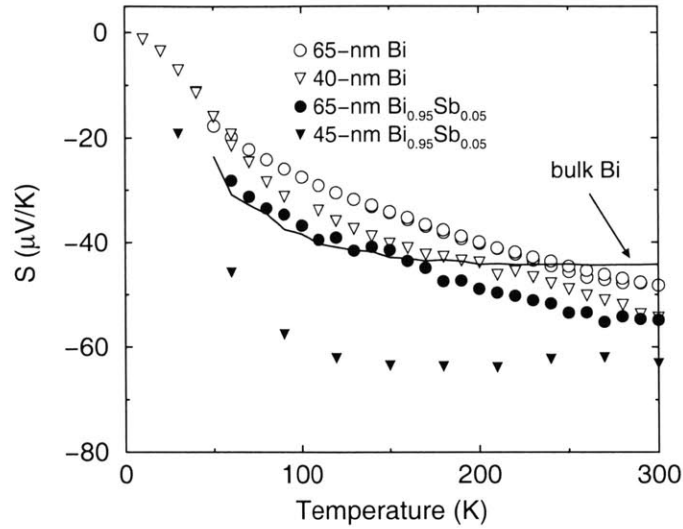
Figure 4-12: Measured Seebeck coefficient as a function of T for Bi ($\circ$, $\triangledown$) and Bi$_{0.95}$Sb$_{0.05}$ ($\bullet$, $\blacktriangledown$) nanowires with different diameters [98]. The solid curve denotes the Seebeck coefficient for bulk Bi.

cient of the bulk Bi sample is about $-45\,\mu$V/K at room temperature, which is in good agreement with values from the literature, as well as with its temperature dependence $\partial S/\partial T$ [89]. The measured Seebeck coefficients of 65-nm and 40-nm Bi nanowires at 300 K are -48 and $-55\,\mu$V/K, respectively. It is expected that the Seebeck coefficient of 65-nm and 40-nm Bi nanowires would be close to the bulk value at 300 K, since quantum confinement effects are not pronounced for $d_w \geq 40$ nm at room temperature. Although the measured Seebeck coefficients of nanowire arrays are usually underestimated, these results on nanowire array measurements are encouraging and important in validating the experimental techniques used.

In Fig. 4-12, the Seebeck coefficients of 40-nm nanowires are larger in magnitude than that of 65-nm nanowires for both Bi and Bi$_{0.95}$Sb$_{0.05}$ over the temperature range measured, which may be due to sharper density of states features and a smaller band overlap as the wire diameter decreases [79]. For 40-nm and 65-nm Bi nanowires alloyed with $5\,$at% Sb, we note some increase in the Seebeck coefficient over that for pure Bi nanowires, with the finer nanowires showing a more significant enhancement.

83
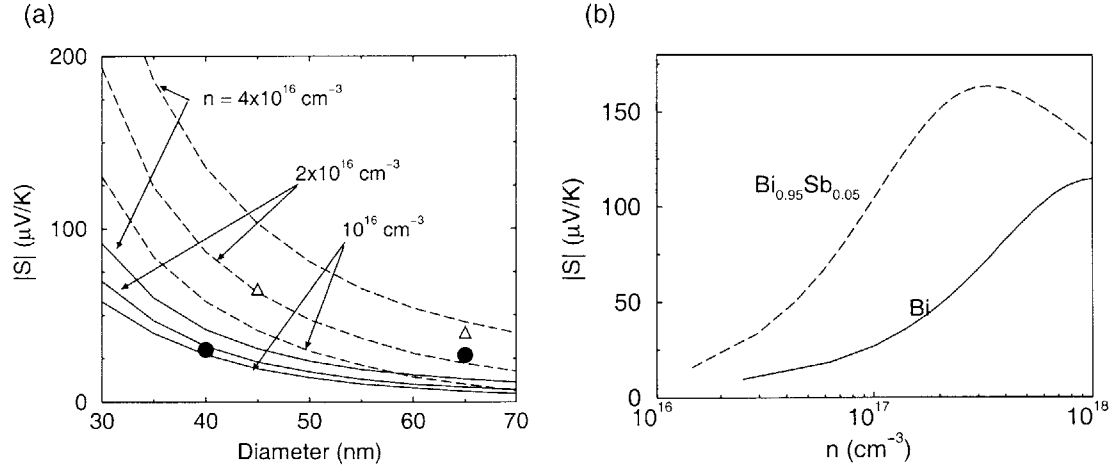
Figure 4-13: (a) Theoretically predicted magnitude of the Seebeck coefficient as a function of d_w at 100 K for Bi (—) and $Bi_{0.95}Sb_{0.05}$ (- - -) nanowires of different dopant concentrations. Also shown in the figure are measured $|S|$ of Bi ($\bullet$) and of $Bi_{0.95}Sb_{0.05}$ ($\triangle$) nanowires at 100 K. (b) Calculated $|S|$ as a function of carrier concentration at 100 K for 65-nm Bi (—) and $Bi_{0.95}Sb_{0.05}$ (- - -) nanowires.

These results indicate that Sb alloying and the confinement effects in Bi are both effective at decreasing the band overlap and enhancing the thermopower, consistent with the theoretical predictions.

From the measured Seebeck coefficients and theoretical model calculations, we can extract valuable information, such as the Fermi energy and the carrier concentration. Based on the transport model for $Bi_{1-x}Sb_x$ nanowires, Fig. 4-13(a) shows the calculated Seebeck coefficient as a function of wire diameter for Bi and $Bi_{0.95}Sb_{0.95}$ nanowires at three different n-type dopant concentrations (1×10^{16}, 2×10^{16} and $4 \times 10^{16}\,\mathrm{cm}^{-3}$) at 100 K [98]. Also shown in Fig. 4-13(a) are the measured Seebeck coefficients of Bi ($\bullet$) and $Bi_{0.95}Sb_{0.05}$ ($\triangle$) nanowires at 100 K. Good agreement between the experimental results and the theoretical model is obtained, and the corresponding dopant carrier concentrations ($\sim 1 \times 10^{16}$ to $4 \times 10^{16}\,\mathrm{cm}^{-3}$) also agree with the uncontrolled impurity carrier concentrations derived in previous sections. Fig. 4-13(b) shows the calculated $|S|$ as a function of carrier concentration n for 65-nm Bi and $Bi_{0.95}Sb_{0.05}$ nanowires, illustrating the difference in the dependence of $|S|$ on n between semimetallic and semiconducting nanowires [98]. We note that $|S|$ is much

more sensitive to n in semiconducting nanowires (i.e. $Bi_{0.95}Sb_{0.05}$) than in semimetallic nanowires (i.e. Bi nanowires with $d_w \geq 50\,nm$), as reflected by the larger increase in $|S|$ as the carrier concentration n increases for $Bi_{0.95}Sb_x$ nanowires in Fig. 4-13(b). This is because the Fermi level has a stronger dependence on n for semiconducting wires. This observation results in two important implications that may be useful for characterizing nanowires. First, from the change in Seebeck coefficient as a function of carrier concentration, we may be able to distinguish semiconducting nanowires from semimetallic wires if the carrier concentration can be controlled. In addition, the strong dependence of the Seebeck coefficient on the carrier concentration for semiconducting nanowires renders the S measurement a promising probe to determine the carrier concentration in nanowires. From Fig. 4-13, it is also expected that a higher Seebeck coefficient can be achieved at higher carrier concentrations ($n > 10^{17}\,cm^{-3}$) by intentionally doping the nanowires with electron donors (e.g. Te). Assuming a doping efficiency $\delta_e \sim 0.1$ for Te dopants in Bi nanowires (see Section 4.2.4), Te dopant concentrations of ~ 0.04 at% and ~ 0.02 at% should be used in preparing 65-nm Bi and $Bi_{0.95}Sb_{0.05}$ nanowires, respectively, in order to achieve the maximum thermopower.

Recently, Heremans et $al.$ have observed a substantial increase in the thermopower of Bi nanowires as the wire diameter further decreases, as shown in Fig. 4-14(a) for 15-nm Bi/silica and 9-nm Bi/alumina nanocomposites [58]. The enhancement is due to the sharp density of states near the Fermi energy in a 1D system. Although the samples in Fig. 4-14(a) also possess very high electrical resistance ($\sim G\Omega$), the results for the 9-nm Bi/alumina samples show that the Seebeck coefficient can be enhanced by ~ 1000 times relative to bulk Bi. However, for Bi nanowires with very small diameters ($\sim 4\,nm$), the localization effect becomes dominant, which compromises the thermopower enhancement. Therefore, the optimal wire diameter range for the largest thermopower enhancement is expected to be between 4 nm and 15 nm [58] for Bi nanowires.

The effect of diameter on the thermopower of nanowires has also been observed in Zn nanowires [58]. Fig. 4-14(b) shows the Seebeck coefficients of 9-nm Zn/alumina
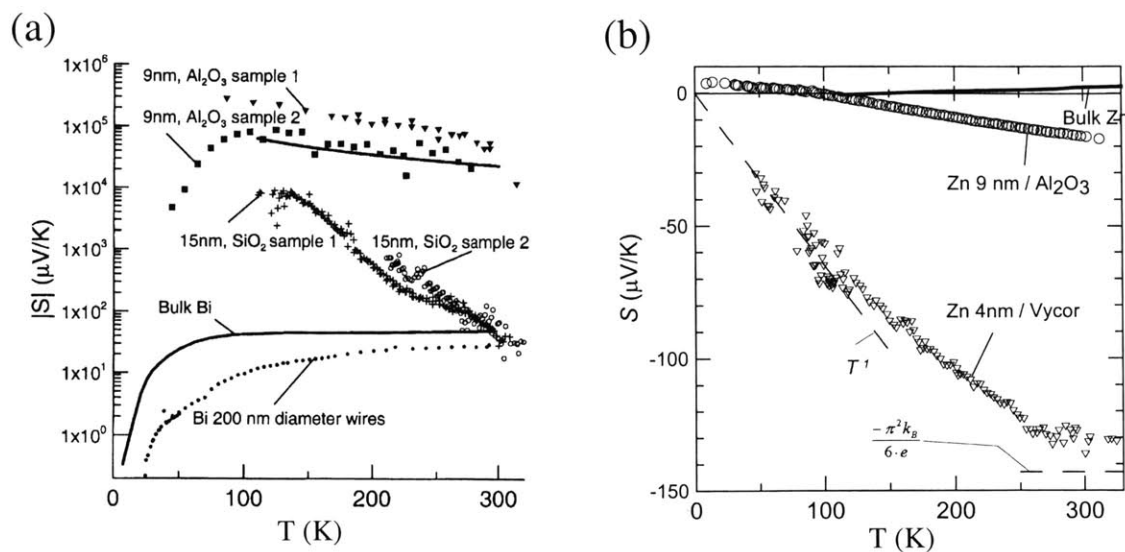
Figure 4-14: (a) Absolute values of the Seebeck coefficient of two 15-nm Bi/silica samples and two 9-nm Bi/alumina samples [58]. The solid straight line is a fit to a T^{-1} law [58]. (b) Measured Seebeck coefficient as a function of temperature for 9-nm Zn/Al_2O_3 and 4-nm Zn/Vycor glass samples in comparison to that of bulk Zn [58].

and 4-nm Zn/Vycor glass nanocomposites, which also exhibit enhanced thermopower as the wire diameter decreases. It is interesting to compare the electronic band structure of Zn to that of Bi, because like Bi, Zn also possesses electrons and holes simultaneously due to band overlap effects. Zn is a group IIB element, which has 2 nearly free electrons per atom, and therefore should have a fully filled Brillouin zone. The band overlap in Zn causes the electrons to spill over to the next Brillouin zone, thus creating holes in the first Brillouin zone. However, unlike Bi, Zn is considered to be a metal because of its much larger Fermi surfaces. It is found that while 9-nm Zn nanowires still exhibit metallic behavior, the thermopower of 4-nm Zn nanowires is very large, and shows a different temperature dependence that is not linear in T with a saturation effect above 250 K. These unusual temperature-dependent effects may be due to the 1D localization effect, although further investigation is required for a definitive identification of the conduction mechanism in such small nanowires.

In summary, the Seebeck coefficient of nanowires exhibits a different temperature dependence from that of their bulk counterparts, as well as an enhanced thermopower

under certain conditions. The different temperature dependence of the thermopower for nanowires and for bulk materials results from the fact that the thermopower of nanowires is determined by the relative magnitude of the thermal energy $k_B T$, which increases with increasing temperature, and by the subband energy separation due to quantum confinement effects, which usually possesses a weaker temperature dependence. Generally speaking, nanowires possess a larger Seebeck coefficient than their bulk counterparts because of the sharp density of states features that are unique to 1D systems. In the case of Bi nanowires, the semimetal-semiconductor transition further enhances their thermopower by eliminating the cancellation between the contributions to S from electrons and holes. However, for nanowires with very small diameters ($< 5\,\mathrm{nm}$), the scattering mechanism and the energy dependence of the scattering time may be significantly affected by 1D localization effects, and, depending on the materials, the thermopower may be reduced (e.g. Bi) or enhanced (e.g. Zn).

4.4   Determination of the Carrier Concentration

The carrier density and the Fermi energy in nanowires are important fundamental parameters in determining their transport properties and in optimizing their thermoelectric performance. Conventional techniques used to obtain the Fermi energy or carrier concentration in bulk crystalline materials include the Hall measurements, Shubnikov-de Haas effects in a magnetic field, and plasma frequency from optical measurements. However, due to the quasi-1D nature and the small size of nanowires, these techniques may not be directly applicable to nanowires, and some indirect means is usually required to determine the Fermi energy and carrier concentration experimentally in nanowires.

Due to the limited experimental methods available to study nanowires, theoretical modeling plays an important role in deriving the Fermi energy from available transport measurements. For Te-doped Bi nanowires, the carrier concentration N_d

contributed by the Te donor atoms, which may deviate significantly from the nominal Te concentration in the alloy melt, can be obtained by comparing the temperature dependence of the experimentally-derived carrier mobility with that of the calculated carrier mobility in accordance with Matthiessen's rule. The doping efficiency δ_e, defined as the ratio between the actual Te donor concentration in nanowires and the nominal Te concentration, may also be dependent on the nominal Te concentration. As discussed in Section 4.2.4, a model for the temperature-dependent carrier mobility of Te-doped Bi nanowires is given by Eq. (4.4), and the parameter β, defined in Eq. (4.6), represents the importance of the ionized impurity scattering relative to the electron-phonon scattering processes. For a measured $R(T)$ curve and a given N_d, β can be obtained by fitting Eq. (4.4) with the carrier mobility μ_{eff} derived experimentally using $\sigma(T) = en(T)\mu_{\text{eff}}(T)$, where $n(T)$ is the total carrier concentration. Based on the measured $R(T)$ for Te-doped Bi nanowire arrays in Fig. 4-9(a), Fig. 4-15 shows the calculated β values as a function of N_d for three Te-doped Bi nanowires with nominal Te concentrations of 0.025 at%, 0.075 at%, and 0.150 at%. The various data points of each nanowire sample denote the calculated β values, assuming different doping efficiencies ($\delta_e = 0.1, 0.2, 0.3, ...$). Although these data points form all possible combinations of β-N_d pairs for each nanowire sample, only the pair that has the actual donor concentration reflects the real nanowires we measured and is physically meaningful. We note that for large δ_e values, there are no satisfactory fitting between the measured mobility and Eq. (4.4), and the upper limits of δ_e are found to be 0.6, 0.3, and 0.2 for 0.025 at%, 0.075 at%, and 0.150 at% Te-doped Bi nanowires, respectively. In order to determine the β-N_d pairs that correspond to the actual samples, the following correlation between β and N_d should be further considered. Since the ionized impurity scattering strength is proportional to the charged impurity density N_d, the parameter β is expected to increase linearly with N_d. An empirical relation between β and N_d, which satisfies the above constraint and passes through certain β-N_d pairs of all three Te-doped Bi nanowire samples, is given by $\beta = 2.48 \times 10^{-18} N_d$, where N_d is in units of cm^{-3} (see the dashed line in Fig. 4-15). According to this empirical relation, the doping efficiency δ_e is
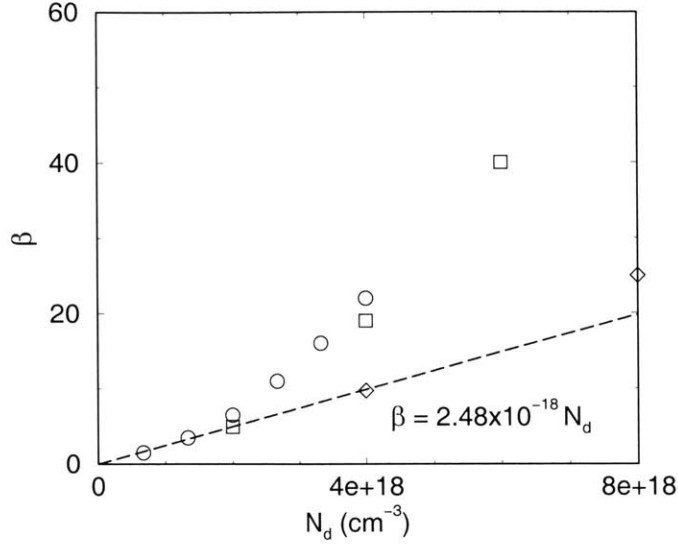
Figure 4-15: Calculated β values as a function of donor carrier concentration N_d for three Te-doped Bi nanowires with nominal Te concentrations of 0.025 at% ($\circ$), 0.075 at% ($\square$), and 0.150 at% ($\diamond$). The various data points of each nanowire sample denote the calculated β values assuming different doping efficiencies ($\delta_e = 0.1, 0.2, 0.3, ...$). The dashed line shows the empirical relation derived for β and N_d.

found to be ~ 0.10 for 0.075 at% and 0.150 at% Te-doped Bi nanowires, and it is slightly higher ($\delta_e \sim 0.15$) for 0.025 at% Te-doped Bi nanowires, indicating that in nanowires, δ_e increases somewhat with decreasing nominal Te dopant concentration. We note that this empirical relation is of great significance since it provides a universal calibration curve to determine the Te donor concentration in Bi nanowires using temperature-dependent resistance measurements. With the donor concentrations N_d in the nanowires thus obtained, the Fermi energies at 77 K are calculated to be ~ 62, 78, and 97 meV for 0.025 at%, 0.075 at%, and 0.150 at% Te-doped Bi nanowires, respectively, where the zero in energy refers to the L-point conduction band edge in bulk Bi. Fig. 4-16 shows the calculated density of states as a function of energy for 40-nm Bi nanowires (oriented in the $[01\bar{1}2]$ direction) at 77 K, and the Fermi energies of the three Te-doped Bi nanowires are indicated by the arrows. Since the optimal Fermi energy for thermoelectric applications is predicted to be ~ 87 meV with a donor concentration N_d of $\sim 2.73 \times 10^{18}$ cm^{-3} [79] for 40-nm Bi nanowires oriented in the $[01\bar{1}2]$ direction, 0.100 at% Te-doped Bi alloy should be used when preparing
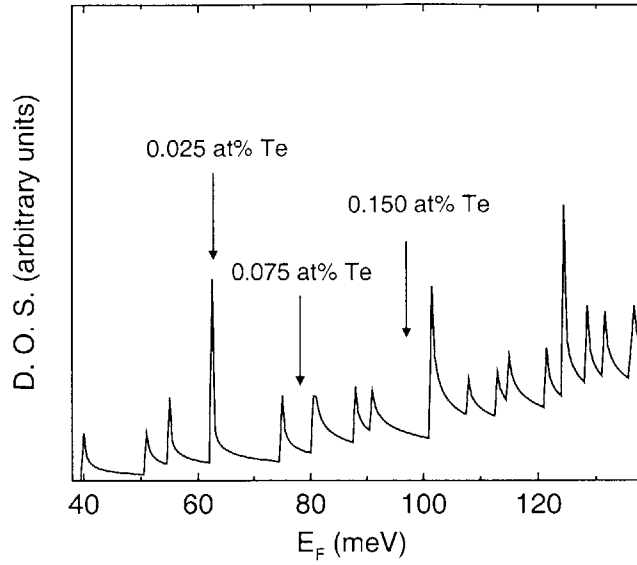
Figure 4-16: Calculated density of states as a function of energy for 40-nm Bi nanowires (oriented in the [01$\bar{1}$2] direction) at 77 K. The zero in energy refers to the L-point conduction band edge in bulk Bi. The arrows indicate the Fermi energies of 0.025 at%, 0.075 at%, and 0.150 at% Te-doped Bi nanowires at $E_F \sim 62$, 78, and 97 meV, respectively.

nanowires by pressure injection, assuming a doping efficiency of ~ 0.1, in order to achieve this optimal carrier concentration for thermoelectric applications.

Based on the same model and similar analysis techniques, the carrier concentration due to uncontrolled impurities was estimated to be on the order of 10^{16} cm^{-3} for undoped nanowire samples (see Sections 4.2.1 and 4.2.2). Although the estimated carrier density yields self-consistent results for these Bi-based nanowires, it should also be noted that, due to the lack of detailed information, which results from the nanowire distributions in an array, these estimated values should be carefully examined and checked by other measurements, such as the Seebeck coefficient measurements.

The Seebeck coefficient measurements of nanowire arrays offer a potentially promising tool to provide information related to the Fermi energy and carrier concentration, because of the sensitive dependence of the Seebeck coefficient on the Fermi energy (see Fig. 4-13). In addition, since the Seebeck coefficient measurements are intrinsically independent of the number of nanowires contributing to the signal, such measure-

ments on nanowire arrays of uniform wire diameter are, in principle, as informative as single-wire measurements. Based on the Seebeck coefficient measurements on $Bi_{1-x}Sb_x$ nanowire arrays, the carrier concentrations due to uncontrolled impurities in undoped nanowires were estimated to be $\sim 1 \times 10^{16}$ to 4×10^{16} cm^{-3} (see Section 4.3), in agreement with the values derived from the resistance measurements. Heremans *et al.* have utilized the Shubnikov-de Haas oscillations in magnetoresistance measurements of Bi nanowires [107], along with their Seebeck coefficient measurements, to calculate the carrier concentration, and they have reported higher carrier concentrations of $\sim 10^{17}$ cm^{-3} due to uncontrolled impurities for Bi nanowires synthesized by vapor deposition.

The plasma frequency in optical measurements, which is a powerful technique often employed to determine the carrier concentration in metals, may also provide valuable information related to the Fermi energy in nanowires. However, the interpretation of the optical measurements on nanowires should be carefully made, because the wire diameter is generally smaller than the wavelength of the incident light, and the results may also depend on the light polarization relative to the wire axis [14, 80]. We note that although none of the approaches described above is capable of obtaining the Fermi energy or carrier concentration of nanowires in a direct fashion without involving modeling, a good estimation of these important parameters could be achieved by comparing the results from two or more of these measurements.

4.5   Magnetoresistance Measurements

Magnetoresistance (MR) measurements provide a valuable technique for characterizing nanowires because they yield a great deal of information about the electron scattering at wire boundaries, the effects of doping and annealing on scattering, and the localization effects in nanowires [96].

Magneto-transport properties of nanowires have been extensively studied [22, 33, 96, 101, 108–110], mostly on Bi nanowires, because of their potential for applica-

tions based on giant magnetoresistance effects. The magnetoresistance of sub-10-nm Zn/SiO$_2$ nanocomposites measured by Heremans *et al.* showed interesting localization effects in 1D systems [111], and the results are in good agreement with the 1D localization model developed by Beutler and Giordano [112]. Fig. 4-17(a) shows the longitudinal MR of 40-nm Bi$_{0.85}$Sb$_{0.15}$ nanowires as a function of magnetic field B at different temperatures [103]. Other 40-nm Bi$_{1-x}$Sb$_x$ nanowire samples with smaller x values were also measured, and they exhibited MR(B) trends similar to Fig. 4-17(a). For $T \geq 4$ K, the MR at low B can be described by a parabolic relation MR $\equiv (R(B) - R(B = 0))/R(B) = A_0 B^2$, where A_0 is the magnetoresistance coefficient. In Fig. 4-17(a), A_0 increases with decreasing T, consistent with a decrease in electron-phonon scattering as T decreases. For all samples, as T decreases below 4 K, the MR exhibits a behavior rather distinct from that at higher T, as indicated by the arrow in Fig. 4-17(a). This abnormal feature is seen in the first derivative of each of the MR curves (see inset of Fig. 4-17(a)). This feature, observed previously in Bi nanowires [96], is attributed to transitional 1D-3D localization effects associated with having the magnetic length $L_H = (\hbar/eB)^{1/2}$ equal to the wire diameter d_w, and having a long phase-breaking length ($L_\phi \geq d_w$). The characteristic length L_H is the spatial extent of the wavefunction of electrons in the lowest Landau level, and L_H is independent of the carrier effective masses. Setting $L_H(B_p)$ equal to the diameter d_w of the nanowire defines a critical magnetic field strength B_p, below which the wavefunction is confined by the nanowire boundary (the 1D regime), and above which the wavefunction is confined by the magnetic field (the 3D regime). The physical basis for this phenomenon is associated with confinement of a single magnetic flux quantum within the nanowire cross-section [96]. The peak of the dR/dB curve at 2 K in Fig. 4-17(a) occurs at $B_p \sim 0.3$ T, corresponding to $L_H \sim 47$ nm, very close to the nominal nanowire diameter of 40 nm. This phenomenon, though independent of temperature, is observed for $T < 5$ K, since the phase-breaking length has to be larger than the wire diameter.

It should be noted that the phenomenon associated with the 1D-3D localization is also observed in Sb nanowires [106] and Bi$_{1-x}$Sb$_x$ nanowires with different Sb contents
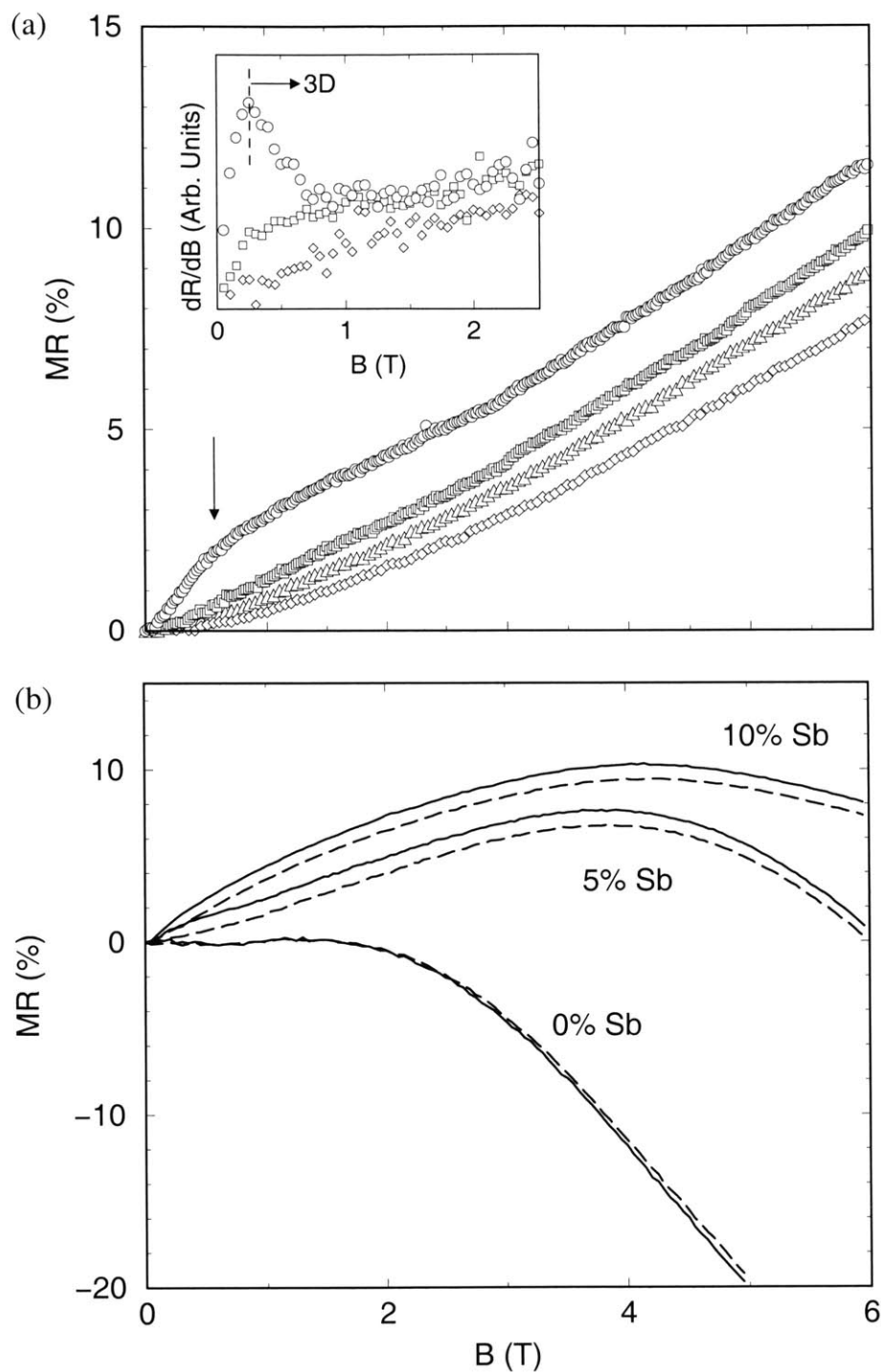
Figure 4-17: (a) Longitudinal MR of 40-nm $Bi_{0.85}Sb_{0.15}$ nanowires as a function of magnetic field at (○) 2 K, (□) 4 K, (△) 10 K, and (◇) 30 K. The inset shows the first derivative with respect to the magnetic field (dR/dB) of the longitudinal MR. (b) Longitudinal MR as a function of B for 65-nm $Bi_{1-x}Sb_x$ nanowires at 2 K (——) and 4 K (- - -).

with a good agreement between the measured B_p and the calculated values, suggesting that the 1D-3D localization phenomenon is a universal effect in nanowires. Furthermore, the transverse magnetoresistance measurements of these nanowire arrays, where the magnetic field is perpendicular to the wire axis, also exhibit the unusual feature as a function of magnetic field, and the measured critical field strength B_p is independent of the field orientation, as expected by the theory.

Figure 4-17(b) shows the measured MR as a function of magnetic field for $Bi_{1-x}Sb_x$ nanowires of a larger diameter ($d_w = 65$ nm). The 1D-3D transitional localization effect, although weaker than in the 40-nm wires, is observed at a lower B, consistent with theoretical expectations [96]. Other interesting features are the non-monotonic MR(B) behavior and the maximum observed in the longitudinal MR (e.g., at $B \sim 4$ T for $x \geq 0.05$), which is attributed to wire boundary scattering effects [110]. In the presence of a magnetic field, the trajectory of the mobile carriers is deflected, increasing the probability of wire boundary scattering at low B. However, as B increases beyond a critical field B_M, such that the cyclotron orbits of the carriers lie within the wires, the probability of wire boundary scattering will be reduced, resulting in a decrease in the MR. In Fig. 4-17(b), the field B_M for the maximum MR increases with increasing x due to the relative strengths of wire boundary scattering and impurity scattering for electrons. Since neutral impurity scattering makes a greater contribution to the transport in the alloy nanowires than in pure Bi nanowires, a greater field is needed to reduce the wire boundary scattering and observe a decreased MR. Our results show that the addition of Sb does not destroy the ballistic transport in pure Bi nanowires [110], and also confirms the long carrier mean free paths and the high crystalline quality in our $Bi_{1-x}Sb_x$ nanowires.

The magnetoresistance studies of Bi nanowires synthesized by electrochemical deposition have also been reported by several groups [33, 101, 108, 109]. Although these studies all showed an increasing magnetoresistance for Bi nanowires with increasing field strength, which is in qualitative agreement with our findings, the unusual 1D-3D localization effects and the boundary scattering effects mentioned above, however, were not reported in these other studies. Since the temperatures

94

employed in these studies are usually higher than $30\,K$ [33], it is expected that a much lower temperature ($< 5\,K$) will be required to observe the 1D-3D localization effect in nanowires. The absence of the MR maximum in these nanowires, a characteristic signature of boundary scattering effects, is believed to be due to a shorter carrier mean free path than the wire diameter, resulting from the small crystalline grain sizes for nanowires synthesized by the electrochemical deposition.

Chapter 5

Thermoelectric Properties of Superlattice Nanowires

5.1 Introduction

Studies on low-dimensional systems, such as 1D quantum wires and 2D superlattices, have attracted considerable attention for improved performance in various applications, such as optics [12, 13], microelectronics [113], thermoelectrics [11, 98, 114], and magnetics [17]. Due to the large surface-to-volume ratio for enhanced surface effects and quantum confinement effects, these nanostructured materials are expected to exhibit dramatically different behavior from their bulk counterparts.

Theoretical calculations and experimental investigation of thermoelectric properties of 1D and 2D systems have been studied extensively for various materials [79, 114, 115]. Since the enhancement in thermoelectric properties is anticipated to be more pronounced as dimensionality decreases, 0D structures hold even greater promise than 1D and 2D systems. However, unlike 1D or 2D systems, where at least one of the directions is not quantum-confined and thus can provide for electrical conduction, 0D structures, such as quantum dots, are confined in all directions and this may present difficulties for some applications.

To utilize the unique properties of quantum dots for situations where electron conduction is required, it is necessary to devise some means for carrier transport
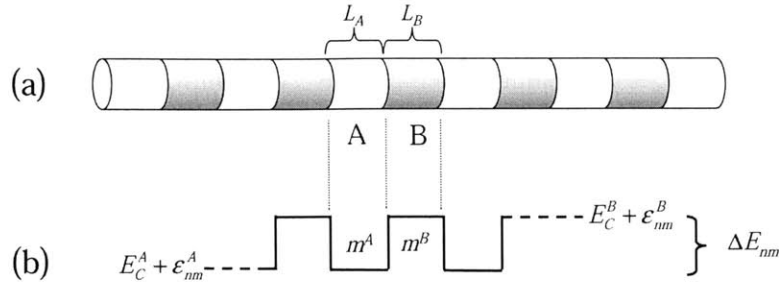
Figure 5-1: (a) Schematic diagram of a superlattice nanowire consisting of interlaced nanodots A and B. (b) Schematic potential profile of one conduction subband in a superlattice nanowire.

(e.g., tunneling or hopping) between individual dots. For this purpose, several novel structures based on quantum dots that capture the essence of 0D structures and enhance electronic transport have been proposed and synthesized, such as quantum dot array superlattices [11] and superlattice nanowires [28]. These new structures have shown great promise in the context of thermoelectricity, and Harman et $al.$ have measured an impressive thermoelectric performance of $ZT \sim 2$ at $300\,\mathrm{K}$ for PbTeSe-based quantum dot superlattices [11], compared to a highest ZT of ~ 1 for conventional bulk materials. A possible mechanism for this enhanced thermoelectric performance has been proposed to be due to the mini-band formation in coupled 3D quantum dot array structures [116]. Other nanostructures based on quantum dots that are of great interest for thermoelectricity are superlattice nanowires (SLNWs) (see Fig. 5-1(a)), which consist of a series of interlaced nanodots of two different materials (denoted by A and B). In the superlattice nanowire (SLNW) structure, the electronic transport along the wire axis is made possible by the tunneling between adjacent quantum dots, whereas the uniqueness of each quantum dot and its 0D characteristics are maintained by the energy difference of the conduction or valence bands between different materials (see Fig. 5-1(b)). The band offset not only provides some amount of quantum confinement, but also creates a periodic potential for carriers moving along the wire axis, which may result in a sharper density of electronic states

than is present in ordinary 1D systems. This new structure is especially attractive for thermoelectric applications because the heterogeneous interfaces between the nanodots can reduce the lattice thermal conductivity by blocking the phonon conduction along the wire axis [117], while electrical conduction may be sustained and benefit from the unusual electronic band structures due to the periodic potential perturbation. These 1D heterogeneous structures also hold great promise in other applications, such as nano-barcodes [118], nanolasers [119], 1D waveguides, and resonant tunneling diodes [120].

Various approaches have been developed to synthesize superlattice nanowire structures with different materials. Co/Cu superlattice nanowires were first fabricated in nanoporous templates using electrochemical deposition [28], and more recently, researchers have synthesized highly crystalline semiconductor superlattice nanowires (e.g., Si/SiGe [118], InP/InAs [119], and GaAs/GaP [121]) by the Vapor-Liquid-Solid growth mechanism. Due to the structural complexity and compositional diversity in these quantum dot-based systems, it is essential to develop a model to understand the behavior and to predict properties of interest for these novel structures, especially for practical applications and device optimization.

In this chapter, we present a general theoretical model for the electronic structure and transport properties of superlattice nanowires, which explicitly takes into account the cylindrical wire boundary conditions, the diameter-dependent band offsets for the periodic potential along the wire axis, and the multiple anisotropic carriers. The density of electronic states and the dispersion relations for each quantum subband in superlattice nanowires are presented in Section 5.2 using the Kronig-Penney model. With the electronic band structures thus obtained, a transport model based on the 1D Boltzmann transport equations is then developed. The effect of the superlattice structure on the phonon thermal conductivity, which is an important factor determining the thermoelectric performance, is also discussed. In Section 5.3, the established transport model is utilized to study the thermoelectric properties of superlattice nanowires made of various lead salts (e.g. PbS, PbSe, and PbTe) at 77 K, which is a temperature of interest for cryogenic cooling. The lead salts are chosen

for our model studies of superlattice nanowires because they are conventionally good thermoelectric materials with well-established transport properties. The thermoelectric properties of these lead salt superlattice nanowires, particularly PbS/PbSe, are investigated to elucidate their performance dependence on the segment length, wire diameter, crystal orientation along the wire axis, and the length ratio of the constituent nanodots.

5.2 Theoretical Model of Superlattice Nanowires

5.2.1 Electronic Band Structure

In superlattice nanowires, their transport and other electronic properties are determined by the electronic band structure, which exhibits dramatically different features from that of a simple 1D nanowire or bulk materials. To model the electronic band structure of superlattice nanowires, we assume that each segment has a circular cross-section with a uniform wire diameter d_w (see Fig. 5-1(a)), and the carriers in each cylindrical nanodot are confined by an infinite potential at the wire boundary (the cylindrical sidewall), which is a good approximation for nanowires embedded in a wide bandgap insulating matrix and for free-standing nanowires. We also assume that each nanodot consists of a sufficient number of atoms so that the effective mass theorem is valid to derive the local electronic properties of a nanodot from the band structure parameters of the bulk material.

For the following discussions, the z axis is chosen to be along the wire axis, and we first consider the electronic structure in one nanodot (material A for example). Due to the quantum confinement normal to the wire axis, quantized subbands are formed in the nanodot. The confined electrons are described by the wavefunction,

$$\psi_{nm}^A(x, y, z) = \phi_{nm}^A(x, y) \exp(ikz), \tag{5.1}$$

where the superscript A denotes the material type, $\phi_{nm}(x, y)$ is the quantized wave-

function normal to the wire axis that is classified by the quantum numbers (n, m), and k represents the electron wavevector along the wire axis (z axis). In Eq. (5.1), the wavefunction $\exp(ikz)$ emphasizes the unrestricted motion for electrons in the z direction within the nanodot. The energy corresponding to the electronic states of Eq. (5.1) is given by:

$$E^A_{nm}(k) = E^A_C + \epsilon^A_{nm} + \frac{\hbar^2 k^2}{2m^A_z} \tag{5.2}$$

where E^A_C is the energy of the conduction band edge for bulk material A, ϵ^A_{nm} is the quantization energy of the (n, m) subband, and m^A_z is the transport effective mass along the wire axis. We note that the quantization energy ϵ_{nm} and the corresponding wavefunction $\phi_{nm}(x, y)$ both depend on the geometry of the wire cross-section, the wire diameter, and the carrier effective masses. For cylindrical 1D wires with anisotropic carrier mass tensors, the approach to calculate the wavefunction ϕ_{nm} and the quantized energy ϵ_{nm} has been described in Section 3.2.1.

By arranging the two types of nanodots (A and B) into a superlattice nanowire (see Fig. 5-1(a)), the electrons in the (n, m) subband will experience a periodic square-well potential $U(z)$ with an energy barrier height,

$$\Delta E_{nm} = (E^B_C + \epsilon^B_{nm}) - (E^A_C + \epsilon^A_{nm}), \tag{5.3}$$

when traveling along the wire axis (see Fig. 5-1(b)). Although independent quantum dots possess discrete energy levels like those of atoms, superlattice nanowires exhibit 1D-like dispersion relations along the wire axis due to the wavefunction leakage across the finite barrier height ΔE_{nm} between quantum dots. The (sub)band offset energies ΔE_{nm} are usually different from that of bulk materials $(E^B_C - E^A_C)$ due to the different quantum confinement energy ϵ_{nm} for each type of quantum dot. ΔE_{nm} may also depend on the subband index (n, m) and the wire diameter d_w.

According to the Bloch theorem [122], the wavefunction $\eta(z)$ for electrons in a superlattice structure with a periodic potential $U(z)$ takes a different form from $\exp(ikz)$

and must satisfy the boundary condition,

$$\eta(z + L) = \exp(i\kappa z)\eta(z), \tag{5.4}$$

where κ is the 1D wavevector of electrons moving along the superlattice nanowire, and $L = L_A + L_B$ is the periodic length of the superlattice nanowire. It should be pointed out that κ in Eq. (5.4) describes the energy-momentum relation of the *entire* superlattice nanowire, while k in Eq. (5.1) is a property related to one nanodot only.

We note that while the electronic wavefunction in each nanodot is described by linear combinations of Eq. (5.1), the overall envelope wavefunction of electrons in the superlattice nanowire should be expressed as

$$\psi_{nm}(x, y, z) = \phi_{nm}(x, y)\eta(z). \tag{5.5}$$

The energy of electrons described by Eq. (5.5), which can be solved as a function of κ using the Kronig-Penney model, constitutes the important dispersion relation $E_{nm}(\kappa)$ of the (n, m) subband in the superlattice nanowire. For electrons with energies above the potential barrier $(E \geq E_C^B + \epsilon_{nm}^B)$, the corresponding wavevector κ is solved by

$$\cos(\kappa L) = \cos(k^A L_A)\cos(k^B L_B) - \frac{1}{2}\left(\frac{m_z^B k^A}{m_z^A k^B} + \frac{m_z^A k^B}{m_z^B k^A}\right)\sin(k^A L_A)\sin(k^B L_B). \tag{5.6}$$

For electrons with energies below the potential barrier $(E_C^A + \epsilon_{nm}^A \leq E < E_C^B + \epsilon_{nm}^B)$, the wavevector κ is determined by

$$\cos(\kappa L) = \cos(k^A L_A)\cosh(q^B L_B) - \frac{1}{2}\left(\frac{m_z^B k^A}{m_z^A q^B} - \frac{m_z^A q^B}{m_z^B k^A}\right)\sin(k^A L_A)\sinh(q^B L_B), \tag{5.7}$$

where

$$k^A = \sqrt{2m_z^A(E - E_C^A - \epsilon_{nm}^A)}/\hbar$$
$$k^B = \sqrt{2m_z^B(E - E_C^B - \epsilon_{nm}^B)}/\hbar \tag{5.8}$$
$$q^A = \sqrt{2m_z^B(E_C^B + \epsilon_{nm}^B - E)}/\hbar.$$

The density of states $D_{nm}(E)$ of the (n, m) subband is related to the energy dispersion

relation by

$$D_{nm}(E) = \frac{\pi}{2} \left(\frac{\partial E_{nm}}{\partial \kappa} \right)^{-1}. \tag{5.9}$$

We note that, due to the periodic potential perturbation, the density of states $D_{nm}(E)$ in a superlattice nanowire may possess a very different energy dependence from that of a simple nanowire (see Eq. (5.2)). The electronic band structure ($E_{nm}(\kappa)$ and $D_{nm}(E)$) of one subband is highly dependent on the segment length (L_A or L_B), potential barrier height (V_b), and transport effective masses (m_z^A and m_z^B).

Figure 5-2 shows the density of states function $D(E)$ and the number of states ($N(E) \equiv \int D(E)dE$) calculated for a subband with various segment lengths ($L_A = L_B = 1$, 5, 20, and 60 nm), assuming a potential barrier height of $V_b = 50\,\mathrm{meV}$ and an effective mass of $m_z^A = m_z^B = 0.5\,m_0$, where m_0 is the free electron mass. The zero in energy is chosen to be at the top of the potential barrier. It is found in Fig. 5-2(a) that for very short superlattice periods ($L_A = 1\,\mathrm{nm}$), the electronic band structure approaches that of an alloy system (alloy limit) with a density of states similar to that of a simple 1D system (see Fig. 5-2(a)). In this limit, the onset of the density of states corresponds to an effective band edge in the middle of the potential well, and this effective band edge is equal to the average of the periodic potential (see Fig. 5-2(a)). As the segment length increases, the density of states (or the number of states) begins to develop mini-bands and mini-band gaps in the subband structure (see Figs. 5-2(b) and (c)), exhibiting features unique to the superlattice nanowires. The widths of these mini-bands are usually very narrow ($\sim 1\,\mathrm{meV}$ for the first mini-band in Fig. 5-2(b)) for energies in the potential well ($E < 0$), yielding a δ function-like density of states similar to that of the discrete states of quantum dots, as approximated by vertical lines in Figs. 5-2(b) and (c). As the energy increases, the widths of these mini-bands usually become larger and the mini-band gaps become narrower. We also note that the number of these narrow mini-bands in the potential well increases with increasing segment length (see Fig. 5-2(c)); and for long segment lengths ($L_A \geq 60\,\mathrm{nm}$), these mini-bands become so close to each other in energy that they may be approximated by a continuum, if the mini-band gaps are
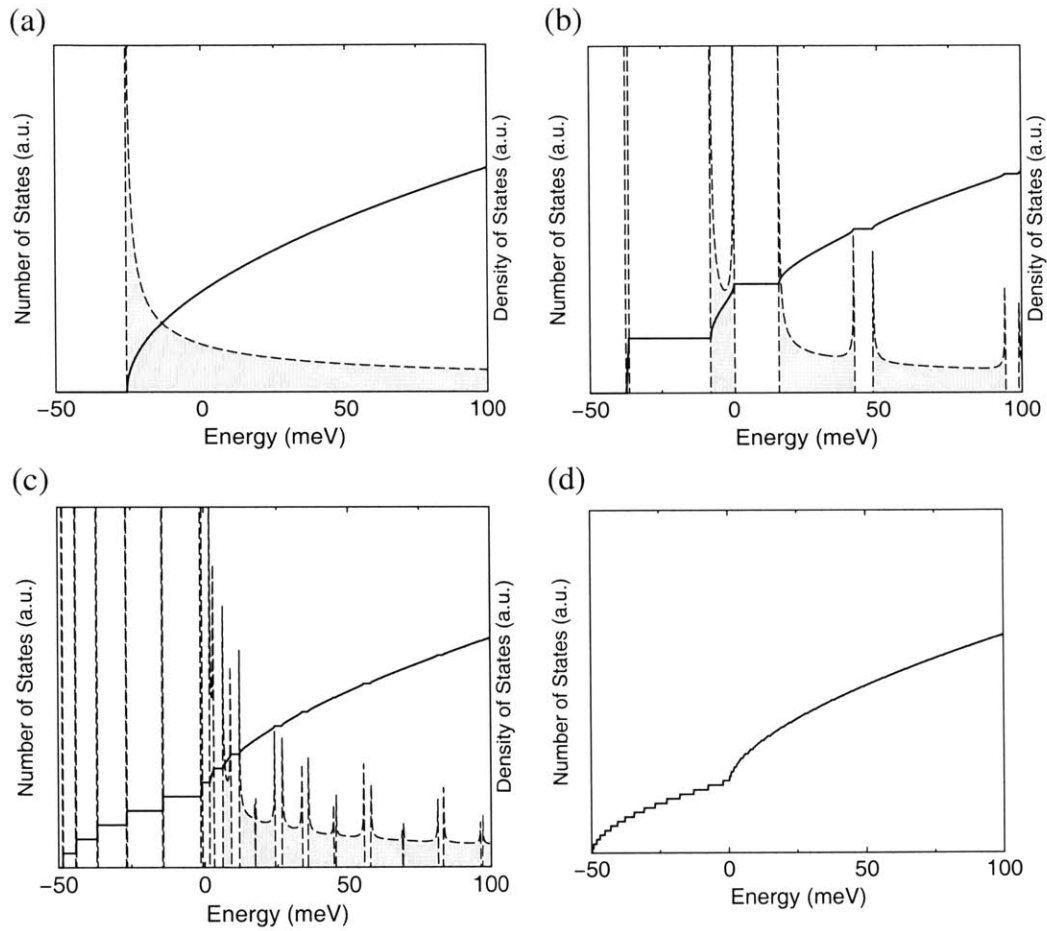
Figure 5-2: Calculated density of states (- - -) and the number of states (—) of a 1D subband in a periodic potential with segment lengths $L_A = L_B$ of (a) 1 nm, (b) 5 nm, (c) 20 nm, and (d) 60 nm, assuming a potential barrier height of 50 meV and effective masses of 0.5 m_0. The zero in energy is chosen to be at the top of the potential barrier.

much smaller than the thermal energy (see Fig. 5-2(d)). In this long segment length limit, the density of states of the superlattice nanowire is approximately equivalent to the averaged density of states of the two constituent materials (classical limit). In the following, we define the *alloy* and *classical* limits for superlattice nanowires that have very short and very long periods with the electronic subband structures shown in Figs. 5-2(a) and (d), respectively. It is also worth noting that in Fig. 5-2(c), while the mini-bands are well-separated in energy for states with energies in the potential well ($E \leq 0$), the band structure approximates the continuum of the classical limit for electrons with energies above the potential barrier ($E > 0$).

These dramatically different electronic band structures of superlattice nanowires shown in Figs. 5-2 can be qualitatively categorized based on different length and energy scales: the electron de Broglie wavelength (Λ_e), the segment length (L_A or L_B), the mini-band gap energy (ϵ_g), and the thermal energy ($k_B T$). In the potential well region (e.g., in the nanodot made of material A in Fig. 5-1(b)), the energy separation between two mini-bands is on the order of $\epsilon_g \sim (\pi\hbar/L)\sqrt{V_b/2m_z^A}$, and the wavelength of electrons with energy near the potential barrier is approximately $\Lambda_e \sim 2\pi\hbar/\sqrt{2m_z^A V_b}$. When the segment length is much shorter than the de Broglie wavelength Λ_e, a full electronic wavelength would cover many superlattice periods (see Fig. 5-3(a)), so the electrons only experience an averaged potential without noticing the detailed potential structure as they travel along the nanowire (alloy limit). On the other hand, if the thermal energy $k_B T$ is much larger than the mini-band gaps ϵ_g (see Fig. 5-3(b)), the mini-bands can be treated as continuous states due to the thermal smearing (classical limit). We define two dimensionless quantities,

$$\zeta \equiv \frac{L/2}{\Lambda_e} = \frac{L\sqrt{2m_z V_b}}{4\pi\hbar} \tag{5.10}$$

and

$$\eta \equiv \frac{\epsilon_g}{k_B T} = \frac{\pi\hbar}{k_B T L}\sqrt{\frac{V_b}{2m_z}}, \tag{5.11}$$

for the determination of subband structure. The criteria for the alloy limit is then given by $L \ll \Lambda_e$ (see Fig. 5-3(a)), or $\zeta \ll 1$, while the condition for the classical limit

104
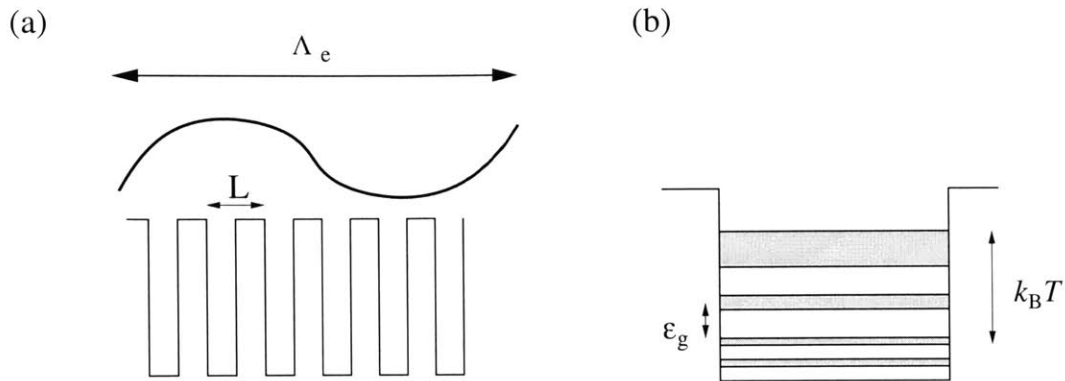
Figure 5-3: Schematic diagrams illustrating the conditions for superlattice nanowires in the (a) alloy limit and (b) classical limit. In the alloy limit, the period L is much shorter than the de Broglie wavelength Λ_e, and a full electronic wavelength would cover many superlattice periods. In the classical limit, the thermal energy $k_B T$ is much larger than the mini-band gaps ϵ_g, and the mini-bands can be treated as continuous states due to the thermal smearing.

Table 5.1: Calculated ζ and η for various segment lengths at 77 K, assuming a potential barrier of 50 meV and an effective mass of $0.5 m_0$.

Segment length ($L/2$)	1 nm (alloy limit)	5 nm	20 nm	60 nm (classical limit)
ζ	0.13	0.64	2.57	7.73
η	9.69	1.93	0.47	0.16

is $\epsilon_g \ll k_B T$ (see Fig. 5-3(b)), or $\eta \ll 1$. Table 5.1 lists the calculated values of ζ and η corresponding to the parameters used in Fig. 5-2 at $T = 77\,K$. We note that ζ is calculated to be 0.13 for $L_A = 1$ nm (Fig. 5-2(a)), and η is 0.16 for a segment length of 60 nm (Fig. 5-2(d)), indicating that $\zeta \lesssim 0.1$ and $\eta \lesssim 0.1$ are satisfactory criteria for identifying the alloy and classical limits, respectively, for the subband structures of superlattice nanowires. For superlattice nanowires with unequal segment lengths, it is found that these conditions for ζ and η for determining the alloy and classical limits still hold for $0.1 < L_A/L_B < 10$.

5.2.2   Electrical Transport Properties

With the dispersion relation $E_{nm}(\kappa)$ of each subband thus obtained, important transport properties can be derived based on the Boltzmann transport equations for 1D systems [79]. For simplicity, we use the constant relaxation time approximation to calculate the following fundamental integrals for the conduction band

$$K_{e,\alpha} = \frac{4\tau_e}{\pi^2\hbar^2 d_w^2} \sum_{n,m} \int \frac{(E - E_F)^\alpha}{D_{nm}(E)} \left(-\frac{df}{dE}\right) dE, \tag{5.12}$$

where $\alpha = 0, 1$ or 2, τ_e is the relaxation time for electrons, E_F is the Fermi energy, $f(E)$ is the Fermi-Dirac distribution function, and the summation is over all subbands for all electron pockets. A similar expression for holes is given by

$$K_{h,\alpha} = \frac{4\tau_h}{\pi^2\hbar^2 d_w^2} \sum_{n,m} \int \frac{(E_F - E)^\alpha}{D_{nm}(E)} \left(-\frac{df}{dE}\right) dE. \tag{5.13}$$

The electrical conductivity σ, Seebeck coefficient S, and electrical contribution to the thermal conductivity λ_e are then obtained from K_α by

$$\sigma = e^2(K_{e,0} + K_{h,0}) \tag{5.14}$$

$$S = -\frac{1}{eT}\frac{K_{e,1} - K_{h,1}}{K_{e,0} + K_{h,0}} \tag{5.15}$$

$$\lambda_e = \frac{1}{T}\left(K_{e,2} + K_{h,2} - \frac{(K_{e,1} - K_{h,1})^2}{K_{e,0} + K_{h,0}}\right). \tag{5.16}$$

Since there is no general analytical expression for the density of states $D(E)$ of superlattice nanowires, the calculation of the integrals in Eqs. (5.12) and (5.13) usually requires considerable amount of computing resource. However, for subbands in the alloy or classical limit, the computational task can be greatly simplified by adopting analytical expressions for $D(E)$ for these two limiting conditions.

106

5.2.3 Lattice Thermal Conductivity

The phonon transport in superlattice nanowires is influenced by additional phonon scattering at the wire boundary and at the interfaces between the quantum dots. It is expected that the lattice thermal conductivity should be significantly reduced as the wire diameter or the segment length becomes smaller than the bulk phonon mean free path. The lattice thermal conductivity for superlattice nanowires has been modeled, based on the phonon Boltzmann transport equations with diffuse mismatch interface conditions [117]. Assuming a diffuse nanowire boundary for phonons, which is a good approximation for nanowires with rough or imperfect surfaces, the phonon thermal conductivity λ_{SL} of superlattice nanowires is given by [117, 123]

$$
\frac{L}{\lambda_{SL}} = \frac{L_A}{\lambda_A} + \frac{L_B}{\lambda_B} + 4 \left(\frac{1}{C_A v_A t_{AB}} + \frac{1}{C_B v_B t_{BA}} \right) \left(1 - \frac{t_{AB} + t_{BA}}{2} \right)
$$
$$
+ \frac{3}{d_w} \left(\frac{L_A}{C_A v_A \alpha_A} + \frac{L_B}{C_B v_B \alpha_B} \right), \tag{5.17}
$$

where λ, C, and v are the lattice thermal conductivity, heat capacity per unit volume, and sound velocity of the bulk material (A or B), respectively. t_{AB} (or t_{BA}) is the phonon transmissivity from nanodot A to nanodot B (or B to A), which is defined as the probability of phonon energy transfer through the A-B (or B-A) interface. α_A (or α_B) is a geometric factor that only depends on the aspect ratio L_A/d_w (or L_B/d_w) of the nanodots, varying between 0.75 and 1 for cylindrical wires [117]. Fig. 5-4 shows the calculated α_A (or α_B) as a function of L_A/d_w (or L_B/d_w), showing that for $L_A \ll d_w$, this geometric factor α_A approximates 0.75, whereas for $L_A \gg d_w$, α_A rapidly converges to 1.

In Eq. (5.17), the contributions of the segment interface and the wire boundary scattering processes to the lattice thermal resistivity are contained in the third and fourth terms, respectively, and the first two terms in Eq. (5.17) account for intrinsic phonon scattering events present in bulk materials. Using the diffuse mismatch
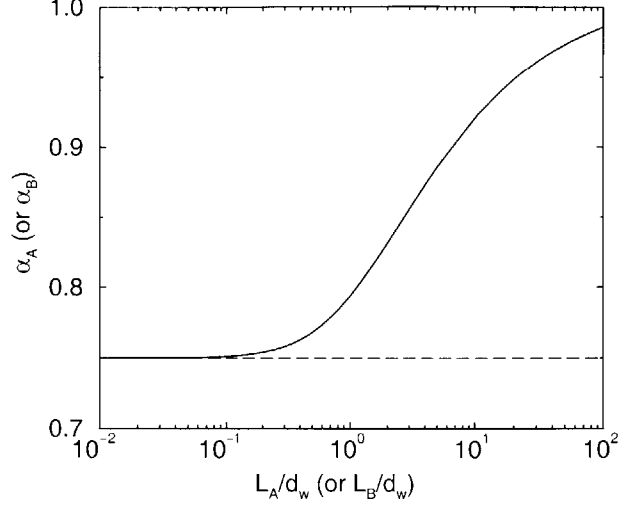
Figure 5-4: Calculated geometric factor α_A (or α_B) as a function of L_A/d_w (or L_B/d_w), showing that for $L_A \ll d_w$, the geometric factor α_A approximates 0.75, whereas for $L_A \gg d_w$, α_A rapidly converges to 1.

model [123, 124] approximation for segment interfaces, t_{AB} is given by

$$t_{AB} = \frac{C_B v_B}{C_A v_A + C_B v_B},\tag{5.18}$$

and $t_{BA} = 1 - t_{AB}$. Eq. (5.17) can then be rearranged as

$$\frac{L}{\lambda_{SL}} = \frac{L_A}{\lambda_A}\left(1 + \frac{4}{3}\frac{\Lambda_A}{L_A} + \frac{\Lambda_A}{\alpha_A d_w}\right) + \frac{L_B}{\lambda_B}\left(1 + \frac{4}{3}\frac{\Lambda_B}{L_B} + \frac{\Lambda_B}{\alpha_B d_w}\right),\tag{5.19}$$

where Λ_A and Λ_B are the phonon mean free paths of bulk materials A and B, respectively, which are derived from kinetic theory

$$\lambda = \frac{1}{3}Cv\Lambda.\tag{5.20}$$

It is convenient to define an effective phonon mean free path Λ_{eff} for one segment (A for example) in the superlattice nanowire by

$$\Lambda_{A,\text{eff}}^{-1} = \Lambda_A^{-1} + \frac{4}{3}L_A^{-1} + \frac{1}{\alpha_A}d_w^{-1},\tag{5.21}$$

108

and the corresponding effective thermal conductivity λ_{eff} in each segment by

$$\lambda_{\text{A,eff}} = (\Lambda_{\text{A,eff}}/\Lambda_A)\lambda_A, \qquad (5.22)$$

which implies effective phonon scattering lengths of $3L_A/4$ and $\alpha_A d_w$ for interface and wire boundary scattering, respectively. The lattice thermal conductivity λ_{SL} can then be concisely expressed in terms of a series of two nanodots (A and B) with effective thermal conductivities $\lambda_{\text{A,eff}}$ and $\lambda_{\text{B,eff}}$ by

$$\frac{L}{\lambda_{SL}} = \frac{L_A}{\lambda_{\text{A,eff}}} + \frac{L_B}{\lambda_{\text{B,eff}}}. \qquad (5.23)$$

It should be noted that the derivation of Eq. (5.17) assumes a linear phonon dispersion relation with a constant sound velocity, which is only valid for temperatures much lower than the Debye temperature. A more accurate description for the lattice thermal conductivity of superlattice nanowires that takes into account a nonlinear phonon dispersion relation at higher phonon frequencies can be obtained by replacing the product of the heat capacity and the sound velocity Cv in Eqs. (5.17)–(5.20) with the integration of $C(\omega)v(\omega)$ with respect to the phonon frequency ω, $\int C(\omega)v(\omega)d\omega$ [117]. To further improve the model for the thermal conductivity of superlattice nanowires, the interface condition for the phonon transport should also be considered, as discussed in Refs. [117, 125].

5.3   Lead Salt Superlattice Nanowires

In this section, we apply the electronic band model and transport equations developed in Section 5.2 to investigate the thermoelectric properties of superlattice nanowires composed of lead salts (PbTe, PbSe, and PbS). Lead salts and their alloys are narrow-gap semiconductors that have been widely studied. They have well-established electronic properties because of their potential for tunable photoelectronic devices in the infrared and visible range [126]. Lead salts have been found to be promising ther-

moelectric materials, going back to the early stage in thermoelectrics research, and PbS and PbTe were used in the first thermoelectric generators and cooling units, respectively [4]. Recently, a thermoelectric performance twice as high as the best conventional thermoelectric material has been demonstrated by lead salt quantum dot arrays [11], suggesting that superlattice nanowires consisting of lead salt quantum dots may also be promising thermoelectric materials.

5.3.1 Electronic Band Structure

The lead chalcogenide family (PbTe, PbSe, and PbS) constitutes an attractive model system to study the effect of the superlattice structure on the transport properties of nanowires because of its simple crystal and electronic structures with well-known properties over a wide temperature range. The lead salts all possess the same NaCl-like face-centered cubic structure with lattice constants $a_0 = 5.94$ Å, 6.12 Å, and 6.46 Å for PbS, PbSe, and PbTe, respectively [127], and they all have similar direct-gap semiconductor band structures. The constant energy surfaces for the conduction and valence bands of these lead salts are prolate ellipsoids of revolution centered at the four equivalent L points in the Brillouin zone, and the major axes of these ellipsoids are in the [111] directions [127], as shown in Fig. 5-5. On the other hand, there is a considerable band offset when combining two dissimilar lead salts together, and this band offset provides carrier confinement between quantum dots. The band structure of lead salts in the bulk form have been studied extensively, and some of the important temperature-dependent parameters related to their transport properties are listed in Table 5.2. To minimize the lattice mismatch at the heterogeneous interfaces, we choose to study PbS/PbSe and PbSe/PbTe superlattice nanowires, with particular emphasis on the PbS/PbSe system. We note that the lattice mismatch may not be as significant an issue in superlattice nanowires as in superlattice thin films, since researchers have found that in superlattice nanowires, the lattice strain can be laterally relaxed to avoid defects at the interface [121].

Based on the band structure parameters in Table 5.2, we first calculate the quan-

110
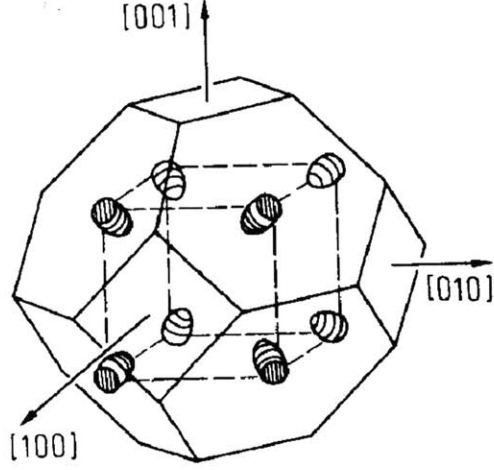
Figure 5-5: The Brillouin zone of lead salts, showing the constant energy surfaces of the four L-point carrier pockets.

Table 5.2: The direct bandgap E_g (in units of meV) and the effective mass components of the L-point electron and hole pockets for bulk PbS, PbSe, and PbTe, and their temperature dependence [126].

	PbS	PbSe	PbTe
$E_g(T)$	$263+$ $\sqrt{400 + 0.256T^2}$	$125+$ $\sqrt{400 + 0.256T^2}$	$171.5+$ $\sqrt{(12.8)^2 + 0.19(T + 20)^2}$
$m_{e\perp}/m_0$	$\left(10.6\frac{E_g(0)}{E_g(T)} + 1.9\right)^{-1}$	$\left(20.7\frac{E_g(0)}{E_g(T)} + 4.3\right)^{-1}$	$\left(30.58\frac{E_g(0)}{E_g(T)} + 14.29\right)^{-1}$
$m_{e\|}/m_0$	$\left(5.8\frac{E_g(0)}{E_g(T)} + 3.7\right)^{-1}$	$\left(11.4\frac{E_g(0)}{E_g(T)} + 2.9\right)^{-1}$	$\left(2.98\frac{E_g(0)}{E_g(T)} + 2.42\right)^{-1}$
$m_{h\perp}/m_0$	$\left(10.6\frac{E_g(0)}{E_g(T)} + 2.7\right)^{-1}$	$\left(20.7\frac{E_g(0)}{E_g(T)} + 8.7\right)^{-1}$	$\left(30.58\frac{E_g(0)}{E_g(T)} + 10.0\right)^{-1}$
$m_{h\|}/m_0$	$\left(5.8\frac{E_g(0)}{E_g(T)} + 3.7\right)^{-1}$	$\left(11.4\frac{E_g(0)}{E_g(T)} + 3.3\right)^{-1}$	$\left(2.98\frac{E_g(0)}{E_g(T)} + 1.25\right)^{-1}$

tized subband energy ϵ_{nm} related to the confinement of the wire boundary in the x-y directions and the transport effective masses m_z along the wire axis. Since the carrier pockets of these lead salts are highly anisotropic, ϵ_{nm} and m_z are dependent on the crystallographic direction of the wire axis. For wires oriented along the [001] direction, the four L pockets are all degenerate and are denoted as $L^{(4)}$. For wires oriented along the [111] direction, this four-fold degeneracy is lifted, resulting in two inequivalent groups of carrier pockets: a single pocket with its major axis along the wire axis (denoted as $L^{(1)}$), and the other three pockets that are still degenerate (denoted as $L^{(3)}$). The subband energy ϵ_{nm}, which is inversely proportional to d_w^2, is calculated for the three lead salts at 77 K for two wire orientations ([001] and [111]), and the results are listed in Tables 5.3 and 5.4 for the first five subbands for the electrons and holes, respectively. The transport effective masses along the wire axis for the various lead salts and orientations are given in Table 5.5. We note that since the $L^{(1)}$ carriers of these lead salts usually have their largest mass component along the wire axis and their smallest mass components in the quantum confined directions, they possess a larger subband energy and a heavier transport effective mass along the wire axis compared to the other pockets.

The subband energy and the transport effective masses in each segment are the fundamental parameters in determining the subband offset (see Eq. (5.3)) and the subband dispersion relation $E_{nm}(\kappa)$ of the superlattice nanowires. Assuming an equal *bulk* band offset for the conduction and valence bands in a heterogeneous structure constructed from two lead salts and choosing the zero energy to be at the middle of the bulk bandgap, the (n, m) subband edge energy of a segment made of material X (PbS, PbSe, or PbTe) is given by

$$E_{nm}^X = \pm \left(\frac{E_g^X}{2} + \frac{\chi_{nm}^X}{d_w^2} \right) \tag{5.24}$$

for electrons (+) and holes (−), where $\chi_{nm} = \epsilon_{nm} \cdot d_w^2$ is a diameter-independent parameter as those given in Tables 5.3 and 5.4.

It should be noted that the potential barrier and well regions of a *bulk* hetero-

Table 5.3: The first five subband energies ($\chi_{nm} \equiv \epsilon_{nm}d_w^2$) normalized to the wire diameter d_w and given in units of eV·nm² for each distinct electron pocket in various lead salts and wire orientations at 77 K.

material	orientation	pocket	order: 1	2	3	4	5
PbS	[001]	$L_e^{(4)}$	9.52	23.17	25.14	42.49	43.48
	[111]	$L_e^{(1)}$	10.30	26.12	26.12	46.92	46.92
	[111]	$L_e^{(3)}$	9.26	22.19	24.80	40.69	42.19
PbSe	[001]	$L_e^{(4)}$	16.70	38.85	45.85	70.90	75.99
	[111]	$L_e^{(1)}$	19.47	49.40	49.40	88.72	88.72
	[111]	$L_e^{(3)}$	15.77	25.31	44.63	63.70	71.65
PbTe	[001]	$L_e^{(4)}$	25.32	50.79	77.38	87.37	114.35
	[111]	$L_e^{(1)}$	35.98	91.27	91.27	163.94	163.94
	[111]	$L_e^{(3)}$	21.61	36.85	57.79	72.11	84.65

Table 5.4: The first five subband energies ($\chi_{nm} \equiv \epsilon_{nm}d_w^2$) normalized to the wire diameter d_w and given in units of eV·nm² for each distinct hole pocket in various lead salts and wire orientations at 77 K.

material	orientation	pocket	order: 1	2	3	4	5
PbS	[001]	$L_h^{(4)}$	9.99	24.07	26.62	44.14	45.51
	[111]	$L_h^{(1)}$	11.00	27.91	27.91	50.13	50.13
	[111]	$L_h^{(3)}$	9.65	22.78	26.19	41.70	43.95
PbSe	[001]	$L_h^{(4)}$	19.39	44.18	54.16	80.17	88.19
	[111]	$L_h^{(1)}$	23.35	59.24	59.24	106.40	106.40
	[111]	$L_h^{(3)}$	18.06	39.12	52.41	69.69	81.95
PbTe	[001]	$L_h^{(4)}$	22.46	44.71	68.97	76.61	101.39
	[111]	$L_h^{(1)}$	32.19	81.68	81.68	146.70	146.70
	[111]	$L_h^{(3)}$	19.06	31.94	49.54	64.11	72.03

Table 5.5: Calculated transport effective masses along the wire axis for each carrier pocket in various lead salts with different wire orientations. All effective mass coefficients are normalized to the free electron mass.

Material	[100] direction		[111] direction			
	$m_{e,z}^{(4)}$	$m_{h,z}^{(4)}$	$m_{e,z}^{(1)}$	$m_{e,z}^{(3)}$	$m_{h,z}^{(1)}$	$m_{h,z}^{(3)}$
PbS	0.0939	0.0903	0.1105	0.0884	0.1105	0.0835
PbSe	0.0564	0.0506	0.0788	0.0490	0.0764	0.0421
PbTe	0.0829	0.1051	0.2000	0.0440	0.2607	0.0533

geneous structure may be inverted in a superlattice nanowire due to this diameter-dependent subband energy ϵ_{nm}. For example, Fig. 5-6 shows the first subband edge energies of PbS, PbSe, and PbTe nanodots oriented in the [001] direction as a function of wire diameter at 77 K. In the bulk form, the bandgap (E_g) relation of the three lead salts is PbSe $<$ PbTe $<$ PbS, and hence PbSe constitutes the potential well region for electrons in the PbSe/PbS or PbSe/PbTe heterostructures, as depicted by the upper-right inset in Fig. 5-6. However, as the wire diameter decreases, the subband edge energy of PbS nanodots increases at a slower rate than that of PbSe or PbTe nanodots because of the heavier carrier effective masses in PbS, and the first subband energy of PbS nanodots crosses that of PbTe and PbSe at $d_w \sim 18\,\mathrm{nm}$ and 10 nm, respectively. The insets in Fig. 5-6 sketch the relative energy levels of the first subband edge of these lead salts in three different diameter ranges, showing that for small-diameter superlattice nanowires (e.g., PbSe/PbS), some of the subbands in the nanowire may undergo a potential barrier-well inversion when the subband edge energies of PbS nanodots become lower than those of the corresponding PbSe subbands. Due to the carrier anisotropy of these lead salts, the critical wire diameter for the potential barrier-well inversion is also dependent on the crystallographic direction, and for the [111] orientation, the lowest lying $L_e^{(3)}$ conduction subband of PbS nanodots crosses those of PbSe and PbTe at $d_w \sim 16\,\mathrm{nm}$ and 10 nm, respectively. This subband edge crossing and barrier-well inversion induced by quantum confinement, which is absent in other systems, such as 2D superlattice thin films, are unique properties of superlattice nanowires, and they hold important implications for carrier
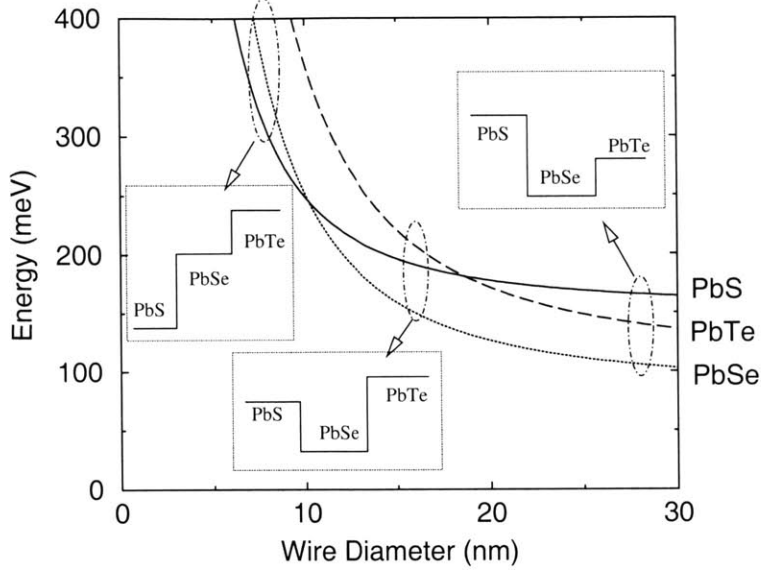
Figure 5-6: The subband energy of various lead salt nanodots oriented in the [001] direction at $77\,\mathrm{K}$, showing the first subband energy as a function of wire diameter. The zero energy refers to the middle of the bulk band gap. As d_w decreases, the subbands moves up in energy, and the PbS subband (—) crosses those of PbTe (- - -) and PbSe ($\cdots$) at $d_w \sim 18\,\mathrm{nm}$ and $10\,\mathrm{nm}$, respectively. The three insets depict the relation of subband edge energies of the three lead salts at different diameter ranges.

transport phenomena. We note that since the band offset vanishes at the crossing of corresponding subbands of two materials, the carriers in that subband may travel along the wire like free carriers without the potential barrier, which may be desirable for certain transport-related applications. Since the theoretical formalism developed for superlattice nanowires in Section 5.2 treats the potential well A and barrier B symmetrically, the effect of this potential barrier-well inversion can be readily addressed in the following model calculations for lead salt superlattice nanowires. It is also interesting to compare this potential-well inversion in superlattice nanowires to the semimetal-semiconductor transition observed in Bi nanowires [79], which results from the subband crossing due to a diameter-dependent phase diagram.

Figure 5-7 shows the calculated density of states of the conduction band for [001] PbSe/PbS superlattice nanowires as a function of energy at $77\,\mathrm{K}$ with a wire diameter of $d_w = 10\,\mathrm{nm}$ and equal segment lengths $L_{\mathrm{PbSe}} = L_{\mathrm{PbS}} = 5\,\mathrm{nm}$. The density of states of $\mathrm{PbS_{0.5}Se_{0.5}}$ nanowires with the same diameter and orientation is also plot-

115
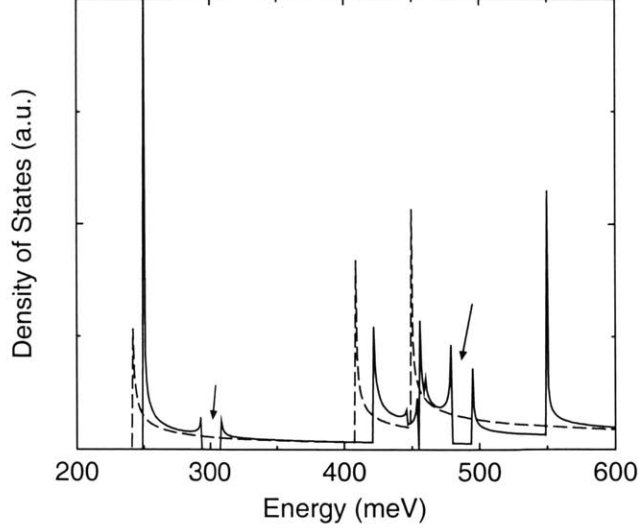
Figure 5-7: Calculated density of states for [001] PbSe/PbS superlattice nanowires (—) with wire diameter $d_w = 10\,\mathrm{nm}$ and segment lengths $L_{\mathrm{PbSe}} = L_{\mathrm{PbS}} = 5\,\mathrm{nm}$ at 77 K. The arrows indicate the mini-band gaps resulting from the periodic potential in the superlattice nanowires. Due to the superposition of multiple subbands, the mini-band gap indicated by the second arrow at $E \sim 490\,\mathrm{meV}$ has a non-vanishing density of states. The calculated density of states for $\mathrm{PbS_{0.5}Se_{0.5}}$ nanowires (- - -) with the same wire diameter and orientation is also shown for comparison.

ted in Fig. 5-7 for comparison. We note that for alloy nanowires, the singularities in the electronic density of states correspond to individual 1D subband edges ϵ_{nm}, and for each subband the density of states varies as $(E - \epsilon_{nm})^{-1/2}$. In contrast, the density of states for superlattice nanowires usually exhibits a more complicated energy dependence with additional singularities resulting from the mini-band gaps, as indicated by the arrows in Fig. 5-7. The superposition of multiple subbands further enriches the behavior of the density of states in superlattice nanowires, as shown at $E \sim 450\,\mathrm{meV}$. It should also be pointed out that the density of states profile of these lead salt superlattice nanowires is highly sensitive to the crystal orientation because of their multiple anisotropic carrier pockets. These interesting features in the dispersion relation along the transport direction, which are absent in both simple nanowires and 2D superlattice systems, are unique to superlattice nanowires. They are responsible for unusual transport properties predicted in the superlattice nanowires, as will be discussed in the next section.

116

5.3.2 Transport and Thermoelectric Properties

In this section, we calculate transport properties of superlattice nanowires composed of various lead salts, and we investigate their potential for thermoelectric applications, based on the electronic band structure model and the transport equations developed in previous sections.

Figure 5-8 shows the calculated Seebeck coefficient and electrical conductivity as a function of Fermi energy for [001] PbSe/PbS superlattice nanowires with a diameter $d_w = 10\,\mathrm{nm}$ and segment lengths $L_{\mathrm{PbS}} = L_{\mathrm{PbSe}} = 5\,\mathrm{nm}$ at 77 K, as well as the calculated results for $PbS_{0.5}Se_{0.5}$ nanowires with the same diameter and crystal orientation. The relaxation times τ of electrons and holes, required for calculating various transport-related integrals (Eqs. (5.12) and (5.13)), are derived from the carrier mobility of bulk materials [128] using the relation $\mu = e\tau/m^*$, as listed in Table 5.6 for various lead salts at 77 K. However, we note that the carrier mobility of low-dimensional systems may possess different values from those of their bulk counterparts. It is expected that μ may be lowered in nanostructures due to the extra scattering at the wire boundary and the heterogeneous interfaces, whereas the reduction in available final states for scattering events in low-dimensional systems may increase μ. Therefore, careful experimental studies are required to obtain a more accurate estimate for μ and to further improve model calculations.

As shown in Fig. 5-8, the electrical conductivity of a homogeneous (alloy) nanowire increases monotonically with increasing Fermi energy (or electron density), while that for the superlattice nanowires exhibits non-monotonic variations with local minima corresponding to the mini-band gaps in the density of states (see Fig. 5-7). In Fig. 5-8, the Seebeck coefficient of superlattice nanowires also shows unusual behaviors due to the existence of the mini-band gaps. We note that for alloy nanowires, the Seebeck coefficient is always negative and the magnitude diminishes rapidly with increasing Fermi energy, except for some small fluctuations near the subband edges. Interestingly, for superlattice nanowires, the Seebeck coefficient not only shows strong oscillations near the mini-band gaps, but also becomes positive at certain energy ranges.
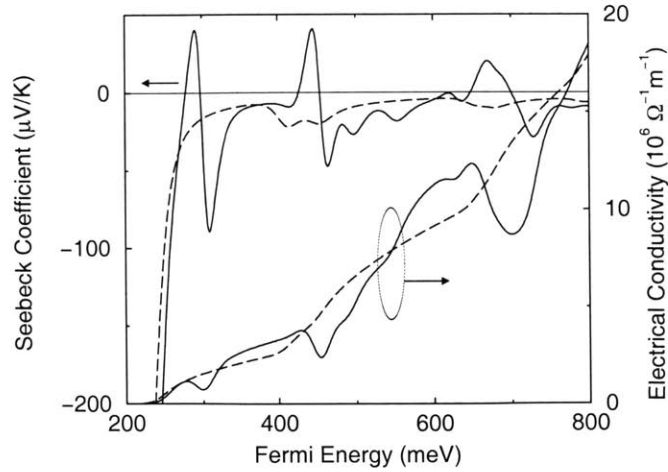
Figure 5-8: Calculated Seebeck coefficient and electrical conductivity as a function of Fermi energy for [001] PbSe(5 nm)/PbS(5 nm) superlattice nanowires (—) and PbS$_{0.5}$Se$_{0.5}$ nanowires (- - -) at 77 K. The wire diameters are $d_w = 10$ nm for both types of nanowires.

This sign change in the Seebeck coefficient as the Fermi energy varies has important implications, indicating that the superlattice nanowires may be tailored to exhibit n- or p-type properties, using the same dopants (e.g., electron donors) by carefully controlling the Fermi energy or the dopant concentration. More importantly, we also note that the Seebeck coefficient extrema of superlattice nanowires have substantially larger magnitudes for Fermi energies near the mini-band gaps, while the corresponding electrical conductivity is only slightly reduced compared to the alloy nanowires (see Fig. 5-8). This phenomenon is a direct consequence of the unique potential profile for superlattice nanowires in the transport direction. A similar behavior of enhanced Seebeck coefficient due to mini-band formation has also been predicted by Balandin and coworkers for 3D quantum dot array structures [116], illustrating the impact of the periodic potential perturbation on transport properties. These observations are significant because they not only illustrate one of the advantages of superlattice nanowires for thermoelectric applications, but also account for the enhanced Seebeck coefficient and power factor ($S^2\sigma$) measured in quantum dot array systems and reported by Harman et $al.$ [11] since their systems have a similar periodic potential profile in the direction of carrier transport.

Table 5.6: Mobility of electrons and holes for various lead salts at 77 K [128]. The carrier relaxation time is derived using the relation $\tau = m\mu/e$.

Property	PbS	PbSe	PbTe
μ_e (cm^{2}V^{-1}s^{-1})	11000	16500	31600
μ_h (cm^{2}V^{-1}s^{-1})	15000	13700	21600
τ_e (s)	5.83×10^{-13}	5.11×10^{-13}	8.86×10^{-13}
τ_h (s)	$7,62 \times 10^{-13}$	3.73×10^{-13}	7.13×10^{-13}

Table 5.7: Selected thermal properties of bulk lead salts. The temperature dependence of the thermal resistivity is linearly interpolated from values in Ref. [129] below 300 K, and the phonon mean free path (m.f.p.) is calculated using Eq. (5.20).

Property	PbS	PbSe	PbTe
Debye Temperature θ_D [129]	220 K	160 K	130 K
Thermal Resistivity $1/\lambda$ (W^{-1}mK)	$\begin{cases} 17.9T & (\leq 180\,\text{K}) \\ 13.4T & (\geq 240\,\text{K}) \end{cases}$	$\begin{cases} 24.2T & (\leq 160\,\text{K}) \\ 19.5T & (\geq 200\,\text{K}) \end{cases}$	$16.42T$
Phonon m.f.p. (Λ). at 77 K	14.5 nm	13.2 nm	25 nm

In order to obtain the thermoelectric figure of merit for the superlattice nanowires, Eqs. (5.17)–(5.23) are employed to calculate the lattice thermal conductivity. The heat capacity and the sound velocity of the lead salts, which are essential parameters in determining the phonon mean free path in bulk materials, are inferred from the Debye temperature (θ_D) using the Debye model for the phonon dispersion relations. Table 5.7 lists the Debye temperature, lattice thermal resistivities ($1/\lambda$), and calculated phonon mean free paths Λ for various bulk lead salts at 77 K. Since the Debye temperatures of these lead salts are much higher than the temperature of interest here (77 K), a linear phonon dispersion relation is assumed for acoustic phonons, and the constant sound velocity is derived based on the Debye cut-off frequency.

With the lattice thermal conductivities thus obtained, Fig. 5-9 shows the calcu-
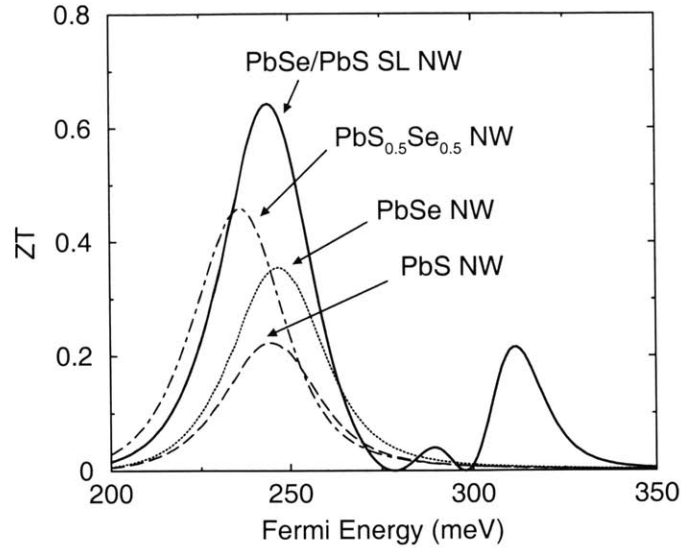
Figure 5-9: Calculated ZT as a function of Fermi energy for [001] PbSe(5 nm)/PbS(5 nm) superlattice nanowires, as well as PbSe, PbS, and $PbS_{0.5}Se_{0.5}$ nanowires at 77 K. The wire diameters are 10 nm in all cases.

lated ZT as a function of Fermi energy for [001] PbSe(5 nm)/PbS(5 nm) superlattice nanowires and for the corresponding PbSe, PbS, and $PbS_{0.5}Se_{0.5}$ nanowires with diameters $d_w = 10$ nm at 77 K, showing an enhancement in ZT for superlattice nanowires over pure or alloy lead salt nanowires. At the appropriate placement of Fermi energy, optimal ZT values of 0.65, 0.46, 0.36, and 0.22 are obtained for PbSe/PbS superlattice nanowires, $PbS_{0.5}Se_{0.5}$, PbSe, and PbS nanowires, respectively. Compared to homogeneous nanowires, there are more than one pronounced ZT extrema as a function of Fermi energy for the superlattice nanowires (see Fig. 5-9) due to the unusual Seebeck coefficient features in superlattice nanowires discussed earlier (see Fig. 5-8). It is interesting to note that in Fig. 5-9, the second ZT maximum for superlattice nanowires corresponds to a positive Seebeck coefficient, whereas the first and the third ZT peaks correspond to negative Seebeck coefficients. Since the sign of the Seebeck coefficient is critical in determining the direction of heat and current flows for thermoelectric devices, this sign should be carefully identified in determining the optimal ZT for the superlattice nanowires. The placement of Fermi energy is also important in order to realize desirable thermoelectric properties related to the sign

120
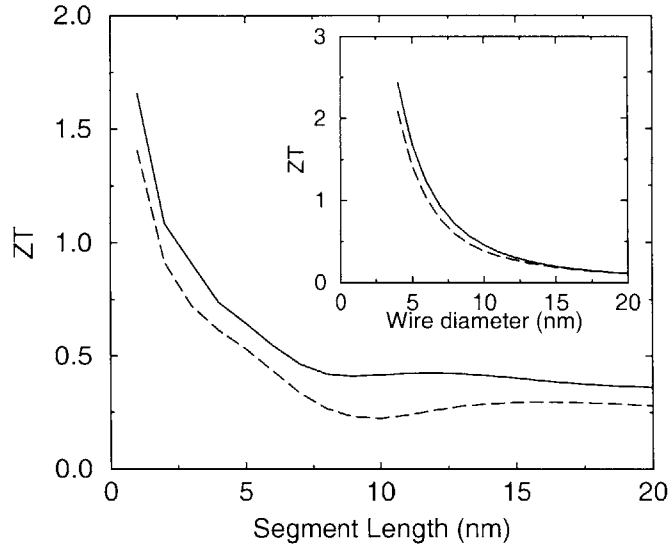
Figure 5-10: Calculated ZT as a function of segment length for n-type 10 nm-diameter PbSe/PbS superlattice nanowires oriented along the [001] (—) and [111] (- - -) directions at 77 K. Inset: calculated ZT for $PbS_{0.5}Se_{0.5}$ nanowires oriented along the [001] ( ) and [111] (- - -) directions as a function of wire diameter at 77 K.

of S.

Figure 5-10 shows the optimal ZT for n-type 10 nm-diameter PbSe/PbS superlattice nanowires as a function of segment length ($L_{PbSe} = L_{PbS}$) for two crystal orientations ([001] and [111]) at 77 K. For comparison, the inset of Fig. 5-10 shows the optimal ZT for $PbS_{0.5}Se_{0.5}$ nanowires calculated as a function of wire diameter at 77 K. At a diameter of 10 nm, the ZT values are 0.46 and 0.39 for [001] and [111] $PbS_{0.5}Se_{0.5}$ nanowires, respectively. We note that for both the PbSe/PbS superlattice and $PbS_{0.5}Se_{0.5}$ nanowires, the nanowires oriented along the [001] direction possess a slightly higher ZT than those oriented along the [111] direction, possibly due to a higher density of states and smaller transport effective masses for [001] wires, which result from the four degenerate pockets. As indicated in Fig. 5-10, the thermoelectric performance of the 10-nm superlattice nanowires increases rapidly as the segment length decreases, with ZT values higher than those of the corresponding alloy nanowires for segment lengths ≤ 7 nm. However, it is also noted that for longer segment lengths ($L_{PbSe} = L_{PbS} > 7$ nm), the superlattice nanowires exhibit a lower

Figure 5-11: Calculated ZT of n-type 5 nm-diameter PbSe/PbS superlattice nanowires as a function of segment length ($L_{PbSe} = L_{PbS}$) for [001] (—) and [111] (- - -) orientations at 77 K. Inset: electronic density of states of [001] PbSe/PbS superlattice nanowires with a wire diameter of 5 nm and $L_{PbSe} = L_{PbS} = 10$ nm at 77 K. The arrow indicates the Fermi energy ($\sim$ 782 meV) where the optimal ZT occurs.

ZT than the alloy nanowires, which may be due to a lower lattice thermal conductivity in the alloy nanowires. It is interesting to note how the thermoelectric performance of the superlattice and alloy nanowires, which contain the same number of Pb, S, and Se atoms, can be tailored by controlling the spatial arrangement (periodic segments vs. alloy) of the constituent species.

Figure 5-11 displays the ZT for n-type 5 nm-diameter PbSe/PbS superlattice nanowires as a function of segment length ($L_{PbSe} = L_{PbS}$) at 77 K, showing an oscillatory behavior as the segment length varies. For comparison, the ZT values for 5 nm-diameter $PbS_{0.5}Se_{0.5}$ nanowires are calculated as 1.68 and 1.41 for the [001] and [111] orientations, respectively (inset of Fig. 5-10). In Fig. 5-11, the optimal segment length for 5 nm-diameter PbSe/PbS superlattice nanowires is $\sim$ 3 nm for both [001] and [111] orientations, with optimal ZT values of 4.4 and 3.7, respectively, which are much higher than the optimal ZT of 10 nm-diameter superlattice nanowires of a similar segment length. The ZT oscillation as a function of segment length shown in Fig. 5-11, which is absent or insignificant in the larger diameter superlattice
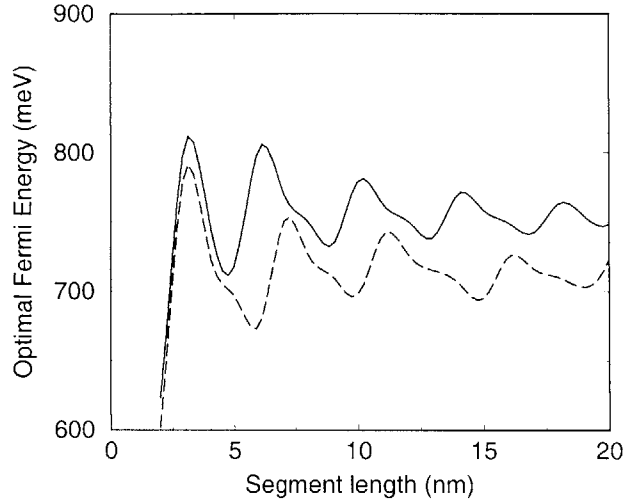
Figure 5-12: Calculated Fermi energy $E_{F(\text{opt})}$ for n-type 5 nm-diameter PbSe/PbS superlattice nanowires as a function of segment length ($L_{\text{PbSe}} = L_{\text{PbS}}$) for [001] (—) and [111] (- - -) orientations at 77 K.

nanowires (see Fig. 5-10), is due to the larger subband separation as the wire diameter decreases. The inset of Fig. 5-11 depicts the density of states for a 5 nm-diameter PbSe(10 nm)/PbS(10 nm) superlattice nanowire oriented along the [001] direction, showing that only *one* subband contributes to the transport properties in the energy range of importance, since the onset of the second subband does not appear until $E > 1000$ meV. The arrow in the inset of Fig. 5-11 indicates the optimal Fermi energy for the maximum ZT, which usually occurs near the band edge of the mini-bands. For small-diameter superlattice nanowires, the transport properties are mainly determined by the band width of the mini-bands and the mini-band gaps (which are highly dependent on the segment length), instead of the diameter-dependent subband energies. As shown in Fig. 5-2, the band structure of one subband evolves from that of the *alloy* limit to the *classical* limit as the segment length increases, resulting in an oscillatory optimal ZT due to the variation in the widths and gaps of the mini-bands. This oscillatory behavior is also reflected in the Fermi energy $E_{F(\text{opt})}$ where the optimal ZT occurs, as shown in Fig. 5-12 for the calculated $E_{F(\text{opt})}$ of 5 nm-diameter PbSe/PbS superlattice nanowires, which exhibits fluctuation as a function of segment length corresponding to the ZT oscillation in Fig. 5-11. In contrast to 5 nm-diameter
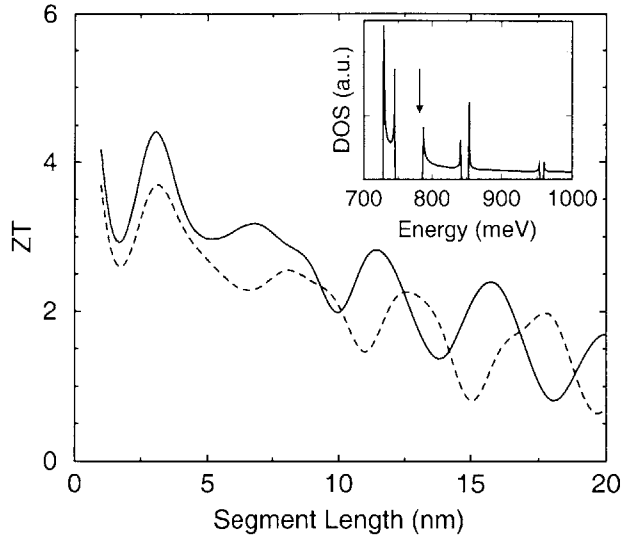
Figure 5-13: Calculated optimal ZT of p-type PbSe/PbS superlattice nanowires as a function of segment length ($L_{\text{PbSe}} = L_{\text{PbS}}$) for two different wire diameters oriented along [001] (—) and [111] (- - -) directions at 77 K.

nanowires, the density of states of 10 nm-diameter PbSe/PbS superlattice nanowires (see Fig. 5-7) exhibits a much more complicated energy dependence due to the superposition of multiple subbands in the energy range of the optimal ZT. Hence, for large-diameter superlattice nanowires, this ZT oscillation as a function of segment length becomes smeared out due to the averaging effect of the contributions from multiple subbands.

It should be pointed out that in the calculation of lead salt superlattice nanowires, we only consider contributions from the L-point carriers. However, for small-diameter nanowires with large subband separations, other high energy bands in the electronic structure may become important in determining transport properties. For the lead salts studied here, the second band extrema occur at the Σ or Δ points in the Brillouin zone, and the energies of these band extrema are all $\sim 1\,\text{eV}$ for the three lead salts in the bulk form [130]. Since the Fermi energy for ZT maximum is usually below $0.8\,\text{eV}$ for superlattice nanowires studied here (see Fig. 5-12), it is valid to neglect the contributions from these high energy bands in our model calculations.

124
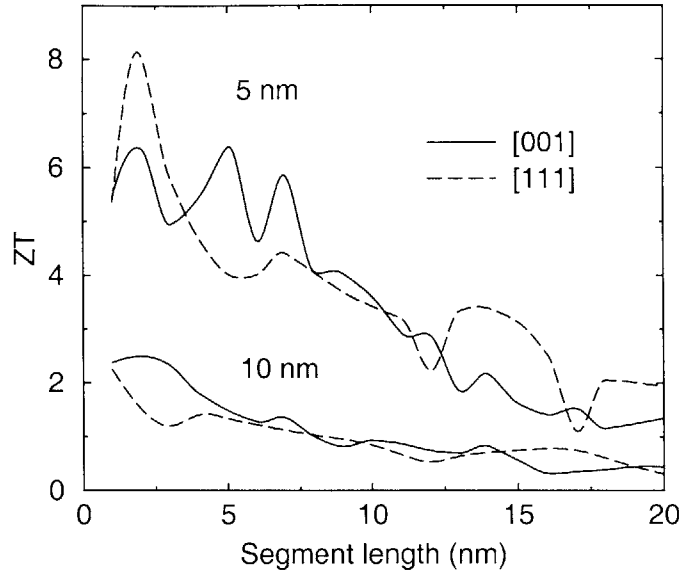
Figure 5-14: Calculated ZT of n-type PSe/PbTe superlattice nanowires as a function of segment length ($L_{PbSe} = L_{PbTe}$) for two different wire diameters (5 and 10 nm) oriented along the [001] (—) and [111] (- - -) directions at 77 K.

Since the lead salts have valence band structures similar to their conduction bands, p-type lead salt superlattice nanowires are expected to exhibit similar thermoelectric performance to their n-type counterparts. Figure 5-13 illustrates the calculated ZT of p-type PbSe/PbS superlattice nanowires as a function of segment length ($L_{PbSe} = L_{PbS}$) for two different wire diameters and crystal orientations, showing comparable ZT values and a similar dependence on the segment length to that for the n-type PbSe/PbS superlattice nanowires. The optimal ZT values for 5 nm-diameter p-type PbSe/PbS superlattice nanowires are calculated as 6.25 and 4.45 with segment lengths ~ 2 nm and ~ 3 nm for [001] and [111] orientations, respectively. We note that p-type PbSe/PbS superlattice nanowires have optimal ZT values slightly higher than the n-type PbSe/PbS superlattice nanowires, which may be due to the smaller effective masses for holes than for electrons in PbSe and PbS (see Table 5.5).

The thermoelectric performance of superlattice nanowires consisting of PbTe and PbSe segments is also calculated. Fig. 5-14 shows the ZT of n-type PbSe/PbTe superlattice nanowires as a function of segment length ($L_{PbSe} = L_{PbTe}$) for two different diameters (5 nm and 10 nm) and crystal orientations ([001] and [111]) at 77 K. The cor-
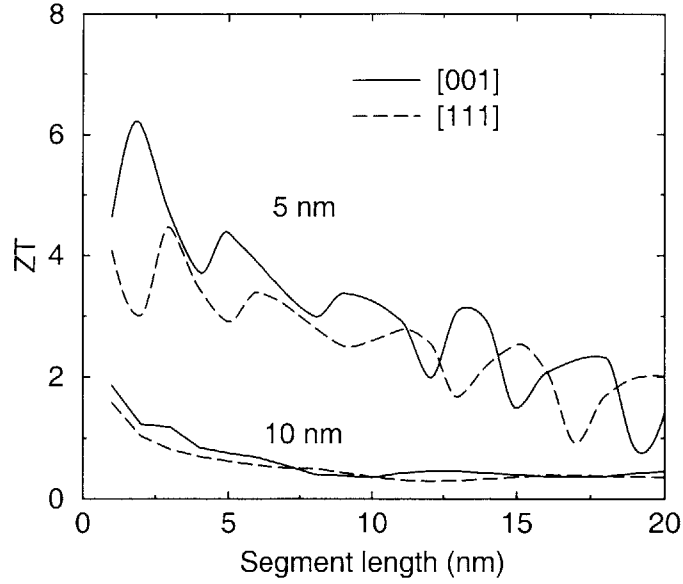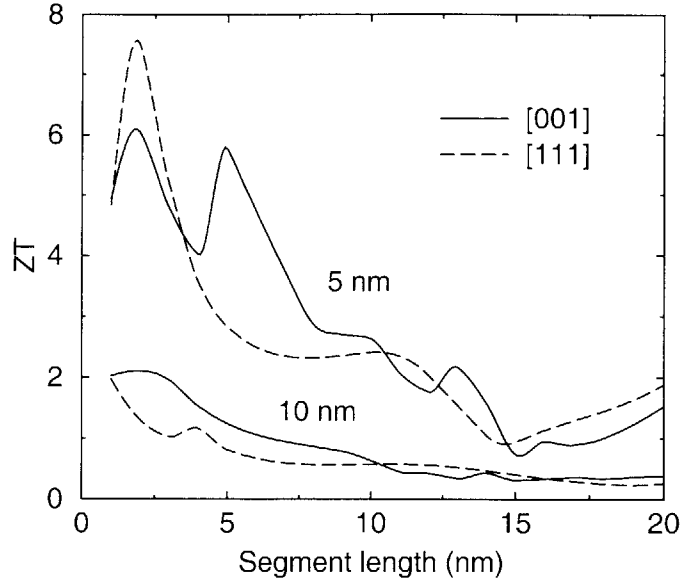
Figure 5-15: Calculated ZT of p-type PSe/PbTe superlattice nanowires as a function of segment length ($L_{PbSe} = L_{PbTe}$) for two different wire diameters (5 and 10 nm) oriented along the [001] (   ) and [111] (- - -) directions at 77 K.

responding results for p-type PbSe/PbTe superlattice nanowires are shown in Fig. 5-15. As indicated by Fig. 5-6, PbTe nanodots always constitute the potential barrier region in PbTe/PbSe superlattice nanowires, regardless of the wire diameter. We note that in addition to the 5 nm-diameter nanowires, the 10 nm-diameter PbSe/PbTe superlattice nanowires also exhibit an oscillatory ZT behavior because of the smaller effective masses and larger subband separations for PbTe. The optimal segment lengths for 5 nm-diameter PbTe/PbSe superlattice nanowires are $\sim$ 2 nm for both [001] and [111] orientations, with optimal ZT values higher than 6. Compared to PbSe/PbS superlattice nanowires in Fig. 5-10, the PbSe/PbTe superlattice nanowires usually possess better thermoelectric performance, which may be due to the better thermoelectric properties for PbTe than for PbS in the bulk forms. In addition, the higher carrier anisotropy and smaller effective masses in PbTe than in PbS (see Tables 5.2 and 5.5), which provide a larger density of states and lighter transport effective masses in nanowires, may also account for the higher ZT observed in PbTe/PbSe superlattice nanowires. Table 5.8 summarizes the optimal ZT and the corresponding

Table 5.8: Optimal ZT and segment lengths of 5 nm-diameter n- and p-type lead salt superlattice nanowires at 77 K.

Material		PbSe/PbS		PbSe/PbTe	
Orientation		[001]	[111]	[001]	[111]
n-type	Optimal ZT	4.40	3.70	6.37	8.07
	Segment Length	3 nm	3 nm	2 nm	2 nm
p-type	Optimal ZT	6.25	4.45	6.02	7.58
	Segment Length	2 nm	2 nm	2 nm	2 nm

segment lengths for n- and p-type PbSe/PbS and PbSe/PbTe superlattice nanowires at 77 K. We notice that p-type PbSe/PbTe superlattice nanowires possess a lower ZT than their n-type counterparts, in contrast to the p-type PbSe/PbS superlattice nanowires. This may be due to the larger effective masses and lower mobilities for holes than for electrons in PbTe (see Tables 5.5 and 5.6).

The calculations so far are made assuming an equal segment length for the two constituent materials. However, for a given period length $L = L_A + L_B$ for superlattice nanowires, the thermoelectric performance may be further optimized by adjusting the length ratio of the two materials. For example, Fig. 5-16 shows the calculated ZT for 5 nm-diameter n-type PbSe/PbS superlattice nanowires as a function of PbSe segment length L_{PbSe} at a given period $L = L_{PbSe} + L_{PbS} = 10$ nm. The optimal ZT values of 5 nm-diameter PbSe and PbS nanowires at 77 K are also shown in Fig. 5-16 for [001] and [111] orientations. We see that a higher ZT can be achieved for PbSe/PbS superlattice nanowires with unequal segment lengths for the PbSe and PbS nanodots. For the [001] orientation, PbSe(2 nm)/PbS(8 nm) superlattice nanowires has the highest ZT of 3.31, while PbSe(3 nm)/PbS(7 nm) superlattice nanowires are optimal for the [111] orientation with $ZT \sim 1.8$. As a comparison, for $L_{PbSe} = L_{PbS} = 5$ nm, the optimal ZT values corresponding to [001] and [111] superlattice nanowires are calculated as 2.98 and 1.68, respectively.

For PbSe/PbTe superlattice nanowires, a similar enhancement in ZT is also observed by choosing asymmetric segment lengths. Fig. 5-17 shows the ZT of 5 nm-diameter n-type PbSe/PbTe superlattice nanowires at 77 K calculated as a function

127
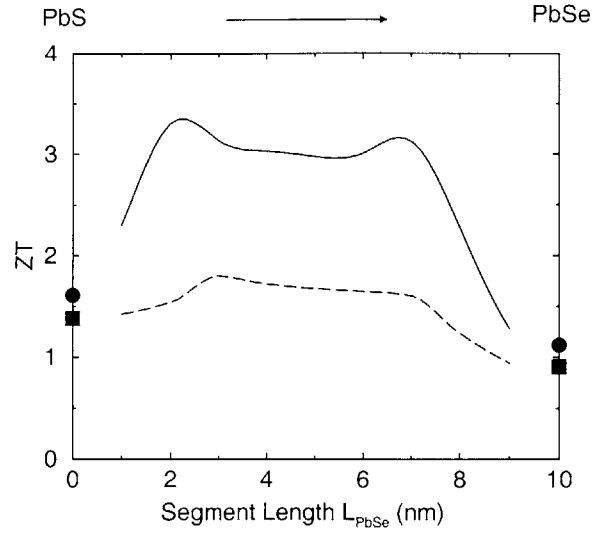
Figure 5-16: Calculated ZT for 5 nm-diameter n-type PbSe/PbS superlattice nanowires with [001] (—) and [111] (- - -) orientations as a function of PbSe segment length L_{PbSe} at 77 K. The segment length of PbS is chosen such that the period $L = L_{PbSe} + L_{PbS}$ is constant and equal to 10 nm. The optimal ZT for 5 nm-diameter PbS and PbSe nanowires are shown as (●) and (■) for [001] and [111] orientations, respectively.
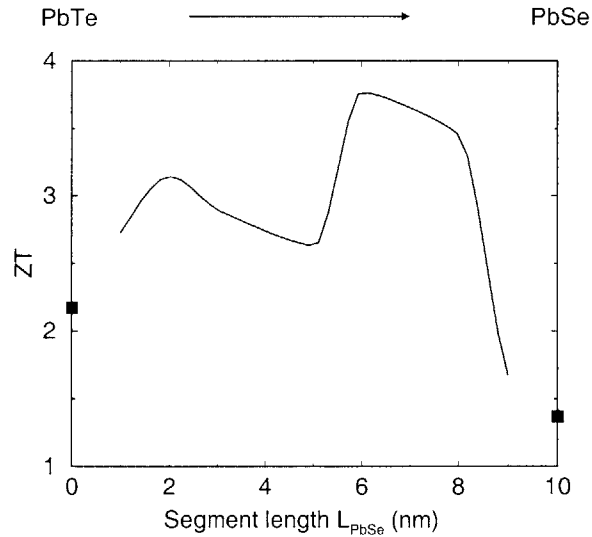
Figure 5-17: Calculated ZT for 5 nm-diameter n-type PbSe/PbTe superlattice nanowires oriented in the [111] direction as a function of PbSe segment length L_{PbSe} at 77 K. The segment length of PbTe is chosen such that the period $L = L_{PbSe} + L_{PbTe}$ is constant and equal to 10 nm. The optimal ZT for 5 nm-diameter PbTe and PbSe nanowires are shown as (■).

of PbSe segment length L_{PbSe} at a given period $L = L_{\text{PbSe}} + L_{\text{PbTe}} = 10\,\text{nm}$. The optimal segment length of PbSe is found to be 6 nm with $ZT \sim 3.8$ for [111] PbSe/PbTe superlattice nanowires, whereas the the optimal ZT value of PbSe(5 nm)/PbTe(5 nm) superlattice nanowires is only ~ 2.6 (see Fig. 5-17). We note that since the electronic band structure and the lattice thermal conductivity of superlattice nanowires are highly dependent on the wire diameter, segment lengths, and the transport properties of their constituent materials, the optimal length ratio for the two components is not universal and may vary for different period lengths and wire diameters. Superlattice nanowires with unequal segment lengths may possess better thermoelectric properties than those with equal segment lengths because the thermal resistivity and/or thermopower can be maximized by increasing the length of materials with desirable attributes without losing the advantage of the superlattice structure.

According to Table 5.8, the optimal ZT is usually achieved for segment lengths as short as 2 nm for lead salt superlattice nanowires at a diameter of 5 nm. However, it is necessary to check these length scales for internal consistency with the model assumption. First, since the lattice constants of these lead salts are about 5 Å, there are ~ 400 unit cells in a nanodot with a diameter of 5 nm and segment length of 2 nm, validating the application of the effective mass theorem and the band structure parameters used in the model calculation. In addition, the ζ values defined in Eq. (5.10) are calculated as ~ 0.4 and 0.5, respectively, for the first subband of 5 nm-diameter [001] PbSe(2 nm)/PbS(2 nm) and PbSe(2 nm)/PbTe(2 nm) superlattice nanowires. Based on the criterion ($\zeta \leq 0.1$) for the alloy limit from previous discussions, these superlattice nanowires are not in the alloy limit, and they do possess a unique electronic band structure that is dramatically different from that for a simple nanowire. This unique band structure partly accounts for the superior performance of the superlattice nanowires in comparison to the corresponding alloy nanowires.

5.4 Conclusions

In this chapter, we present a model for calculating the electronic band structure and transport properties of superlattice nanowires. The model considers the quantum confinement effects due to a cylindrical wire boundary and the formation of 1D subbands of anisotropic carriers. The dispersion relation of each subband in the superlattice nanowire is derived using the Kronig-Penney potential model, and exhibits very different features depending on the segment length. It is found that the electronic band structure of superlattice nanowires of very short and very long segment lengths can be well-approximated by the superposition of simple 1D band structures to substantially reduce the computational complexity.

The thermoelectric properties of superlattice nanowires made of various lead salts (PbS, PbSe, and PbTe) are investigated based on the electronic band structure model derived and 1D Boltzmann transport equations. Due to the electron mass differences between different materials, the potential barrier-well inversion induced by quantum confinement, which is a unique phenomenon in superlattice nanowires, is observed as the wire diameter decreases. The thermoelectric figure of merit ZT of these superlattice nanowires is found to be highly dependent on the segment length, wire diameter, crystal orientation, selection of material constituents, Fermi energy, and the segment length ratio. It is found that ZT generally increases with decreasing wire diameter and decreasing segment length before the alloy limit is reached. For thermoelectric applications, it is usually desirable to design superlattice nanowires composed of materials that have: (1) semiconducting band structures, (2) low inter-diffusion at the interface for effective carrier confinement to occur, and (3) multiple carrier pockets with high anisotropy to achieve a large density of states and small transport effective masses simultaneously.

For PbSe/PbS superlattice nanowires, ZT values higher than those of $PbS_{0.5}Se_{0.5}$ nanowires are possible for segment lengths $L_{PbS} = L_{PbSe} \leq 7\,nm$. An optimal ZT of > 4 is obtained for 5 nm-diameter PbSe/PbS superlattice nanowires. PbTe/PbSe superlattice nanowires possess even better thermoelectric performance than the cor-

responding PbSe/PbS superlattice nanowires, with an optimal ZT of > 6 because of a larger carrier anisotropy and smaller effective masses in PbTe. The results indicate that superlattice nanowires are promising systems for thermoelectric applications, when properly doped and designed. For the lead salt superlattice nanowires studied here, it is necessary to choose segment lengths smaller than the wire diameter in order to have higher ZT values than the corresponding alloy nanowires. For a given super-lattice period, model calculations show that the ZT value can be further improved by adopting different segment lengths for the two constituent materials.

The model developed here not only determines the optimal parameters for super-lattice nanowires (segment length, diameter, materials, and doping level) for thermo-electric applications, but also can be extended to other superlattice systems, such as 3D quantum dot arrays. Furthermore, the theoretical foundation provides a general framework to study superlattice nanowires for properties of interest to other appli-cations. It should be noted that although the results derived from the theoretical calculations are self-consistent with the model assumptions, transport measurements on realistic superlattice nanowires (which are not currently available) would provide valuable information to verify the important approximations and predictions (e.g., Kronig-Penney potential for subbands and the potential barrier-well inversion) and to further improve the theoretical model.

Chapter 6

Conclusions and Future Directions

6.1 Conclusions

This thesis presented an extensive experimental and theoretical study of the thermo-electric-related transport properties of $Bi_{1-x}Sb_x$ nanowires, and developed a theoretical framework for predicting the electrical properties of superlattice nanowires.

The Bi-related nanowires were synthesized by a template-assisted fabrication scheme, whereby nanowires were formed by pressure injecting liquid metal alloys into the cylindrical pores of anodic alumina. TEM and XRD studies showed that these nanowires possessed a very high crystalline quality with a common crystallographic orientation along the wire axis, and this preferred growth direction was found to be diameter-dependent. EDX verified that the Sb concentration in the $Bi_{1-x}Sb_x$ nanowires was consistent with that of the bulk alloy used in pressure injection, and confirmed that Sb was uniformly distributed throughout the entire wire. These characterization results justified the important fundamental assumptions and provided valuable information for modeling and understanding the transport properties of $Bi_{1-x}Sb_x$ nanowires.

A theoretical model for predicting the electronic and transport properties of nanowires was presented in Chapter 3, taking into consideration the effects of cylindrical wire boundary, multiple and anisotropic carrier pockets, and non-parabolic dispersion relations. The application of the model to $Bi_{1-x}Sb_x$ nanowires revealed a

unique semimetal-semiconductor transition as the wire diameter decreases or as the Sb concentration increases. In addition, an interesting physical phenomenon involving a very high hole density of states due to the coalescence of ten hole carrier pockets was uncovered for $Bi_{1-x}Sb_x$ nanowires under certain conditions. This would be particularly useful for improving the thermoelectric performance of p-type materials.

Various transport measurements were carried out for Bi-related nanowires as a function of temperature, wire diameter, Sb content, and magnetic field. Resistance measurements showed distinct temperature dependences for semimetallic and semiconducting nanowires, as predicted by the theory. Furthermore, with the help of modeling, the condition for the semimetal-semiconductor transition of $Bi_{1-x}Sb_x$ nanowires could be clearly identified. The resistance of 40-nm $Bi_{1-x}Sb_x$ nanowires, which was predicted to be semiconducting at all x, exhibited a complex dependence on the Sb content due to the presence of multiple types of carrier pockets and their energy dependence on the Sb content. An enhanced Seebeck coefficient was observed for $Bi_{1-x}Sb_x$ nanowires as the diameter decreases or as the Sb content increases, indicating that Sb alloying and the quantum confinement effects in Bi are both effective at decreasing the band overlap and enhancing the thermopower. The theoretical model was further extended to study transport properties of other nanowires, such as Te-doped Bi nanowires and Sb nanowires, and good agreement between theoretical predictions and experimental results was obtained, illustrating the applicability of our nanowire model.

A model for superlattice nanowires was presented to evaluate their potential for thermoelectric applications. Thermoelectric properties of superlattice nanowires made of various lead salts (PbS, PbSe, and PbTe) were investigated. An interesting inversion of the potential barrier and well induced by quantum confinement was predicted in superlattice nanowires as the wire diameter decreases. The thermoelectric figure of merit ZT of these superlattice nanowires was found to be highly dependent on the segment length, wire diameter, crystal orientation, selection of material constituents, Fermi energy, and segment length ratio. The results showed that ZT generally increased with decreasing wire diameter and with decreasing

segment length before the alloy limit was reached. For the lead salt superlattice nanowires, it was necessary to choose segment lengths smaller than the wire diameter in order to have higher ZT values than the corresponding alloy nanowires. For a given superlattice period, the ZT value could be improved by adopting different segment lengths for the two constituent materials. The model developed here not only determined the optimal parameters (segment length, diameter, materials, and doping level) for thermoelectric applications, but also could be expanded to other superlattice systems, such as 3D quantum dot arrays. Furthermore, the theoretical foundation given here provided a general framework to study properties of interest to other applications of superlattice nanowires.

6.2   Suggestions for Future Studies

In this section, we summarize several research directions that are worthy of further research.

In this thesis, we have performed extensive transport measurements on $Bi_{1-x}Sb_x$ nanowire arrays using a two-probe setup, and valuable information has been extracted with the help of theoretical modeling. Further experimental studies on single or free-standing nanowires are intriguing because single-wire measurements minimize the uncertainties arising from the distribution of nanowire characteristics (e.g. wire diameter, crystal quality, crystallographic orientation, Sb content, etc.) in an array, so that a detailed quantitative comparison between model calculation and experimental results would be possible. In addition, they would also provide vital information that cannot be obtained by the two-probe measurements, such as the absolute conductivity that is critical in determining the thermoelectric figure of merit. Recently, thermal conductivity [131] and electrical conductivity measurements [97, 113] of single nanowires have been demonstrated by patterning tiny electrodes and heaters using novel lithographic techniques. While these single-wire measurement techniques may be readily applied to $Bi_{1-x}Sb_x$ nanowire systems, oxide problems and

materials issues (e.g. compatibility with the lithography resist and chemicals used) remain as major challenges that have to be overcome in order to study the transport properties of single nanowires.

Another promising opportunity associated with single-wire measurements is the possibility to control Fermi energy via a third gate electrode [113, 132]. The gate electrode is usually separated from the nanowire by a thin oxide layer, and the native oxide that is formed on the surface of the free-standing nanowires could be useful in this respect if the oxide thickness can be carefully controlled. Since the transport properties and thermoelectric performance of nanowires are highly dependent on the placement of the Fermi energy, the ability to control the Fermi energy and the carrier concentration is critical in optimizing the thermoelectric figure of merit. Compared with other means to vary the Fermi energy of nanowires by doping with impurity atoms (e.g. Te), the use of a gate electrode has additional advantages that the Fermi energy may be fine tuned by the external circuit without having to prepare numerous samples with different doping levels, and the electron scattering due to the charged impurities can be avoided. Gate electrodes can be fabricated on nanowires by electron beam lithography [132] or by the crossing of a second nanowire on top of the target nanowire, as demonstrated by Huang *et al.* in nanowire-based field-effect transistor (FET) devices [113].

For practical thermoelectric applications based on nanowires, we need to synthesize both *p*- and *n*-type thermoelectric components and assemble nanowires to a macroscopic scale as required by real devices. One promising scheme proposed by Rabin *et al.* is to pattern the templates and then grow nanowire arrays electrochemically [133]. In this approach, different types of nanowires can be selectively grown at different locations of the template to provide the required functionality. In addition, this technique also possesses the potential to synthesize nanowires with smaller diameters (≤ 10 nm), and can be scaled up to produce large-area nanowire arrays.

In Chapter 5 of the thesis, superlattice nanowires were investigated with theoretical modeling. Transport measurements on realistic superlattice nanowires,
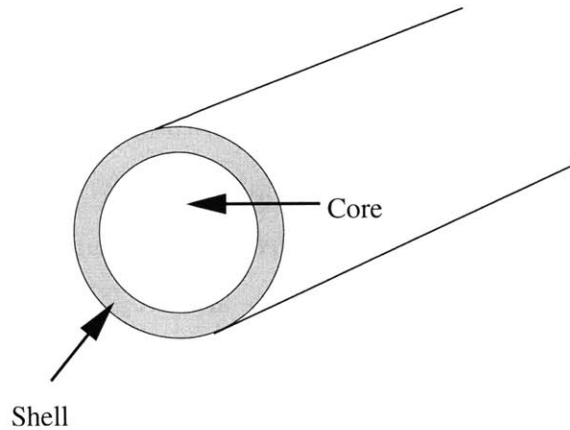
Figure 6-1: Schematic diagram of a coaxially layered (core-shell) nanowire.

which are not currently available, would provide valuable information to verify the important approximations and predictions (e.g., Kronig-Penny potential for subbands and the potential barrier-well inversion), and to further improve the theoretical model. It would also be interesting to study superlattice nanowires with non-perfect periodicity. While Gomez *et al.* have pointed out that the electronic band structure may not be significantly affected by the discrepancy from the perfect periodic potential [134], the lattice thermal conductivity may be, however, further reduced due to random interference of the phonon waves.

Besides the superlattice nanowires, another heterogeneous structure that is of great interest for nanowires is a coaxially layered structure, as shown in Fig. 6-1. These radially modulated nanowires can be synthesized by first growing a nanowire by the VLS method, and then changing the synthesis conditions to deposit a different material on the nanowire surface by CVD. Lattice dislocations due to lattice mismatch at the heterogeneous interface may be avoided if the outer shell thickness is kept small to facilitate epitaxial growth of the shell on the surface of the nanowire core. This technique was demonstrated for the synthesis of Si/Ge and Ge/Si coaxial (or core-shell) nanowires [135], and it was shown that by a thermal annealing process, the outer shell can be formed epitaxially on the inner core. These coaxially layered nanowires may be carefully designed to provide a unique 1D system that has high

mobility carriers and reduced lattice thermal conductivity. By choosing a narrow-gap material for the core, and a potential barrier material as the shell of the coaxial nanowire, the electron wavefunctions will be confined in the potential well of the core region, thus minimizing the electron scattering at the wire boundary and enhancing the carrier mobility. We note that since the surface conditions (e.g. roughness, passivation layer, dangling bonds, etc.) of nanowires usually have significant impact on the electrical properties of ordinary nanowires, this core-shell structure is desirable to eliminate surface effects by confining the electrons within the core region. The core-shell interface may also be beneficial for thermoelectric applications as increased phonon scattering at the interface would reduce the lattice thermal conductivity.

Bibliography

[1] Y. Y. Wu and P. D. Yang, J. Am. Chem. Soc. **123**, 3165 (2001).

[2] Z. Zhang, J. Y. Ying, and M. S. Dresselhaus, J. Mater. Res. **13**, 1745 (1998).

[3] C. B. Murray, C. R. Kagan, and M. G. Bawendi, Science **270**, 1335 (1995).

[4] A. F. Ioffe, *Semiconductor Thermoelements and Thermoelectrics Cooling*, Infosearch Ltd., London, 1957.

[5] L. D. Hicks and M. S. Dresselhaus, Phys. Rev. B **47**, 12727 (1993).

[6] L. D. Hicks and M. S. Dresselhaus, Phys. Rev. B **47**, 16631 (1993).

[7] L. D. Hicks. *The Effect of Quantum-Well Superlattices on the Thermo-electric Figure of Merit*. Ph. D. thesis, Massachusetts Institute of Technology, Department of Physics, June 1996.

[8] X. Sun. *The Effect of Quantum Confinement on the Thermoelectric Figure of Merit*. Ph. D. Thesis, Massachusetts Institute of Technology, Department of Physics, June 1999.

[9] L. D. Hicks, T. C. Harman, X. Sun, and M. S. Dresselhaus, Phys. Rev. B **53**, R10493 (1996).

[10] X. Sun, S. B. Cronin, J. Lin, K. L. Wang, T. Koga, M. S. Dresselhaus, and G. Chen. In *The 18th International Conference on Thermoelectrics: ICT Symposium Proceedings, Baltimore*, edited by G. Chen, 1999, p. 652.

[11] T. C. Harman, P. J. Taylor, M. P. Walsh, and B. E. LaForge, Science **297**, 2229 (2002).

[12] M. S. Gudiksen, J. F. Wang, and C. M. Lieber, J. Phys. Chem. B **106**, 4036 (2002).

[13] X. F. Duan, Y. Huang, Y. Cui, J. F. Wang, and C. M. Lieber, Nature **409**, 66 (2001).

[14] M. R. Black, Y.-M. Lin, S. B. Cronin, O. Rabin, and M. S. Dresselhaus, Phys. Rev. B **65**, 195417 (2002).

[15] Y. Y. Wu, H. Q. Yan, and P. D. Yang, Top. Catal. **19**, 197 (2002).

[16] H. Zeng, M. Zheng, R. Skomski, and D. J. Sellmyer, J. Appl. Phys. **87**, 4718 (2000).

[17] K. Nielsch, R. B. Wehrspohn, J. Barthel, U. Gosele, S. F. Fischer, and H. Kronmuller, Appl. Phys. Lett. **79**, 1360 (2001).

[18] R. P. Feynman, http://www.zyvex.com/nanotech/feynman.html, (1959).

[19] Z. Zhang, D. Gekhtman, M. S. Dresselhaus, and J. Y. Ying, Chem. Mater. **11**, 1659 (1999).

[20] C. A. Huber, T. E. Huber, M. Sadoqi, J. A. Lubin, S. Manalis, and C. B. Prater, Science **263**, 800 (1994).

[21] T. E. Huber, M. J. Graf, and C. A. Foss, Jr. In *The 18th International Conference on Thermoelectrics: ICT Symposium Proceedings*, edited by G. Chen, 1999, p. 558.

[22] J. Heremans, C. M. Thrush, Y.-M. Lin, S. Cronin, Z. Zhang, M. S. Dresselhaus, and J. F. Mansfield, Phys. Rev. B **61**, 2921 (2000).

[23] G. S. Cheng, L. D. Zhang, Y. Zhu, G. T. Fei, L. Li, C. M. Mo, and Y. Q. Mao, Appl. Phys. Lett. **75**, 2455 (1999).

[24] L. Sun, P. C. Searson, and C. L. Chien, Appl. Phys. Lett. **74**, 2803 (1999).

[25] C. A. Foss, Jr., M. J. Tierney, and C. R. Martin, J. Phys. Chem. **96**, 9001 (1992).

[26] G. L. Hornyak, C. J. Patrissi, and C. M. Martin, J. Phys. Chem. B **101**, 1548 (1997).

[27] G. Fasol, Science **280**, 545 (1998).

[28] L. Piraux, I. M. George, J. F. Despres, C. Leroy, E. Ferain, R. Legras, K. Ounadjela, and A. Fert, Appl. Phys. Lett. **65**, 2484 (1994).

[29] C. R. Martin, Science **266**, 1961 (1994).

[30] T. M. Whitney, J. S. Jiang, P. C. Searson, and C. L. Chien, Science **261**, 1316 (1993).

[31] A. Blondel, J. P. Meier, B. Doudin, and J.-Ph. Ansermet, Appl. Phys. Lett. **65**, 3019 (1994).

[32] L. Piraux, S. Dubois, J. L. Duvail, A. Radulescu, S. Demoustier-Champagne, E. Ferain, and R. Legras, J. Mater. Res. **14**, 3042 (1999).

[33] K. Liu, C. L. Chien, P. C. Searson, and Y. Z. Kui, Appl. Phys. Lett. **73**, 1436 (1998).

[34] D. Routkevitch, T. Bigioni, M. Moskovits, and J. M. Xu, J. Phys. Chem. **100**, 14073 (1996).

[35] D. Routkevitch, A. A. Tager, J. Haruyama, D. AlMawlawi, M. Moskovits, and J. M. Xu, IEEE Trans. Electron. Dev. **43**, 1646 (1996).

[36] G. Yi and W. Schwarzacher, Appl. Phys. Lett. **74**, 1746 (1999).

[37] X. Peng, L. Manna, W. Yang, J. Wickham, E. Scher, A. Kadavanich, and A. P. Alivisatos, Nature **404**, 59 (2000).

[38] M. S. Sander, A. L. Prieto, R. Gronsky, T. Sands, and A. M. Stacy, Adv. Mater. **14**, 665 (2002).

[39] A. M. Morales and C. M. Lieber, Science **279**, 208 (1998).

[40] D. P. Yu, C. S. Lee, I. Bello, G. W. Zhou, and Z. G. Bai, Solid State Commun. **105**, 403 (1998).

[41] Y. F. Zhang, Y. H. Tang, N. Wang, D. P. Yu, C. S. Lee, I. Bello, and S. T. Lee, Appl. Phys. Lett. **72**, 1835 (1998).

[42] Y. F. Zhang, Y. H. Tang, N. Wang, C. S. Lee, I. Bello, and S. T. Lee, Phys. Rev. B **61**, 4518 (2000).

[43] X. Duan, J. Wang, and C. M. Lieber, Appl. Phys. Lett. **76**, 1116 (2000).

[44] Y. H. Tang, N. Wang, Y. F. Zhang, C. S. Lee, I. Bello, and S. T. Lee, Appl. Phys. Lett **75**, 2921 (1999).

[45] N. Wang, Y. H. Tang, Y. F. Zhang, C. S. Lee, and S. T. Lee, Phys. Rev. B **58**, R16024 (1998).

[46] R. Nötzel, N. N. Ledentsov, L. Daweeritz, and K. Ploog, Phys. Rev. B **45**, 3507 (1992).

[47] H. Omi and T. Ogino, Appl. Phys. Lett. **71**, 2163 (1997).

[48] S. Y. Chou, P. R. Krauss, and L. S. Kong, J. Appl. Phys. **79**, 6101 (1996).

[49] Y.-M. Lin, M. S. Dresselhaus, and J. Y. Ying, Adv. Chem. Eng. **27**, 167 (2001).

[50] M. S. Dresselhaus, Y.-M. Lin, O. Rabin, M. R. Black, and G. Dresselhaus. In *Nanotechnology Handbook*, edited by Bharat Bhushan, Springer-Verlag, Heidelberg, Germany, in press.

[51] D. AlMawlawi, C. Z. Liu, and M. Moskovits, J. Mater. Res. **9**, 1014 (1994).

[52] G. A. Ozin, Adv. Mater. **4**, 612 (1992).

[53] R. J. Tonucci, B. J. Justus, A. J. Campillo, and C. E. Ford, Science **258**, 783 (1992).

[54] J. Y. Ying, Science Spectra **18**, 56 (1999).

[55] E. Ferain and R. Legras, Nucl. Instrum. Methods B **84**, 331 (1993).

[56] T. Thurn-Albrecht, J. Schotter, G. A. Kästle, N. Emley, T. Shibauchi, L. Krusin-Elbaum, K. Guarini, C. T. Black, M. T. Tuominen, and T. P. Russell, Science **290**, 2126 (2000).

[57] D. L. Demske, J. L. Price, N. A. Guardala, N. Lindsey, and J. H. Barkyoumb, Mater. Res. Soc. Symp. Proc. **545**, 209 (1998).

[58] J. P. Heremans, C. M. Thrush, D. T. Morelli, and M.-C. Wu, Phys. Rev. Lett. **88**, 216801 (2002).

[59] J. W. Diggle, T. C. Downie, and C. W. Goulding, Chem. Rev. **69**, 365 (1969).

[60] J. P. O'Sullivan and G. C. Wood, Proc. R. Soc. London A **317**, 511 (1970).

[61] A. P. Li, F. Muller, A. Birner, K. Neilsch, and U. Gosele, J. Appl. Phys. **84**, 6023 (1998).

[62] O. Jessenky, F. Muller, and U. Gosele, Appl. Phys. Lett. **72**, 1173 (1998).

[63] D. AlMawlawi, N. Coombs, and M. Moskovits, J. Appl. Phys. **70**, 4421 (1991).

[64] A. N. Govyadinov and S. A. Zakhvitcevich, J. Vac. Sci. Technol. B **16**, 1222 (1998).

[65] D. N. Davydov, P. A. Sattari, D. AlMawlawi, A. Osika, T. L. Haslett, and M. Moskovits, J. Appl. Phys. **86**, 3983 (1999).

[66] J. Li, C. Papadopoulos, J. M. Xu, and M. Moskovits, Appl. Phys. Lett. **75**, 367 (1999).

[67] H. Masuda, M. Ohya, H. Asoh, and M. Nakao, Jpn. J. Appl. Phys. **38**, 1403 (1999).

[68] Y. Li, E. R. Holland, and P. R. Wilshaw, J. Vac. Sci. Technol. B **18**, 994 (2000).

[69] N. Kouklin, S. Bandyopadhyay, S. Tereshin, A. Varfolomeev, and D. Zaretsky, Appl. Phys. Lett. **76**, 460 (2000).

[70] F. Li, L. Zhang, and R. M. Metzger, Chem. Mater. **10**, 2470 (1998).

[71] Y.-M. Lin, X. Sun, S. Cronin, Z. Zhang, J. Y. Ying, and M. S. Dresselhaus, Mater. Res. Soc. Symp. Proc. **582**, H10.3.1 (2000).

[72] Z. B. Zhang. *Fabrication, Characterization and Transport Properties of Bismuth Nanowire Systems*. Ph. D. Thesis, Massachusetts Institute of Technology, Department of Physics, February 1999.

[73] S. B. Cronin, Y.-M. Lin, O. Rabin, M. R. Black, G. Dresselhaus, M. S. Dresselhaus, and P. L. Gai, Microscopy and Microanalysis **8**, 58 (2002).

[74] T. E. Huber, M. J. Graf, C. A. Foss, Jr., and P. Constant, J. Mater. Res. **15**, 1816 (2000).

[75] J. Heremans and O. P. Hansen, J. Phys. C **12**, 3483 (1979).

[76] R. T. Isaacson and G. A. Williams, Phys. Rev. **185**, 682 (1969).

[77] B. Lenoir, M. Cassart, J. P. Michenaud, H. Scherrer, and S. Scherrer, J. Phys. Chem. Solids **57**, 89 (1996).

[78] H. J. Goldsmid, Phys. Stat. Sol. (a) **1**, 7 (1970).

[79] Y.-M. Lin, X. Sun, and M. S. Dresselhaus, Phys. Rev. B **62**, 4610 (2000).

[80] M. R. Black, M. Padi, S. B. Cronin, Y.-M. Lin, O. Rabin, T. McClure, G. Dresselhaus, P. L. Hagelstein, and M. S. Dresselhaus, Appl. Phys. Lett. **77**, 4142 (2000).

[81] X. Sun, Z. Zhang, and M. S. Dresselhaus, Appl. Phys. Lett. **74**, 4005 (1999).

[82] N. W. Ashcroft and N. D. Mermin, *Solid State Physics*, Holt, Rinehart and Winston, New York, 1976, Chapter 13.

[83] S. G. Walkauskas, D. A. Broido, and K. Kempa, J. Appl. Phys. **85**, 2579 (1999).

[84] S .G Walkauskas, D. A. Broido, K. Kempa, and T. L. Reinecke, J. Appl. Phys. **85**, 2579 (1999).

[85] C. Kittel, *Introduction to Solid State Physics*, 7th Ed., John Wiley & Sons Inc., New York, 1996, Chapter 5.

[86] Y.-M. Lin. *Fabrication, Characterization, and Theoretical Modeling of the Te-doped Bi Nanowire System for Thermoelectric Applications*. M. S. Thesis, Massachusetts Institute of Technology, Department of Electrical Engineering and Computer Science, June 2000.

[87] H. R. Verdun and H. D. Drew, Phys. Rev. Lett. **33**, 1608 (1974).

[88] G. A. Saunders and Z. Sümengen, Proc. Roy. Soc. London A **329**, 453 (1972).

[89] C. F. Gallo, B. S. Chandrasekhar, and P. H. Sutter, J. Appl. Phys. **34**, 144 (1963).

[90] M. P. Vecchi and M. S. Dresselhaus, Phys. Rev. B **10**, 771 (1974).

[91] L. M. Falicov and P. J. Lin, Phys. Rev. **141**, 562 (1966).

[92] R. W. G. Wyckoff, *Crystal Structures*, Vol. 1, Interscience, New York, 1964.

[93] P. Cucka and C. S. Barrett, Acta. Crystallogr. **15**, 865 (1962).

[94] O. Rabin, Y.-M. Lin, and M. S. Dresselhaus, Appl. Phys. Lett. **79**, 81 (2001).

[95] T. Koga, X. Sun, S. B. Cronin, and M. S. Dresselhaus, Appl. Phys. Lett. **75**, 2438 (1999).

[96] J. Heremans, C. M. Thrush, Z. Zhang, X. Sun, M. S. Dresselhaus, J. Y. Ying, and D. T. Morelli, Phys. Rev. B **58**, R10091 (1998).

[97] S. B. Cronin, Y.-M. Lin, O. Rabin, M. R. Black, J. Y. Ying, M. S. Dresselhaus, P. L. Gai, J.-P. Minet, and J.-P. Issi, Nanotech. J. **13**, 653 (2002).

[98] Y.-M. Lin, O. Rabin, S. B. Cronin, J. Y. Ying, and M. S. Dresselhaus, Appl. Phys. Lett. **81**, 2403 (2002).

[99] Y.-M. Lin, S. B. Cronin, J. Y. Ying, M. S. Dresselhaus, and J. P. Heremans, Appl. Phys. Lett. **76**, 3944 (2000).

[100] N. W. Ashcroft and N. D. Mermin, *Solid State Physics*, Holt, Rinehart and Winston, New York, 1976, Chapter 16.

[101] K. Hong, F. Y. Yang, K. Liu, D. H. Reich, P. C. Searson, and C. L. Chien, J. Appl. Phys. **85**, 6184 (1999).

[102] Y.-M. Lin, S. B. Cronin, O. Rabin, J. Y. Ying, and M. S. Dresselhaus, Mater. Res. Soc. Symp. Proc. **737**, in press.

[103] Y.-M. Lin, S. B. Cronin, O. Rabin, J. Y. Ying, and M. S. Dresselhaus, Appl. Phys. Lett. **79**, 677 (2001).

[104] Z. Zhang, X. Sun, M. S. Dresselhaus, J. Y. Ying, and J. Heremans, Phys. Rev. B **61**, 4850 (2000).

[105] H. Brooks, Adv. Electron. Electron Phys. **7**, 158 (1955).

[106] J. Heremans, C. M. Thrush, Y.-M. Lin, S. B. Cronin, and M. S. Dresselhaus, Phys. Rev. B **63**, 085406 (2001).

[107] J. Heremans and C. M. Thrush, Phys. Rev. B **59**, 12579 (1999).

[108] K. Liu, C. L. Chien, and P. C. Searson, Phys. Rev. B **58**, 14681 (1998).

[109] X. F. Wang, L. D. Zhang, J. Zhang, H. Z. Shi, X. S. Peng, M. J. Zheng, J. Fang, J. L. Chen, and B. J. Gao, J. Phys. D **34**, 418 (2001).

[110] Z. Zhang, X. Sun, M. S. Dresselhaus, J. Y. Ying, and J. Heremans, Appl. Phys. Lett. **73**, 1589 (1998).

[111] J. Heremans, C. Thrush, D. Morelli, and M.-C. Wu, unpublished.

[112] D. E. Beutler and N. Giordano, Phys. Rev. B **38**, 8 (1988).

[113] Y. Huang, X. F. Duan, Y. Cui, L. J. Lauhon, K.-H. Kim, and C. M. Lieber, Science **294**, 1313 (2001).

[114] R. Venkatasubramanian, E. Siivola, T. Colpitts, and B. O'Quinn, Nature **413**, 597 (2001).

[115] M. S. Dresselhaus, Y.-M. Lin, T. Koga, S. B. Cronin, O. Rabin, M. R. Black, and G. Dresselhaus. In *Semiconductors and Semimetals: Recent Trends in Thermoelectric Materials Research III*, edited by T. M. Tritt, Academic Press, San Diego, 2001, Chapter 1.

[116] A. A. Balandin and O. L. Lazarenkova, Appl. Phys. Lett. **82**, 415 (2003).

[117] C. Dames and G. Chen, submitted to J. Appl. Phys.

[118] Y. Wu, R. Fan, and P. Yang, Nano Lett. **2**, 83 (2002).

[119] M. S. Gudiksen, L. J. Lauhon, J. Wang, D. C. Smith, and C. M. Lieber, Nature **415**, 617 (2002).

[120] M. T. Bjork, B. J. Ohlsson, C. Thelander, A. I. Persson, K. Deppert, L. R. Wallenberg, and L. Samuelson, Appl. Phys. Lett. **81**, 4458 (2002).

[121] M. T. Bjork, B. J. Ohlsson, T. Sass, A. I. Persson, C. Thelander, M. H. Magnusson, K. Deppert, L. R. Wallenberg, and L. Samuelson, Nano Lett. **2**, 87 (2002).

[122] N. W. Ashcroft and N. D. Mermin, *Solid State Physics*, Holt, Rinehart and Winston, New York, 1976, Chapter 8.

[123] G. Chen, Phys. Rev. B **57**, 14958 (1998).

[124] E. T. Swartz and R. O. Pohl, Rev. Mod. Phys. **61**, 605 (1989).

[125] G. Chen, Appl. Phys. Lett. **82**, 991 (2003).

[126] H. Preier, Appl. Phys. **20**, 189 (1979).

[127] R. Dalven, Infrared Phys. **9**, 141 (1969).

[128] R. S. Allgaier and W. W. Scanlon, Phys. Rev. **111**, 1029 (1958).

[129] Yu. I. Ravich, B. A. Efimova, and I. A. Smirnov. In *Semiconducting Lead Chaco-genides*, edited by L. S. Stil'bans, Plenum Press, New York, 1970, Chapter 4.

[130] P. J. Lin and L. Kleinman, Phys. Rev. **142**, 478 (1966).

[131] D. G. Cahill, W. F. Ford, K. E. Goodson, G. D. Mahan, A. Majumdar, H. J. Maris, R. Merlin, and S. R. Phillpot, J. Appl. Phys. **93**, 793 (2003).

[132] S.-W. Chung, J.-Y. Yu, and J. R. Heath, Appl. Phys. Lett. **76**, 2068 (2000).

[133] O. Rabin, Y.-M. Lin, S. B. Cronin, G. Chen, and M. S. Dresselhaus, Mater. Res. Soc. Symp. Proc. **739**, in press.

[134] I. Gomez, F. Dominguez-Adame, E. Diez, and P. Orellana, J. Appl. Phys. **92**, 4486 (2002).

[135] L. J. Lauhon, M. S. Gudiksen, D. Wang, and C. M. Lieber, Nature **420**, 57 (2002).